Faraday Current Sensing

van der Veeken, H.J.L.

Award date:
2021

ASML &
Eindhoven University of Technology

Faraday Current Sensing

60 ECTS Graduation Project

H.J.L. van der Veeken

Supervisors:
ir. J. van Duivenbode
dr. ir. R. Lavrijsen

Eindhoven, February 2021

Abstract

A Faraday based current sensor is investigated for its feasibility of reaching a required 1 ppm error and a bandwidth of ≥ 1 MHz for the wafer stage of ASML. A first proof of principle showed a error of 3% at 1 MHz that can be reached with a single TGG crystal. However, the available peripherals were not ideal for a first proof of principles. Repeatability turned out to be a significant issue. The different contributions to the total error in the Faraday based current sensor are investigated. It is calculated that the shot noise and temperature drift of the Verdet constant limit the applicability of the Faraday based current sensor. However, only the temperature drift was verified experimentally. Because the temperature drift significantly influences the accuracy it is proposed to lower it by using a temperature bath. This leaves a remained of 2% theoretical shot noise.

By using multiple TGG crystals to increase the path length of the light a linear increase in the gain is achieved. It is deduced to give a minimal error of 0.2%. It was found experimentally that the gain increased by a factor of ~ 1.7 by allowing the light to travel through the crystal twice. The non-ideal effect of the silver mirrors caused a reduction from the ideal factor 2. In a theoretical extrapolation this effect is used to estimate the effect on multiple reflections. Three designs are considered that overcome the incurred phase shift of the reflection. It is derived theoretically that a reflection interface with a small difference in refractive index can allow for 100 reflections. This reduces the error to 506 ppm. Because of non-linearity on the output of the optical setup a compensation scheme is proposed. It may further lower the error to 280 ppm. Further ample routes are sketched for further reducing the error to a theoretical 42 ppm. Using ideal circumstances it is conjectured that the error level can be reduced to 9 ppm. Compared to the presently used Fluxgate of ASML it performs worse at low bandwidths. A major advantage is, however, that it has potentially a much higher bandwidth. Note that the temperature drift of 238 ppm is significantly larger than the ideal conjectured 9 ppm.

Instead of designing complex design to reduce the temperature drift it may be more beneficial to invest in Photonic integrated circuits (PIC). Their accuracy is of the same order of magnitude as dictated by the temperature drift. This makes them interesting in applications with required accuracies of roughly 0.1%, and a high bandwidths (> 1 MHz) is needed.

Contents

Contents v

1 Definitions 1
- 1.1 Definitions . . . 1
  - 1.1.1 Polarization . . . 1
  - 1.1.2 Error and Noise . . . 1
  - 1.1.3 Synonyms in literature . . . 2
  - 1.1.4 abbreviations . . . 2

2 Introduction 3
- 2.1 This thesis . . . 5

3 Faraday Effect 7
- 3.1 Phenomenological Description . . . 7
- 3.2 The Faraday Based Current sensor . . . 8
  - 3.2.1 Estimations of the Faraday effect . . . 9
- 3.3 Microscopic Origin . . . 11
  - 3.3.1 Spin Orbit Coupling . . . 11
  - 3.3.2 Wavelength and Temperature dependency . . . 13
- 3.4 Material Considerations . . . 16
  - 3.4.1 Garnets . . . 17
  - 3.4.2 Other Crystal Structures . . . 18
  - 3.4.3 Material in this Thesis . . . 18

4 Measurement Techniques 20
- 4.1 Measuring the Faraday Effect . . . 20
  - 4.1.1 Polarimetry . . . 20
  - 4.1.2 Interferometry . . . 22
- 4.2 Experimental Equipment . . . 22
  - 4.2.1 Magnetic field . . . 23
  - 4.2.2 Samples . . . 23
- 4.3 Experimental Methods . . . 24
  - 4.3.1 Measurements . . . 24
  - 4.3.2 Error calculation . . . 24

5 Results and Discussion 25
- 5.1 Faraday based Current sensing using TGG . . . 25
  - 5.1.1 Error Investigations . . . 26
  - 5.1.2 How to scale to 1 ppm error? . . . 27
- 5.2 Possibilities in enhancing the path length . . . 28
  - 5.2.1 Increasing Crystal dimensions . . . 28
- 5.3 Reflections . . . 29

5.3.1 Effects of using reflections on the Faraday rotation . . . 29
5.3.2 Multiple reflections to increase the gain . . . 33

6 Further Improvements **39**
6.1 Compensation schemes . . . 39
6.2 Wavelength and Power Considerations . . . 41
6.3 Faraday based current sensor versus Fluxgates . . . 42

7 Conclusions and Outlook **44**
7.1 Conclusion . . . 44
7.2 Outlook . . . 44

Bibliography **47**

Appendix **55**

A Sensor Requirements ASML **55**

B Theory **56**
B.1 Dielectric Tensor . . . 56
B.1.1 Microscopic Dielectric Tensor . . . 57
B.2 Spin-Orbit Coupling . . . 57

C Jones Formalism **58**
C.1 Jones Formalism . . . 58
C.1.1 Optical Elements . . . 58

D Error scaling **60**
D.1 Scaling Error . . . 60
D.1.1 Effect of multiple outputs . . . 60

E Error **62**
E.1 Noise Terms . . . 62
E.1.1 Shot Noise . . . 62
E.1.2 Johnson-Nyquist Noise . . . 62
E.1.3 Mechanical Vibrations . . . 63
E.2 Total Error Calculation . . . 64
E.2.1 Parameters . . . 64
E.2.2 Further mathematical tricks . . . 64
E.3 Optimum path length . . . 65

F Calibrations **66**
F.1 Aligning the Optical Setup . . . 67
F.2 Thickness TGG . . . 67
F.3 Magnetic field determination Sweep . . . 67
F.3.1 Averaging vs. Sweep . . . 67

G TGG Error Measurements **70**
G.1 Temperature Dependence . . . 70
G.2 FFT . . . 71

H Crystal Path length **73**
H.1 Non-Linear behavior . . . 73

I Reflections **75**
I.1 Influence Mirrors experiment 75
I.2 Magnetic field drop 76
I.3 High Reflectance 76
I.4 Total Internal Reflection 77

J Indepth Outlook **79**

Chapter 1

Definitions

1.1 Definitions

This section contains some definitions and abbreviations used in this report.

1.1.1 Polarization

The definitions for polarizations directions used are s- and p-polarized as shown on the left in figure 1.1. Where s-polarized light is perpendicular, and p-polarized light parallel to the plane of incidence (light grey area). As an example a reflection from an interface is shown in the right. They are also known as TE (s) and TM (p) modes.

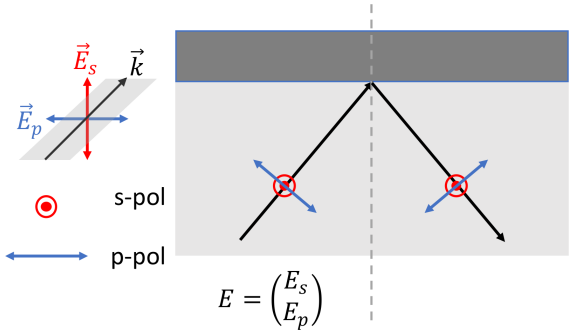

Figure 1.1: The light composed of s- and p-polarization on the left. A schematic overview of a reflection of this light from an interface on the right. The place of incidence is the light grey area in both figures. In red the s-polarization perpendicular to the plane of incidence and in blue p-polarization parallel to the plane of incidence.

1.1.2 Error and Noise

In this thesis total error is defined as the normalized sum of all stochastic and deterministic fluctuations. These are added up according to their nature, e.g. stochastic is 68% and deterministic is 100% uncertainty. Moreover, the deterministic fluctuations can have directions that may compensate. The terms Linear Error (LE) is used to describe deterministic effect that do not scale with the signal. The term Sum Square Noise (SSN) is used to describe all other effects that do scale with the signal. Most of the SSN in stochastic. Noise is considered an error but error is not considered a noise.

1.1.3 Synonyms in literature

Gain = Sensitivity (of the current sensor)

1.1.4 abbreviations

BS = Beamsplitter (Setup)
CF = Crystal field
DM = Differtial Mode (Often called RF instead)
FOM = Figure of merit (ratio Verdet/linear absorption coefficient)
FR = Faraday Rotation
GMI = Giant magneto impedance
HR = High reflective
LCP = Left circular polarized (light)
LE = Linear Error (This does not scale with the gain and can have a direction. Generally 100% uncertainty)
Measurement resolution = smallest rotation that is distinguishable from background fluctuations
MO = Magneto-Optic
Monitors = The + and − outputs of the balanced photodiode.
MS = Mirror (Setup)
NSD = Noise Spectral Density
P = Polarizer
PBS = Polarizing Beamsplitter
PIC = Photonic integrated circuit
PR = Phase retarder (Generally refers to a half-wave plate)
RCP = Right circular polarized (light)
RE = Rare earth (metal)
RIG = Rare earth Iron Garnet
SO = Spin-Orbit
SSN = Sum Square Noise (Noise that scales with the gain and generally has no direction. Additionally, it generally adds up as the root sum of the squares (68% uncertainty))
TAG = Terbium Aluminium Garnet
TE = Transverse electric
TGG = Terbium Gallium Garnet
TIR = Total internal reflection
TM = Transverse magnetic
TSAG = Terbium Scandium Aluminium Garnet
YIG = Yttrium Iron Garnet

Chapter 2

Introduction

Chips are the brainpower of our computers, laptops and cell phones. There is a constant drive to make these devices faster, cheaper, smaller and more efficient. Currently the smallest features of these chips have reached the size of several dozens of atoms. Consequently, manufacturing becomes increasingly complex. ASML is a company which takes a leading position in making the machines that are used in manufacturing wafers with details at the nanometer scale. Their machines use a process, called lithography, where features are imprinted on a wafer by exposing it to a light source. A wafer is fully patterned by changing its position relative to the light source using a wafer stage. To attain nanometer precision in the placement of all these patterns the movement of the wafer stage also requires nanometer precision. The current sensor is a crucial component in achieving the precision of the wafer stage.

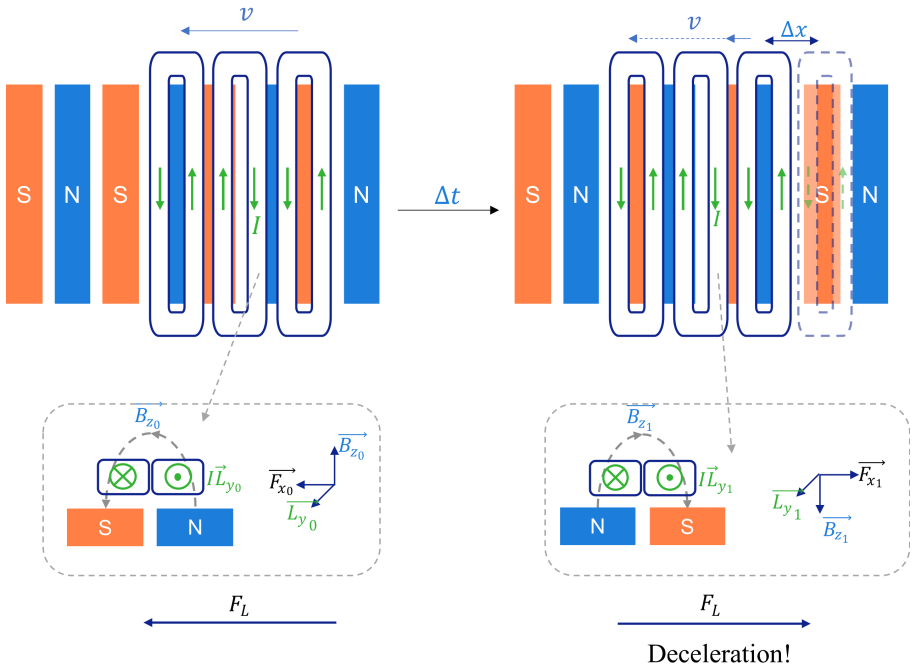

Figure 2.1: A schematic view of the movement of a wafer stage.

In figure 2.1 the movement of a wafer stage on top of an array of magnets is schematically shown. Attached to the wafer stage are coils (white belt) which are driven with precise currents, to generate a Lorentz force; $F = I\vec{L} \times \vec{B}$. On the left the Lorentz force points towards the left and a movement towards the left starts. After a time Δt the situation at the right is reached.

There the magnetic field is reversed causing the Lorentz force to become opposite to the movement causing deceleration. To prevent deceleration the current has to be reversed when the magnetic field changes sign. The speed at which this needs to take place depends on the speed of the wafer, v, and the distance between the magnets, Δx. Therefore, the current must be swapped within a time span of $\Delta t = \Delta x/v$. This is one reason why a high bandwidth is required, valid for the long stroke actuators that makes the large movements (> 1 μm). Corrections for instabilities in the movement of the long stroke are performed by the short stroke. It has a single coil and no significant movement w.r.t. the magnetic field, but high bandwidth is still required to counteract high frequent disturbances, e.g. due to flapping cables and resonances in the stiff structures. The challenge in positioning and moving the wafer stage at high precision, therefore, lies in applying both a precise and high frequency current. Unfortunately, errors of various origins can tamper accuracy. This requires constant adjustments to the current. For this, high temporal knowledge of the current is required. These can be measured using a specialized current sensor. This current sensor must be capable of measuring frequencies ≥ 1 MHz and with a noise spectral density (NSD) of only $0.1\frac{\mu A}{\sqrt{Hz}}$ on a current range of ± 100 A (see appendix A for a full specification list). The error on the output of a current sensor is the NSD integrated over the bandwidth of the current sensor. This means that the error normalized to the range of the current sensor (from now on called total error) cannot exceed $(0.1\frac{\mu A}{\sqrt{Hz}} * \sqrt{1MHz})/(100A) = 1$ ppm. This requirement has not been met by the commercially available current sensors yet. This work investigates the feasibility of using Faraday based current sensing to reach this target.

Table 2.1: The performance of different current sensing techniques. Retrieved from [1].

	Bandwidth	DC Capable	Accuracy	Thermal drift [ppm/K]	Isolated	Range	Power Loss
Shunt Resistor • Coaxial • SMD	MHz kHz-MHz	Yes	0.1% – 2%	25 – 300	No	kA mA – A	W – kW mW – W
Copper Trace[1]	kHz	Yes	0.5% – 5%	50 – 200	No	A – kA	mW
Current Transformer	kHz-MHz	No	0.1% – 1%	< 100	Yes	A – kA	mW
Rogowski Coil	kHz-MHz	No	0.2% – 5%	50 – 300	Yes	A – MA	mW
Hall Effect [1] (open-loop / closed-loop)	kHz	Yes	0.5% – 5%	50 – 1000	Yes	A – kA	mW
Fluxgate	kHz	Yes	0.001% – 0.5%	< 50	Yes	mA – kA	mW – W
AMR Effect[1] (closed-loop, core-less)	kHz	Yes	0.5% – 2%	100 – 200	Yes	A	mW
Core-less open-loop (GMR, AMR, Hall Effect)[1]	kHz	Yes	1% – 10%	200 – 1000	Yes	mA – kA	mW
Fiber-Optic Current Sensor[1]	kHz-MHz	Yes	0.1% – 1%	< 100	Yes	kA – MA	W

[1] Using temperature compensation electronics

In table 2.1 current sensors based on different technologies are compared. Currently, ASML uses Fluxgates with 5 ppm total error and a bandwidth up to 800 kHz. However, these Fluxgates are limited by the magnetization switching time of the magnetic core used. As a result, a bandwidth of ≥ 1 MHz cannot be achieved. Only 4 of the current sensors in table 2.1 have bandwidths that may reach the MHz; the shunt resistor, the current transformer, the Rogowski Coil and the Fiber-Optic Current Sensor. Shunt resistors are undesirable as they are in direct contact with the current wire. This is non ideal for safety and common mode voltage suppression (the currents flow in high voltage circuits with fast transients). The current transformer and the Rogowski coil require additional techniques for measuring DC currents, restricting their advantages. A method that has gained attention is the Giant magneto impedance (GMI) method with a large theoretical sensitivity and possible bandwidth up to tens of MHz [2]. Its NSD is expected to go below ~ 1

pT/$\sqrt{\text{Hz}}$ which is sufficient to reach the 1 ppm total error [3]. However, the requirement for an ultra low error and extremely high frequency (up to 100 MHz) carrier current limits the performance of the GMI and heavily increases the costs. Furthermore, GMI sensors having a bandwidth of at least 1 MHz have yet to be proven [4]. The Faraday based fiber-optic current sensor may be the technique with the highest potential to reach the target. It involves the Faraday effect where a polarization change in light is caused by the magnetic field of the current. Most of the present Faraday based current sensors are developed for the high power industry capable of measuring currents of kA with accuracies of only 0.1% [5]. Unfortunately, these designs all perform poorly for smaller currents [6]. The glass used in the fiber has a small sensitivity. Therefore, large lengths of the fiber around the current wire are required for sufficient signal. These large path lengths and the bend induced linear birefringence of the fiber limit the sensitivity at low currents [7]. An alternative to the fiber-optic current sensor is the Faraday based bulk-optic current sensor [8]. There the bulk materials have a much larger sensitivity than the glass used in fibers. This reduces the necessary path length and allows for higher sensitivity to smaller current. NSDs of 500 nA/$\sqrt{\text{Hz}}$ with bandwidth $>$ 10 MHz have been proven for bulk Gallium doped Yttrium Iron Garnet (Ga:YIG) based sensor but are still a factor 5 away from the desired 1 ppm [9, 10]. A theoretical analysis of a bulk Rare earth Iron Garnet (RIG) based Faraday current sensors showed a possible total error of only 4.9 ppm [11]. However, the ferromagnetic Ga:YIG and RIG have a non-linearity up to 1% due to hysteresis effects. Also saturation limits the range of the sensor. Additionally, temperature effects of the crystals on the gain of the sensor can be up to several 100 ppm/K [12, 13]. In a recent study, Rietman et al. discussed the feasibility of using the paramagnetic material Terbium Gallium Garnet (TGG) [14]. In particular, they argued that the possible bandwidth is in the GHz [14].

This thesis focusses on a bulk Faraday based current sensor. The Faraday based current sensor is theoretically estimated to have a total error roughly twice that of the best available the Fluxgate. However, the main benefit is that the Faraday based current sensor can reach bandwidth far above the 1 MHz. One the possible applications is as a magnetic field sensor for spintronic devices [15]. Electron microscopes can shorten the exposure time of a (organic) sample if short electron pulses can be measured. High frequency pulsed lasers, currents or other application that require current modulations of several MHz or above may want to use Faraday current sensor to monitor the modulations [16]. In particular, the GMI may benefit from a Faraday current sensor in its required modulation.

2.1 This thesis

Chapter 1 presents some definitions and abbreviations used in this thesis. In chapter 3 the Faraday effect is explained. Also the concept of a Faraday based current sensor is presented. Materials that can be used in the current sensor are discussed and TGG is argued to be one of the most realistic material to use for a small current sensor. The measurement setup and methodology is discussed in chapter 4. An optical bridge is employed to measure the Faraday effect due to its low error and simplicity. In chapter 5 a proof of principle using a TGG based current sensor with a total error of 3% is demonstrated, using simple peripheral equipment. This total error is reduced further by increasing the path length that the light travels through the TGG. This is done in two ways: Firstly, increasing the total crystal size and secondly, using reflections which benefits from the non-reciprocity of the Faraday effect. A linear increase in the gain is measured by increasing the path length through the crystal length. Furthermore, a simple increase in the gain of a factor ~ 1.7 has been experimentally achieved using reflections. This is theoretically worked out for a large amount of reflections. It is predicted to give a total error of 280 ppm if a compensation scheme is used. Unfortunately, the total error is limited by a temperature drift of 240 ppm. Possible designs for a compensation scheme are discussed in chapter 6. The effect of improving the total error at large bandwidths is shortly discusses with further calculations. This is compared to a Fluxgate showing that the Faraday current sensor perform worse at low frequencies, but the higher possible

bandwidth makes it attractive nonetheless. Finally, the conclusion is given in chapter 7 with an outlook for further research.

Chapter 3

Faraday Effect

The principle of a Faraday based current sensor is to probe the magnetic field of the current by measuring its effect on the polarization of light; the Faraday effect. It produces a rotation in the polarization state of light by converting s- to p-polarization or vice versa. Its magnitude is directly proportional to the magnetic field. In this chapter the underlying physics of the Faraday effect and its consequences for a current sensor will be discussed.

3.1 Phenomenological Description

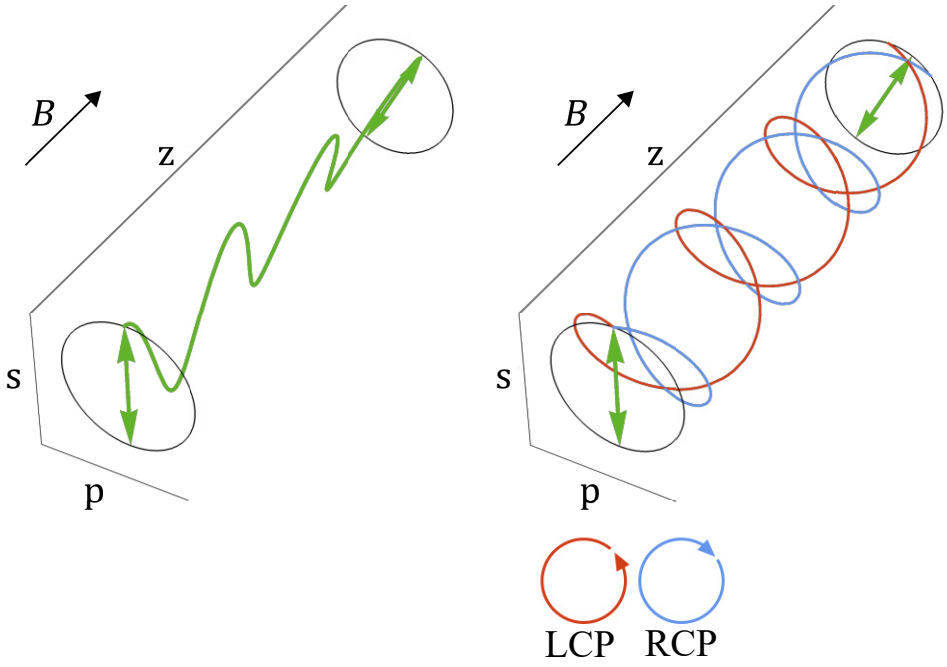

Figure 3.1: The Faraday effect on polarized light entering a medium in a magnetic field, B, parallel to the direction of propagating light (z-axis). On the left linear polarized (green) light experiences a rotation converting s- into p-polarization. On the right, the behaviour of both left circular (LCP) and right circular (RCP) polarized light is shown.

A more thorough derivation of Magneto-Optics can be found in the paper of Bennett [17]. For more information on magnetism see Magnetism and Magnetic Materials by Coey [18]. The

Faraday effect is a Magneto-Optic effect (MO) where linear polarized light travelling through a carrier material experiences a rotation when a magnetic field is applied. This is shown on the left in figure 3.1. This rotation is caused by the different speeds at which left- and right-circular polarized light move through a medium that is placed in a magnetic field. Linear polarized light can be written as a superposition of both left and right circular polarized light. The rotation is defined as the accumulated phase difference between LCP and RCP. Thus, the Faraday rotation can be described as

$$\theta = \frac{\omega L}{2c}(n_R - n_L), \tag{3.1}$$

where ω is the angular frequency of the light, c the speed of light in vacuum and L the path length that the light travels through the material, n_R and n_L are the refractive indices of RCP and LCP, respectively. The magnetic field influences the difference between the refractive indices in equation 3.1. This is described by the dielectric tensor which is further explained in appendix B.1. In a linear approximation equation 3.1 can be rewritten as

$$\theta = \mathcal{V} \int_L B \cdot dl, \tag{3.2}$$

where $\mathcal{V}$ is the material dependent Verdet constant and $\int_L B \cdot dl$ is the integrated magnetic flux density along the path of the propagating light at a total path length L. A typical values for the Verdet constant is -130 rad/(T.m) for Terbium Gallium Garnet (TGG) [19]. Commonly used BK-7 glass, however, has a Verdet constant of only 4.30 rad/(T.m) [20]. This wide range of possible values of the Verdet constant gives possibilities to design the response of the current sensor. This difference is caused by the Spin-Orbit coupling that is higher for rare-earth metals such as Terbium in the TGG. This will be discussed further in section 3.3.

An important property of equation 3.2 is its non-reciprocity. This means that when the light reverses its direction through, e.g. a reflection, the light continues to rotate in the same sense. This is because the magnetic field is also reversed allowing the rotation to accumulate through e.g. reflections.

3.2 The Faraday Based Current sensor

In figure 3.2 the proposed concept of the Faraday current sensor is schematically shown. Its properties are shown in table 3.1 which will be discussed throughout this thesis. The current to be measured, I_P, generates a magnetic field B_P. B_P causes a Faraday rotation, θ_F, in an optical setup, shown in red. In the optical setup light generated by a laser passes a polarizer. Next it experiences the Faraday rotation in the sensor head. The latter contains a crystal that is exposed to the magnetic field. The light passes a phase retarder and is split by a Wollaston prism. The resulting two beams are converted into three currents by two photodiodes ($\pm$). Combined they generate an output proportional to the Faraday rotation. This output is converted to a voltage that is transformed to a digital signal using an analog-to-digital converter (not shown). This digital signal is processed to obtain the measured current, I_P. Its result can be used to create a feedback current I_f generating a magnetic field B_f that is invoked on the crystal. The purpose of this feedback is to keep the output in a linear regime where both the gain is high and the total error is low. This is further discussed in section 6.1.

In short, the performance of the Faraday based current sensor is mainly influenced by four items; the magnetic field generation, the induced Faraday rotation, the measurement resolution of the Faraday rotation and temperature drift. The magnetic field generation involves the magnetic field that is experienced by the crystal. It is described by a magnetic field gain of $G_B = \frac{B}{I}$ in units T/A. In effect, the induced Faraday rotation is the coupling of this magnetic field with the crystals properties, Verdet constant, and the length of the path that the light travels through this crystal.

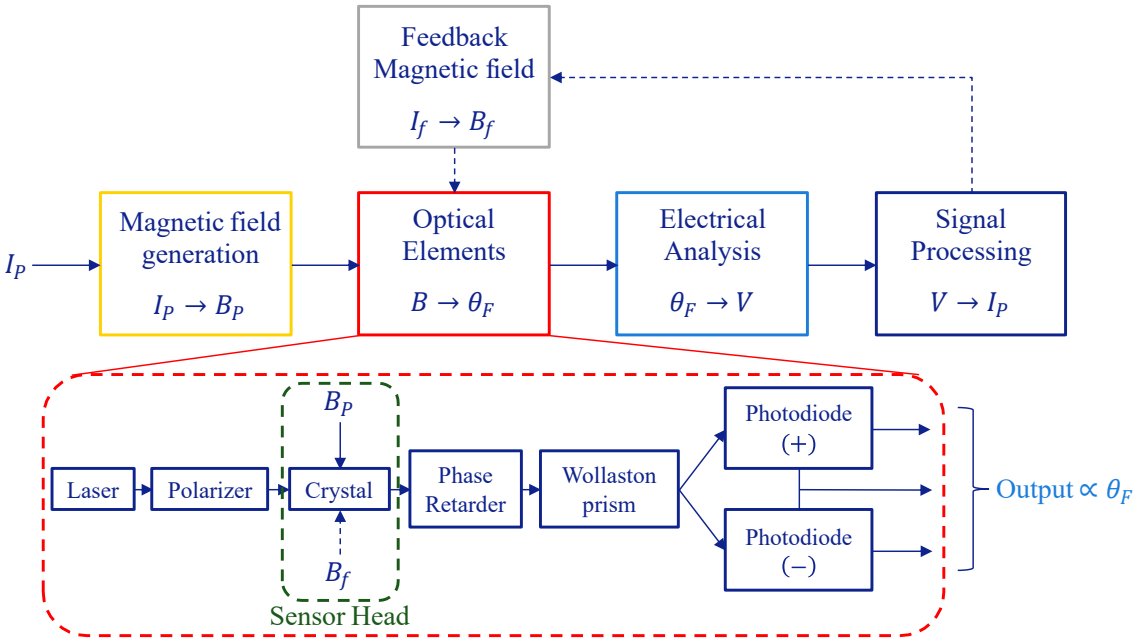

Figure 3.2: A schematic overview of a Faraday based current sensor. The transformation of the current I_P to obtain its value. The Faraday rotation is obtained in the optical setup shown in detail at the bottom.

The gain associated with the induced Faraday rotation using equation 3.2 is denoted by $G_{FR} = \frac{\theta_F}{B} = \mathcal{V}L$ in units rad/T. The measurement resolution of the Faraday rotation determines the minimal Faraday rotation, σ_{θ_F}, that can be separated from background fluctuations. Temperature drift impacts the output by changing the gain. This includes effects such as thermal expansion of the crystal increasing the path length and wavelength drifts of the laser. The normalized total error of the current sensor is defined by

$$\frac{\sigma_{I_P}}{I_{P,max}} = \frac{\sigma_{\theta_F}}{\theta_{F,max}} + \kappa = \frac{\sigma_{\theta_F}}{G_B G_{FR} I_{P,max}} + \kappa, \tag{3.3}$$

where σ_{I_P} is the minimal detectable current to be measured, $I_{P,max}$ is the maximum current to be measured (e.g. 100 A), $\theta_{F,max}$ the maximum Faraday rotation associated with the maximum current and κ the normalized temperature drift. By increasing G_B and G_{FR} and by decreasing σ_{θ_F} the first term of the total error can be lowered, but the temperature drift is generally independent on the gains G_B and G_{FR}. Because the temperature drift does not dependent on the gain it will be treated separately. The largest temperature drift originates from the Verdet constant and is discussed in section 3.3.2. Next, a first estimation of the Faraday effect is provided.

3.2.1 Estimations of the Faraday effect

The magnetic field from a straight current carrying wire (See figure 3.3) is denoted by Ampère's law as

$$B = \frac{\mu_0 I_p}{2\pi r}, \tag{3.4}$$

where μ_0 is the vacuum permeability, r is the radial distance from the wire carrying current I_P. The wire can also be placed in an U shape as shown on the right in figure 3.3. Positioning the wire in a coil line configuration is not preferred as winding currents can interact with each other through their parasitic capacitance. For $I_P = 100$ assume the light travels through a 5 mm TGG crystal with a gain of $G_{FR} = -0.65$ rad/T. The crystals is placed at a distance of 3 mm from

Table 3.1: Parameters of the Faraday based Current sensor

Parameter	Value
Verdet constant	-130 rad/(T.m)
Wavelength	633 nm
Crystal length	5 mm
Number of reflection	100
Laser Power	20 mW
Magnetic Gain (G_B)	0.1 mT/A
Sensor Head Gain (G_{FR})	-65 rad/T
Total gain ($G_B * G_{FR}$)	-6.5 mrad/A
Range	> 100 A
Noise Spectral Density	$0.9\frac{\mu A}{\sqrt{Hz}}$
Temperature drift, κ (at $\Delta T = 0.05$ K)	240 ppm
Bandwidth	≥ 1 MHz
Est. Cost	$\sim 2000 - 3000$ €
Ideal total error	9 ppm
Total error with κ	249 ppm

the current, I_p, carrying wire centre. The magnetic field in the crystal is roughly ~ 7 mT for the straight wire and ~ 10 mT for the U shape [21]. Then the Faraday rotation for a single pass is roughly 4.55 mrad or 6.5 mrad, respectively. Because the magnetic field of the U shape is higher it will be used in this thesis. This gives a magnetic field gain of $G_B = 0.1$ mT/A. To obtain a total error of 1 ppm rotations of $6.5\text{mrad} * 1\text{ppm} = 6.5$ nrad need to be distinguished if temperature drift is neglected. Measuring rotations down to several nrad is possible, but only when the bandwidth of the setup is severely limited [22, 23].

Because the current wire cannot be wound up in a coil due to parasitic effects G_B is limited. The two other options to reach low total error at high bandwidth are increasing G_{FR} and reduce the measurement resolution, σ_{θ_F}. Possibilities for increasing G_{FR} is to increase the Verdet constant or increase the path length. The measurement resolution can be lowered by optimizing the measurement setup. This proves to be difficult due the particle effects of the light (photons) and current (electrons). It invokes statistical fluctuations in the detection, called shot noise. This limits the measurement resolution to roughly $10\mu rad$ at 1 MHz bandwidth [24]. This will be further discussed in section 4.1.1. Ideas for enhancements are given in section 6.2. As a result, it is assumed impractical to measure 6.5 nrad. On the other hand, increasing G_{FR} through the Verdet constant and the path length will be the best methods to reach the desired total error of 1 ppm. In the next section the possibilities of enhancing the Verdet constant are discussed. The microscopic origin of the Faraday effect is examined. Furthermore, the effects of the wavelength and temperature on the Verdet constant are shown.

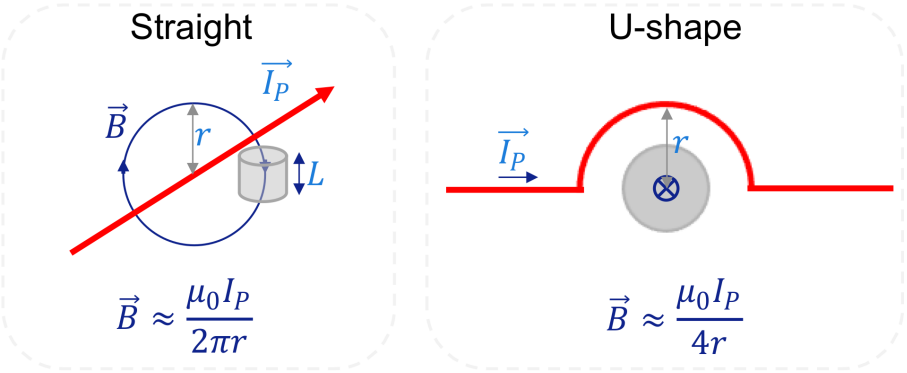

Figure 3.3: A magnetic field generated by a straight current carrying wire going through a crystal of length L at a distance r. On the right a wire is positioned in a U shape with the crystal placed inside the U shape.

3.3 Microscopic Origin

Up till now only a macroscopic description of the Faraday effect has been given. The microscopic origin of the Faraday effect originates from the Spin-Orbit (SO) coupling. This SO coupling induces a correlation between the orbital momentum L and spin momentum S of a electron in a material. This coupling allows the projection of the orbital momentum of right- and left-circular polarized light, $L = +1$ and $L = -1$, respectively, on a free electron to also probe the spin. Thus, when the number of up-spins in a material is unequal to the number of down-spins RCP and LCP will interact differently with the material. This gives rise to the Faraday effect. The higher this difference between spins the larger the Faraday effect. In a crystal, however, the electrons interact with neighbouring atoms and electrons reducing the orbital motion of the electrons through e.g. crystal field effects. This reduces the chance of the projection of the orbital momenta of RCP and LCP on the electrons. Therefore, materials with a well defined orbital momentum L are preferred. Because of the screening of the crystal field by higher lying electronic shells, rare earth (RE) metals have well defined orbital momenta for the optical transitions. Well defined orbital momenta in addition to strong Spin-Orbit coupling make REs prime candidates for the Faraday effect.

3.3.1 Spin Orbit Coupling

In figure 3.4 the relativistic origin of the SO coupling is shown. From the nucleus point of view the electron is orbiting it. However, when considering the point of view of the electron, it is the nucleus that orbits around the electron. This orbiting of the nucleus generates a magnetic field that interacts with the spin of the electron. Hence, the orbital movement (L) and the spin (S) of the electron are now coupled, i.e. SO coupling. The Hamiltonian of the SO coupling of a single electron can be described by

$$\mathcal{H}_{SO} = \frac{\Lambda_{SO}}{\hbar^2} \hat{L} \cdot \hat{S}, \tag{3.5}$$

where Λ_{SO} is the Spin-Orbit coupling constant. The coupling constant scales with the atomic number Z as $\Lambda \propto Z^4$. This scaling is explained in appendix B.2. Heavier elements, therefore, exhibit a strong coupling and lighter elements a weaker coupling. This is one of the reasons why the Verdet constant is higher for a crystal containing the heavy RE metal Terbium ($Z = 65$) compared to that of glass of which the heaviest element is Silicon ($Z = 14$).

In addition to the SO coupling the Coulomb interaction with nearby atoms, e.g. the crystal field (CF), also influences the orbitals in which the electrons move. The CF can contribute additional effects that couple the spin and orbits or decouple them by quenching the orbital angular

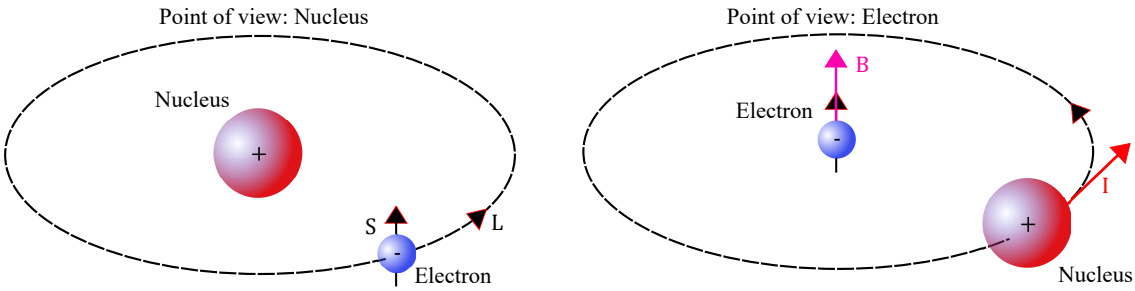

Figure 3.4: An electron orbits the nucleus (lef) when looking from the nucleus point of view with orbital moment L and spin S. On the right the Nucleus orbits the electron when looking from the electrons point of view.

momentum [25, 26]. In ferromagnetic $3d$ ions, such as Fe and Co, the crystal field causes the orbital angular momentum to be quenched. This low orbital momentum means that the optical coupling will be reduced significantly even though the highly localized density of states allows for large spin splitting [27]. For rare earth (RE) metals, such as Terbium, only the $4f$ electrons contribute to the magnetic effects and the $4f \rightarrow 4f5d$ transition causes the Faraday effects. Those electrons are located deep in the atom and are shielded from the surrounding electrons by the outer $6s$ and $5p$ electrons [28]. This makes RE metals less susceptible to possible quenching effect of the crystal field. Therefore, RE metals in crystalline form or applied as trace elements are interesting materials for the Faraday based current sensor.

The effect of the SO coupling is schematically shown in figure 3.5, For simplicity the CF effects are neglected. The ground state with orbital angular moment $L = 1$ and spin moment $S = 1/2$ is split into a state of $J = L + S$ and $J = |L - S|$. For this case no Faraday effect is observed as both RCP and LCP can interact with the same degenerate energy level. The situation changes when a magnetic field B_{ext} is applied. This causes Zeeman splitting lifting the degeneracy. Assuming the Zeeman effect to be weaker than SO and CF effects and orbital quenching is small then J is the proper quantum number. In this case the Zeeman splitting can be described as

$$\Delta\varepsilon_Z = \mu_B g_J B_{ext} m_J, \tag{3.6}$$

where μ_B is the Bohr magneton, m_J is the magnetic quantum number and g_J is the Landé g-factor. This splitting is schematically shown on the right side in figure 3.5 for the different spins. In the spin-up case the transition with LCP is lower in energy and for the spin-down case the RCP has a lower energy. By tuning the difference in the number of up-spins $N_\uparrow$ and down-spins $N_\downarrow$ a selection between RCP dominated or LCP dominated induced transitions can be made. This difference between the number of spins is not only affected by the Zeeman effect but also by the exchange interaction between spins, denoted by $-\mathcal{J}\hat{\mathbf{S}}_1 \cdot \hat{\mathbf{S}}_2$. Furthermore, the superexchange interaction with electrons of next to neighbour atoms can be used to enhance the difference between spins. The exchange interaction is large for elements with high J. This is the case for most REs except for Sm and Eu. The super exchange can occur in materials such as Garnets, in which the RE embedded as trace elements, interact with each other through the p-orbitals of the oxides [29–31].

Loosely speaking the Faraday effect can be enhanced by increasing the SO coupling, with the aid of heavier atoms. The prime candidates are the RE metals. The increased SO coupling in combination with a large difference in the spin occupation between up and down allows for the Verdet constant to increase. In effect, this results in a larger sensitivity of the Faraday based current sensor.

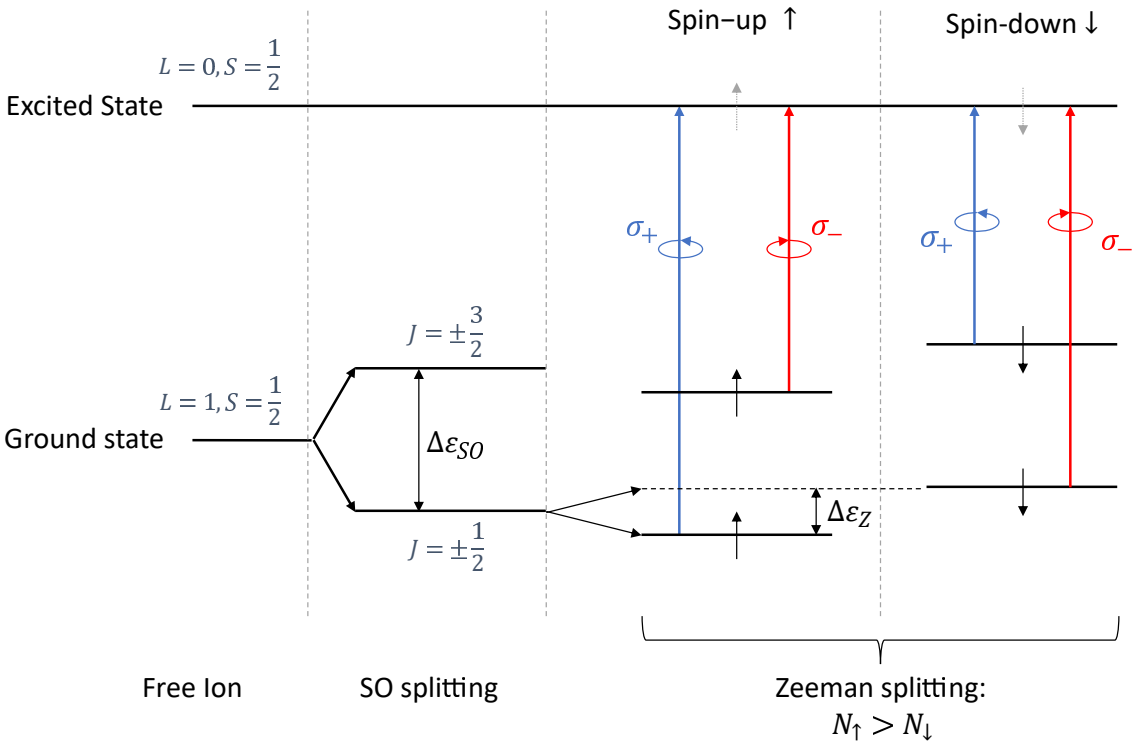

Figure 3.5: A simplified energy diagram of a ground state and excited state. On the far left a free ion without SO coupling is shown. The proper quantum numbers are L and S. Next, the SO splitting of energy $\Delta\varepsilon_{SO}$ is shown. The proper quantum number is now J. No splitting occurs in the excited state due to $L = 0$. This is done for simplicity. To the right the Zeeman effect is introduced causing a splitting, $\Delta\varepsilon_Z$, between spin up (middle right) and spin down (far right). The allowed transitions when considering the selection rules, $\Delta l = \pm 1, \Delta s = 0$, are shown in RCP (blue) and LCP (red) for both spins.

3.3.2 Wavelength and Temperature dependency

Choosing a material with a large amount of RE is not the only relevant parameter. As shortly discussed in section 3.2 the temperature drift is also a relevant aspect of the total error. The effect of a temperature drift is also present in the Verdet constant through its wavelength and the direct temperature dependencies. For the full theoretical considerations on the effect of the temperature and wavelength see [32]. The wavelength of the incident light λ influences the transition probability between the ground and excited state of figure 3.5. A larger difference between the applied wavelength with the transition wavelength λ_0 will reduce the probability of the light interacting with the electrons associated with this exact transition. This effect can be approximated for a paramagnetic material dominated by a single transition. This is described by

$$\mathcal{V}(\lambda) = \frac{F\lambda_0^2}{\lambda^2 - \lambda_0^2} + G, \tag{3.7}$$

where λ_0 is the transition wavelength, F is a material specific mixing constant and G is a constant that accounts the influence of a finite fixed temperature. In figure 3.6 the wavelength dependency of the Verdet constant of four different materials is shown. All materials had a transition wavelength in the UV ($\sim 200 - 400$ nm) coming from the $4f \rightarrow 4f5d$ transition of the REs. This causes the Verdet constant to continues lower when using high wavelengths. The material PrF_3 has the overall largest Verdet constant in the ultra violet (UV, $< 400nm$) range. The Verdet constant of TGG and Tb_2O_3 in visible range (VIS, $400 < \lambda < 1100$nm) is roughly 1 order of

magnitude smaller than the material applicable in the UV range. However, the steepness of the wavelength dependency is much lower. Tb_2O_3 has a larger overall Verdet constant than TGG. The final material is EuF_2 which is transparent in the near infra-red (NIR, $\lambda > 1100$ nm). It has the smallest Verdet constant but a much lower steepness. In short, the higher the Verdet constant the higher the steepness, e.g. wavelength drift becomes larger.

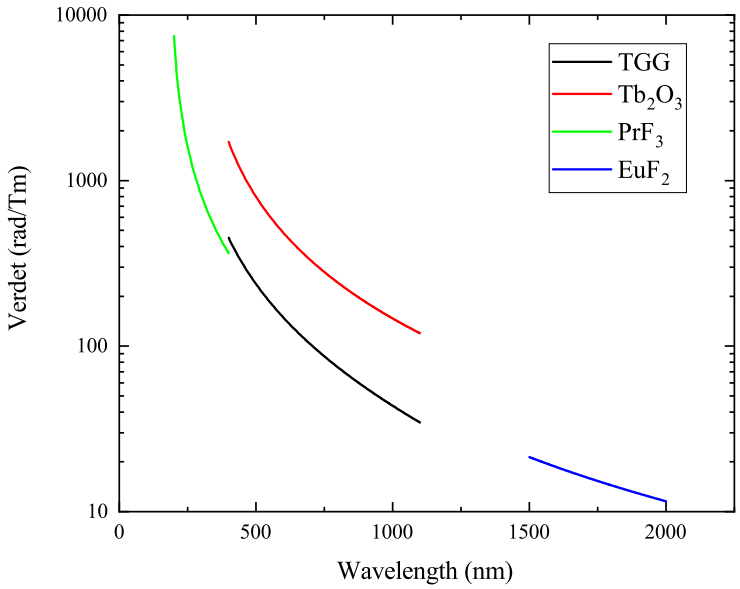

Figure 3.6: The Verdet constant dependence on the wavelength for different materials in their transparent regions. In black TGG and in red Tb_2O_3 in the visible (VIS) range. In green PrF_3 in the ultra violet (UV) range and in blue EuF_2 in the near infra red (NIR) range. Values derived from equation 3.7 using parameters adapted from [32].

In order to compare the materials a normalized wavelength drift of the Verdet constant is proposed as

$$\kappa_\lambda = \frac{1}{\mathcal{V}(\lambda)} \frac{\partial \mathcal{V}}{\partial \lambda} = -\frac{2F\lambda\lambda_0^2}{(\lambda^2 - \lambda_0^2)(F\lambda_0^2 + G(\lambda^2 - \lambda_0^2))} \tag{3.8}$$

in ppm/nm. In table 3.2 the normalized wavelength drift, from now on called wavelength drift, of the Verdet constant (κ_λ) for different materials and wavelengths is presented. It is adapted from [32]. The wavelength drift is the largest for wavelengths in the UV range ($\lambda < 400$ nm) with a minimum of 7100 ppm/nm. In the VIS range ($400 < \lambda < 1100$nm) this drift is roughly equivalent for all materials. At 1064 nm it differs a factor 2 from 633 nm. It is roughly a factor $2-4$ lower than UV. Looking at the NIR ($\lambda > 1100$ nm) the wavelength drifts are comparable. Similarly to the difference between UV and VIS, they are lower than the VIS range by a factor of 2-4. To limit the wavelength drift it seems obvious to use wavelengths in the NIR. However, the currently investigated materials in the NIR are scarce. In addition, the Verdet constant is roughly 1/10 that of materials in the VIS range. This makes them less desirable for a Faraday based current sensor. The UV materials have an even larger Verdet constant. However, their wavelength drift posses an additional challenge in the design of the current sensor. For instance, for a laser with a typical wavelength drift of 0.25 nm/K (HL6319G) and a temperature bath with temperature stability of 0.05 K the Verdet constant can change by $\sim 10000\text{ppm/nm} * 0.25\text{nm/K} * 0.05\text{K} = 125$ ppm. This is 2 orders of magnitude higher than the desired 1 ppm. For this reason a compromise is made by

Table 3.2: The normalized effect of a change in wavelength on the gain, κ_λ, in ppm/nm for different wavelengths. Values adapted from [32] by using equation 3.8.

λ (nm)	238	308	633	1064	1550	1940
CeF_3	100000	16000	3800	2000	1400	1100
PrF_3	18000	10000	-	-	-	-
$LiHoF_4$	9200	7100	-	-	-	-
$LiYbF_4$	14000	9000	-	-	-	-
TGG	-	-	3800	2300	-	-
TSAG	-	-	3800	2000	-	-
TCZ	-	-	4100	2000	-	-
Tb_2O_3	-	-	3900	2000	-	-
EuF_2	-	-	-	-	1400	1100

selecting materials in the VIS. Also, as a further advantage is the extensive research on materials in the VIS [32, 33].

As mentioned before the temperature also affects the Verdet constant. Varying temperatures cause an difference between the number of up and down spins. For paramagnetic materials this is described by the Curie-Weiss law:

$$\mathcal{V}(T) = \frac{H}{T - T_w} + I_\lambda, \tag{3.9}$$

where H is a material constant proportional to the Curie constant, T_w is the Curie-Weiss temperature where a material loses its permanent magnetic properties becoming paramagnetic and I_λ is a constant that contains the contribution of a fixed wavelength λ. In figure 3.7 the temperature dependency of the Verdet constant at 633 nm for TGG is shown. At lower temperature the Verdet constant increases but the steepness of the curve also increases with lower temperatures. Similar to the wavelength the temperature drift of the Verdet constant can be described by

$$\kappa_T = \frac{1}{\mathcal{V}(T)} \frac{\partial \mathcal{V}}{\partial T} = \frac{H}{(H + I(T - T_w))(T - T_w)} \tag{3.10}$$

in ppm/K. TGG has a typical drift of $\sim 3000 - 4000$ ppm/K at room temperature. This increases up to 10000 ppm/K at T=100 K. For a typical temperature bath having a stability of 0.05 K this gives a equivalent error of 150 ppm and 500 ppm for 300 K and 100 K, respectively. Both are significantly higher than the desired 1 ppm. Thus, for a low temperature drift it is better to use high temperatures. Room temperature will be adopted to avoid the need for sophisticated temperature control. Typical temperature drifts for other materials adjacent to other relevant parameters are discussed in the next section to explore materials that can be employed in the Faraday based current sensor.

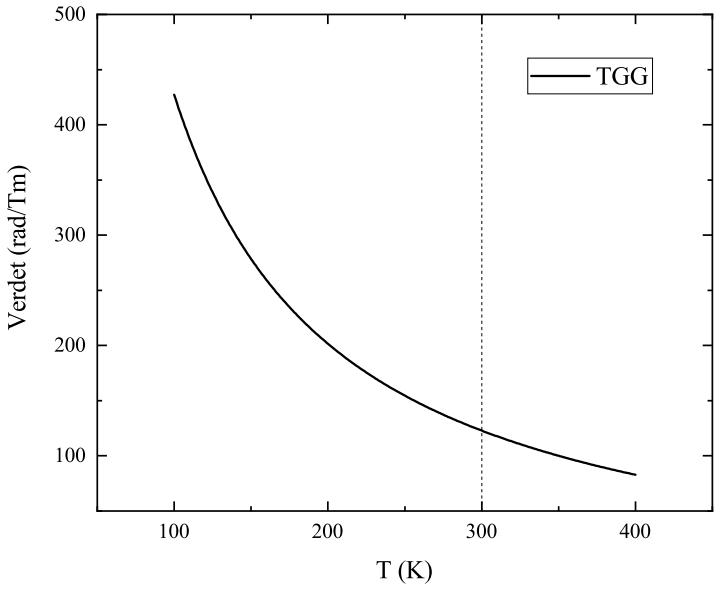

Figure 3.7: The Verdet constant versus the temperature for paramagnetic TGG at a wavelength λ of 633 nm. Room temperature, 300 K, is indicated by the vertical dashed line. Adapted from [34, 35].

3.4 Material Considerations

For the Faraday current sensor a material has to be selected that exhibits a large Verdet constant, a low wavelength drift and a low temperature drift. Equally important is a high transparency needed to detect enough light. The material parameter that determines this transparency is the linear absorption coefficient, μ. Actually, it limits the length of the path that the light can travel through the material. Subsequently, the Verdet constant and the maximum path length, L_{max}, limit the maximum gain ($G_{FR,max} = \mathcal{V}L_{max}$) of the current sensor. In order to quantify the applicability of a material the Figure of Merits (FOM) is introduced. It is defined as the ratio between the Verdet constant and the linear absorption coefficienct, μ: $FOM = \mathcal{V}/\mu \approx G_{FR,max}$ in rad/T. A quick estimation can be made to find the FOM necessary to reach the 1 ppm error of 10 mT (10 nT). Assuming the measurement resolution is 10 μrad with a bandwidth of 1 MHz then the FOM necessary is 10000 rad/T [22].

In table 3.3 a summary of various materials and their relevant properties is given. The material with the highest estimated FOM of 2200 rad/T is KT_3F_{10} followed by Glasses with a FOM of 1500 rad/T. At the third place TGG comes with a FOM of 384 rad/T followed by CeF_3 with a FOM of 123 rad/T. Materials such as Dy_2O_3 and Tb_2O_3 show significantly larger Verdet constants. Unfortunately, values for their absorption have not been found. The temperature drift at room temperature of most materials is around 3000 ppm/K with the exception of YIG and glasses. They have a temperature drift up to 2 orders of magnitude lower. The material used in this thesis is TGG mainly due to its commercial availability and, more importantly, its high Verdet constant at 633 nm. Because at path lengths surpassing ~ 1 m linear birefringence will become an significant issue, KT_3F_{10} and glasses were not chosen although they have a better FOM. This limit in the path length will be discussed in section 5.2. This makes materials with a high Verdet constant preferred. Tb_2O_3 shows the most potential as replacement of TGG due it Verdet constant being

Table 3.3: Estimations of the absolute Verdet constant $\mathcal{V}$, absorption coefficient μ, estimated maximum FOM with the associated maximum path length in brackets and temperature drift at room temperature κ_T, for different materials from literature. Values for the Verdet constant and absorption coefficient are taken at 633 nm for comparison except for YIG which is for 1310 nm. The FOM is an estimated maximum obtained from literature which is not necessarily at a wavelength of 633 nm.

Material	$\mathcal{V}$ (rad/(T.m))	μ (cm^{-1})	max. FOM (rad/T) (L_{max})	κ_T (ppm/K)	Reference
YIG	2200	4	5.5 (2.5 mm)	660	[12, 36]
TGG	130	0.01	384 (10 m)	3400	[19, 37, 38]
TSAG	165.8	-	-	-	[39]
TAG	179.3	-	-	-	[40]
EuF_2	190	-	-	-	[41]
KTb_3F_{10}	113	-	2200 (61 m)	3100	[42, 43]
CeF_3	123	0.01	123 (1 m)	-	[44]
$CeAlO_3$	270	-	-	3300	[45]
$Cd_{1-x}Mn_xTe$	2200	1	22 (1 cm)	5000	[46–48]
Dy_2O_3	347.5	-	-	3100	[32, 49–51]
Tb_2O_3	422	-	-	3100	[32, 49–51]
glasses	2-4	10^{-5}	1500 (1 km)	70	[52, 53]

much larger although its absorption has not been found. The properties of the materials will be discussed in more detail in the next sections.

3.4.1 Garnets

A group of materials often used in bulk Faraday current sensor are the garnets [9, 54]. The garnet structures are interesting due to the incorporation of magnetic sub-lattices. These allow for tailoring of effects such as the superexchange interaction [31]. YIG stands out in the garnets due to its large Verdet constant [36]. In YIG the iron sublattices dominate the magnetic properties but contrary to normal ferromagnetic materials the coercivity is very small [13, 55]. This allows for an almost linear response to an external magnetic field. Therefore, it is a popular material for Faraday based current sensing. However, due to finite coercivity the linearity of such sensor is heavily affected by hysteretic effects and magnetic saturation limits the range. Furthermore, the absorption is high giving a FOM significantly lower than TGG. A positive property is its low temperature drift being an order lower than TGG [12].

Because of the linearity issues paramagnetic garnets such as TGG are preferred although the Verdet constant is an order of magnitude lower than YIG [19, 38]. By exchanging elements in the garnet structure the Verdet constant can effectively be improved. An increase of 25% for Terbium Scandium Aluminium Garnet (TSAG) and 30% for Terbium Aluminium Garnet (TAG) with comparable absorption coefficient have been reported [39, 40, 56–58]. Further enhancement of up to 30% of the magnetic properties can be obtained by doping the garnets with rare earth metals [19, 29, 59]. Unfortunately, the temperature dependency for only a few paramagnetic garnet has been investigated. It is, however, expected that they will have roughly equivalent temperature drift of $\kappa_T \approx 3000$ ppm [60]. The temperature dependency could be reduced by combining crystals with opposite temperature dependencies as Zhao et al. have shown for YbBi:YIG lowering κ_T from 660 to 420 ppm [12].

3.4.2 Other Crystal Structures

Crystal structures that allow for rare earth metals to be incorporated in atomic sites are fluoride based crystals. For example, EuF_2 and KTb_3F_{10} have Verdet constants comparable to that of TGG [41, 43]. The properties enhance significantly near UV light [44]. However, in addition to issues with wavelength drift in the UV, typical detectors in the UV range have a lower quantum efficiency. This making UV based materials less interesting for high accuracy purposes such as the Faraday based current sensor. The crystal KTb_3F_{10} shows the most promise with a low absorption of 10^{-4} cm^{-1} and estimated maximum FOM of 2200 rad/Tm at 1064 nm [42].

Another crystal structure with potential is the Perovskite-type rare earth aluminite ($REAlO_3$). This structure allows for high density of rare earth ions with $CeAlO_3$ crystals have a Verdet constant that is roughly twice that of TGG and CeF_3 [45]. However, no estimations of the linear absorption coefficient could be found. The FOM could, therefore, not be estimate.

Another candidate is $Cd_{1-x}Mn_xTe$. Its Verdet constant is an order of magnitude higher thant TGG [46–48]. However, the high absorption limits the path length to a centimeter. This can be easily surpassed by an order of magnitude using reflections. There is, however, an engineering advantage to this materials. By tuning the amount of the $3d$ metal Mn (x) the properties can be changed. For instance optima can be found in temperature dependencies. For $Cd_{1-x}Mn_xTe$ this optimum is, however, at 5000 ppm/K which is roughly twice as high as TGG.

RE based Oxides such as Dy_2O_3 and Tb_2O_3 have Verdet constant up to 3 times higher than that for TGG [32, 49]. These materials contain a much larger RE content. Recently, the fabrications of these types of crystals has become feasible [50]. The temperature dependence is equivalent to TGG [51]. The absorption is, however, unknown but a higher FOM than that for TGG is expected.

Diamagnetic materials are interesting due the lower temperature dependencies. They are almost two order of magnitude lower than that for paramagnetic materials [52]. This makes them a preferred choice for temperature independent current sensors. For diamagnetic materials equation 3.9 does not apply. It is typically temperature independent or it can be neglected. On the other hand, the band-gap contains a slight temperature dependence that results in a relative wavelength shift compared to the constant wavelength of the laser [52, 61]. Diamagnetic glasses, however, have a Verdet constant that are almost 2 orders of magnitude lower than that for paramagnetic materials [53]. This makes them less suitable for small signals. The significantly lower absorption coefficient allows for extremely large path length of several 100 meters up to kilometers. Increasing the Verdet constant has been attempted by doping the diamagnetic glasses with REs. This has been proven, but at the cost of absorption [62]. Watekar et al. have even shown that using quantum dots as doping is feasible [63]. They were able to enhance the Verdet constant by a factor ~ 2.

Other materials with large MO effect are the Heusler compounds. The easy fine tuning allows for engineering of their large Kerr rotations [64]. Likewise, nanostructures such as nanorods have been theoretically estimated that they have a 3 orders of magnitude higher Verdet constant [65]. These may prove to be an interesting material to develop further. Solids are not the only option to use in a Faraday current sensor as Zhao et al. have shown that a ferrofluid can also be used [66]. A drawback is that they are severely bandwidth limited.

3.4.3 Material in this Thesis

In summary, TGG is used in this thesis due to the relatively high Verdet constant of -130 rad/(T.m), paramagnetic nature for linearity, path length limits up to 6 meters, temperature drift of comparable magnitude to other paramagnetic materials and its commercial availability [38, 59]. KTb_3F_{10} and glass show the most promise to replace TGG if the path length is capable

of reach up to 100 meters. The feasibility of this will discussed in section 5.2. A factor 3 increase can be achieved using Tb_2O_3 if its absorption is low enough.

The typical improvements discussed previously, however, are not enough to reach the desired FOM. It may, therefore, be more fruitful to lower the requirement on the FOM such as lowering the measurement resolution. In the next chapter the method of measuring the Faraday effect is discussed and the methodology for the experiments is given.

Chapter 4

Measurement Techniques

To relieve the requirements on the Verdet constant and on the path length it is essential that the optical detection is highly sensitive. In order to measure the Faraday effect there are two main detection schemes applicable: Polarimetry (Amplitude) and Interferometry (Phase). Only the former has been employed in this study. The latter is discussed briefly. Subsequently, the experimental setup and techniques are discussed.

4.1 Measuring the Faraday Effect

As discussed in the previous chapter the Faraday effect is a rotation of linear polarized light or, equivalently, is a phase shift between left- and right-circular polarized light. The rotation can be measured by comparing the horizontal and vertical electric field of the light. The phase shift measurement requires interfering two light beams and measuring changes in the fringe patterns.

4.1.1 Polarimetry

Measurement of the polarization rotation is carried out with polarimetry. A commonly used measurement setup is the optical bridge [23]. This is employed for this report. The setup for measuring the Faraday rotation is shown in figure 4.1. Laser light is sent through a polarizer (P). Next, it enters the crystal where it undergoes a Faraday rotation when a magnetic field is generated using a coil. The polarization rotated light is rotated further by 45 degrees using a phase retarder (PR). The polarized light is then split using a polarizing beamsplitter (PBS) into horizontal and vertical components. Afterwards, the intensity of the light is converted to currents $I_{D\pm}$ by means of the responsivity $R(\lambda)$ of two photodiodes. By connecting the output of the two photodiodes a differential current, $I_{D+} - I_{D-}$, is generated. All of these currents are converted to a voltage using transimpedance amplifiers. This gain is described by $G_{mon}(\omega)$ for the monitor ($\pm$) outputs and $G_{DM}(\omega)$ for the differential mode (DM) output. The output of the setup produces three different voltages ($V_{\pm}, V_{DM}$) which that are are proportional to the Faraday rotation.

The behaviour of this setup is characterized by looking at the evolution of the electric field of the light. This is done by using Jones formalism which is explained in appendix C. The polarizer is represented by the Jones matrix $P(\alpha)$ where α is the angle of transmission. For the Faraday rotation θ_F the Jones matrix $F(\theta_F)$ is used. The phase retarder with a retardance, η, and fast axis, θ_f, is characterized by the Jones matrix, $P_R(\eta, \theta_f)$. The splitting by the PBS is obtained by assuming the two outputs contain polarizers, $P(0)$ and $P(\pi/2)$, which rotation are $\pi/2$ apart. The electric field of the light coming from the laser, E_0, is transformed to an electric field, E_+ and E_-, that is incident on the photodiodes using

$$E_+ = P(\pi/2)P_R(\eta, \theta_f)F(\theta_F)P(\alpha)E_0 \tag{4.1}$$

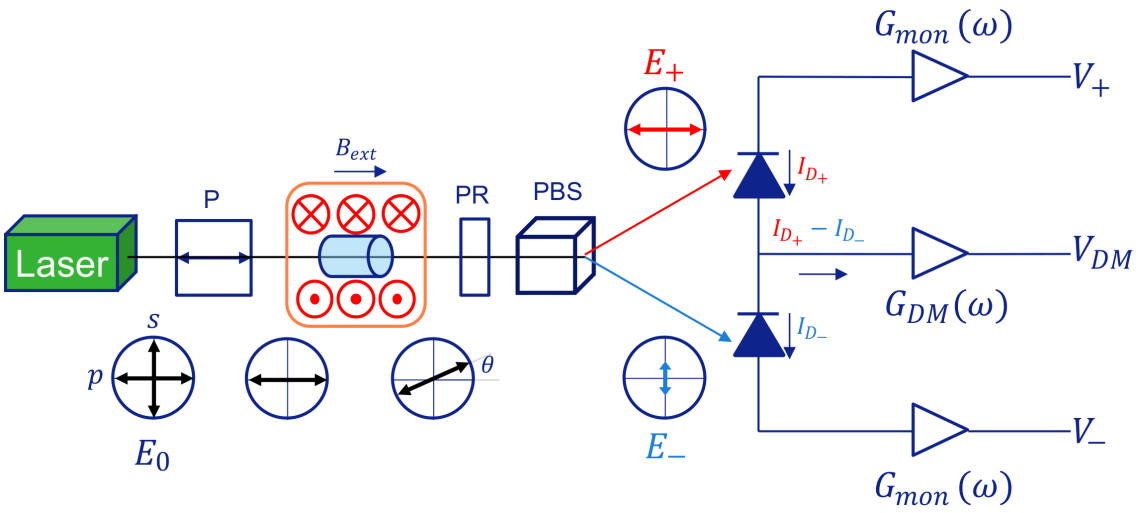

Figure 4.1: A schematic overview of the measurement setup. The evolution of the electric field components, s and p, as it goes through the optical elements is shown beneath the setup.

$$E_- = P(0)P_R(\eta, \theta_f)F(\theta_F)P(\alpha)E_0. \tag{4.2}$$

The intensity of the incident light falling on the photodiode is calculated using $J_\pm = E_\pm E_\pm^*$. This can be used to obtain the voltage at the monitor output: $V_\pm = R(\lambda)G_{mon}(\omega)J_\pm$ and the voltage output at the DM output: $V_{DM} = R(\lambda)G_{DM}(\omega)(J_+ - J_-)$. It can be shown that normalizing the intensity difference produces a relation between the three output voltages and the Faraday rotation θ_F, i.e.

$$\frac{J_+ - J_-}{J_+ + J_-} = \frac{G_{mon}(\omega)}{G_{DM}(\omega)}\frac{V_{DM}}{V_+ + V_-} = -\cos(\frac{\eta}{2})^2\cos(2\alpha - 2\theta_F) - \sin(\frac{\eta}{2})^2\cos(2\alpha - 4\theta_f - 2\theta_F). \tag{4.3}$$

This equation can be simplified significantly by using a half-wave plate with $\eta = \pi$ at an angle of $\theta_f = \pi/8$ as phase retarder. Together with rotating the polarizer angle to zero, i.e. $\alpha = 0$. This reduces equation 4.3 to

$$\sin(2\theta_F) = \frac{J_+ - J_-}{J_+ + J_-} = \frac{G_{mon}(\omega)}{G_{DM}(\omega)}\frac{V_{DM}}{V_+ + V_-}. \tag{4.4}$$

A major advantage of this relation is its independence of the laser power J_0. In practice, the measurement results are much less susceptible to the power fluctuations originating from the laser. In addition, for lower signals the error in V_+ and V_- can be neglected. Furthermore, the leakage current, i.e. dark current, of the photodiode is filtered out in the DM output if both photdiodes are similar.

A polarimetry setup like discussed above can be used to measure polarization rotations down to 10 μrad with 1 MHz bandwidth [24]. This is limited only by the shot noise on the current of the photodiodes. In section 5.1 a 0.5 mm TGG crystal will be used. Using equation 3.3 for a B-field of 10 mT this creates a maximum Faraday rotation $\theta_{F,max}$ of 0.65 mrad. Therefore, a total error of roughly $\frac{10\mu\text{rad}}{0.65\text{mrad}} \approx 1.5\%$ is expected. However, this only holds in the regime where equation 4.4 can be linearly approximated, e.g. $\sin(2\theta_F) \approx 2\theta_F$. For rotation $\theta_F \gg 0$ the error will start to deviate from this linear behaviour. This effect is discussed in Appendix D. There is is shown that when the maximum Faraday effect surpasses ~ 0.4 rad these modified designs are necessary to reach the 1 ppm. Also, rotation above $\pi/4$ rad are indistinguishable from rotation below $\pi/4$ rad due to the sinusoidal behaviour of the output. A counting mechanism can be added to in the signal processing in order to keep track of the integer of $\pi/4$. Non-linear regimes can be

avoided using multiple outputs, feedback mechanisms or autobalancing of the electronic gains (e.g. auto-balanced optical receivers). The multiple outputs and feedback mechanism are discussed in section 6.1. In the previous estimation the maximum Faraday rotation is 0.65 mrad. For this the assumption of linear scaling still holds. Increasing the maximum Faraday rotation by means of increasing the gain has priority. In section 5.3.2 the consequences of the non-linearity will be discussed further.

4.1.2 Interferometry

The phase difference between RCP and LCP is measured with an interferometer [67]. Bohnert et al. have shown that with an interferometer an accuracy of 0.1% is possible for high currents ($\gg$ 1 A) [68]. They found a minimum detectable magneto-optic phase shift of 1.325 μrad/$\sqrt{\text{Hz}}$. For a bandwidth of 1 MHz this results in a minimum detectable phase shift of 1.325 μrad/$\sqrt{\text{Hz}} * \sqrt{1\ \text{MHz}} = 1.325$ mrad [69]. Compared to the 10 μrad for polarimetry the interferometer performs much worse. Specifically, the expected Faraday rotation of 0.65 mrad for a current of 100 A will be impossible to distinguishable from the typical fluctuations of 1.325 mrad of the interferometer design. This makes the interferometer not feasible for measuring currents at high precisions below 1 kA. Besides, the high complexity, a high demands for stability of the optical source and the required modulation make the interferometer an unattractive measurement technique in the present study. Therefore, polarimetry is employed.

4.2 Experimental Equipment

The setup used in the experiments is depicted in figure 4.2. It is based on the schematic in figure 4.1. The laser diode, L658P040, is operated using a TLD001 driver at a wavelength of 658 nm and positioned in a LDM21 mount. Linear p-polarized light is obtained with a LPVISC050-MP2 linear polarizer. PF10-03-P01 silver mirrors are used to redirect the laser beam. A WPH05M-633 half-wave plate is applied as phase retarder to obtain the 45 degree rotation. Unfortunately, this half-wave plate is optimized for 633 nm which means that the retardance is not exactly π but 0.94π. This lowers the gain of the setup by roughly 0.9% compared to the ideal situation. In addition, this mismatch required a slight modification of the fast axis of the half-wave plate in order to remove asymmetrical behaviour. Such asymmetrical behaviour can introduce a difference between negative and positive rotation of 0.002% at $\pm$0.65 mrad increasing up to 0.2% at $\pm$65 mrad rotations. A WP10 wollaston prism with a lens is used to produce the polarization dependent splitting. A balanced photodiode (with bandwidth 1 MHz), PDB210A/M, is used to measure the light intensity and to obtain the three output voltages of equation 4.4. Voltages are measured with a NI PCI-6024E DAQ that is controlled using LabVIEW. The measurement points of the three outputs were obtained sequentially. Each set of points is taken at intervals of roughly 100 ms, i.e. a sampling frequency of $\sim$ 10 Hz. The measurements results are average values of all the data points obtained by the DAQ within this 100 ms. A major disadvantage of the sequential measuring is that there is a small amount of time between obtaining the measurements between the different outputs. This means that the laser drift within this small time will still be present in the measurement. In appendix G.2 this effect is discussed shortly. An Agilent 34410A with accuracy of 0.004% has been used to check the reliability of the DAQ. The total error of the DAQ was found to be $\sim$ 0.15 mV while the total error of the balanced photodiode was found to be $\sim$ 2 µV. The calibrations of the setup can be found in appendix F. The laser power was roughly 5 mW. The power that reaches the photodiodes, however, is reduced by the optical losses of the setup. The power picked up by the photodiodes is 2 mW. The laser power was reduced when the monitor voltages went above 8.5 V to avoid saturation occurring in one or more of the photodiodes. The alignment of the optical setup is shortly discussed in appendix F.1. An rough estimation of the cost shows that this setup would cost between 2000 and 3000 € when purchasing from commercial suppliers such as Thorlabs.

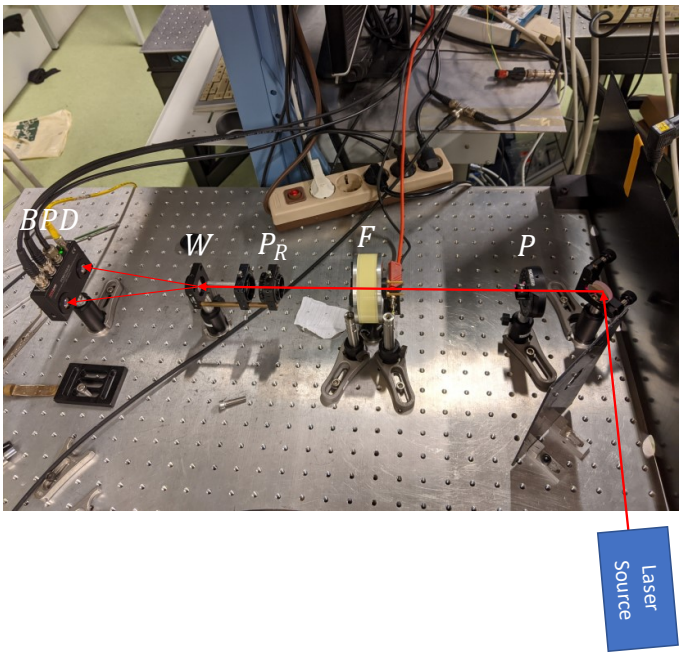

Figure 4.2: A photo of the experimental setup used in this thesis. A lens is placed in between the phase retarder, P_R, and the wollaston prism, W, to allow the wollaston prism to work properly.

4.2.1 Magnetic field

The magnetic field is generated using a coil with roughly 500 turns. The current is supplied using a Keithley 2400 with a maximum(minimum) supplied current of 1A(-1A). The accuracy of the Keithley 2400 at 1A is 0.27% and the error is 25 μA. The coil(s) are calibrated using a LakeShore 421 Gaussmeter with a LakeShore MMA-1808-VG axial probe with an accuracy of 0.2%. The range of the magnetic field generated is $\pm$25.75 mT. The magnetic field showed some dependency on the position inside the coil. This poses an inaccuracy of the magnetic field of about 0.3% and up to 3% for large deviations.

4.2.2 Samples

In the experiments TGG crystals from Chengu Dien Photoelectric Technology Co., LTD were used. Their dimensions are 10x10x0.5 mm. The light is send perpendicular to the 10x10 mm area. This means that the path length is only 0.5 mm. In literature both ceramic and single crystal TGG is used and, therefore, slight differences can be found when comparing to literature values [38]. Also in the literature a wavelength of 633 nm is generally used. However, the experimental setup in this report used 658 nm. This will decrease the Verdet constant as discussed in section 3.3.2. To correct for this the Verdet constant found in this report much be increased by roughly 7% when assuming roughly 0.3% per nm [19].

The glass plates were standard glass plate with a thickness of 0.95 mm. They were cut to fit a sample holder. The uncertainty of the measured thickness of the glass is 0.05 mm when using a caliper. The TGG thickness was measured using a micrometer with an accuracy of 0.001 mm. The values are presented in appendix F.2. The TGG samples where not marked making it difficult to identify which sample was used in what measurement. Therefore, the mean and the standard error of the mean of all TGG samples will be used when calculating the Verdet constant. The mean thickness of the TGG crystal with standard error is 0.506 ± 0.003 mm.

4.3 Experimental Methods

This section provides three methods used in this thesis to obtain relevant quantities, like the Verdet constant, error and reproducibility.

4.3.1 Measurements

The Faraday rotation is measured using two methods: averaging and sweeping. The first method is done by applying a constant current and measuring the output of the setup for about 10 s. The Faraday rotation is determined using equation 4.4. The mean is taken using a Matlab script. The measured rotation at 0 A is subtracted from each measurement point. A linear fit is subtracted from each individual measurement to remove some of the laser drift and to remove the offset. The residue is consider the error and the standard deviation is taken. In the second method a current sweep from -1 A to 1 A is carried out while a measurement is running. This methods had some issues. Firstly, the current applied could not be synchronized perfectly with the measurement of the voltages. Secondly, in the sequential reading different magnetic fields are present. These increase the uncertainty in the values for the magnetic field compared to the first methods. The approach to determine the magnetic field in this sweeping method is discussed in appendix F.3. The averaging method is found to have a non-linear residue after fit. This could be caused by temperature effects increasing the error by roughly 1.5%. This is discussed in appendix F.3.1. The sweep method does not have this issue. Thus, it is expected to give a better approximations. The response was found to be roughly 6% higher than the averaging method.

4.3.2 Error calculation

In previous sections the measurement resolution of the experimental setup was fixed to a value of 10μrad. To find out how to reduce the measurement resolution it is necessary to derive the contributions from different noise sources and error sources. Typical noise sources are the shot noise, Johnson-Nyquist noise and vibrations. These are discussed in appendix E.1. Error sources are the temperature drift discussed in section 3.3.2. Most error sources originate from different physical processes and have different SI units. It is necessary to normalize all these effects towards a common denominator. The effect of an absolute error term on the Faraday rotation is calculated to achieve this. This gives the contributions of an absolute error in terms of Faraday rotation. To normalize it is then divided by the maximum Faraday rotation $\theta_{F,max}$ as derived from the specified range of the current sensor, e.g. 100 A. The upper limit for the current sensor is taken to be the output at 10 mT, i.e. the U-turn of section 3.2.1. For example, the effect of shot noise on the current at the + monitor is calculated with

$$\frac{\sigma_{\theta_F}}{\theta_{F,max}} = \frac{\partial \theta_F}{\partial I_+} \frac{\sigma_{I_+,shot}}{\theta_{F,max}} \tag{4.5}$$

This equation has an analytic solution. However, some derivation could not be obtained analytically. In this case it will be calculated numerically in Mathematica. The error is considered the maximum difference between the output with the changed parameter due to fluctuations and the ideal output (or calibrated output) normalized to the range of the current sensor. The composition of the total error from the different error sources are discussed in appendix E.2. This method will be used to derive so-called Pareto graphs where the contribution from different error sources are compared.

Chapter 5

Results and Discussion

In this chapter a simple measurement to investigate the performance of Faraday based current is shown Its error components are investigated. A strategy is adapted where the path length will be improved. The crystal length is increase for both TGG and glass. Next, a simple measurement using reflections will be discussed. Finally, theoretically designs for multiple reflections are discussed. The results will be used in the next chapter when comparing to a Fluxgate.

5.1 Faraday based Current sensing using TGG

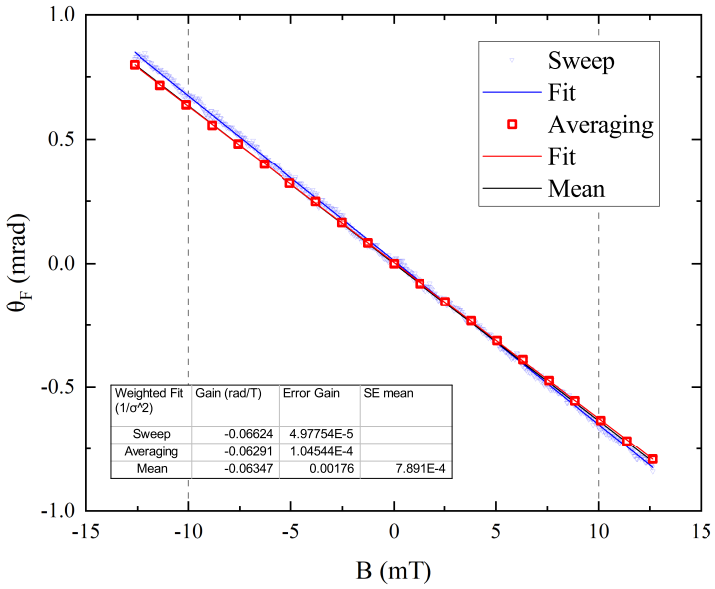

Figure 5.1: The measured Faraday rotation θ_F induced in 0.5 mm TGG for different values of the magnetic field B using both the Sweeping method (Blue triangles) and Averaging method (Red squares). The red solid line represents an unconstrained weighted linear fit while the blue line is an unconstrained fit of equation 3.2. The mean of the response is shown in black. The vertical dashed lines are the maximum and minimum fields when the wire is in a U-turn as discussed in section 3.2.1.

Table 5.1: The derived Verdet constants, the total error of the measurement and the expected values.

Parameter	Measured	Expected
mean Verdet constant (rad/(T.m))	-125.5 ± 0.7	-130 down to -134 [19, 38]
corrected Verdet constant (rad/(T.m))	-134	-
Total error	3%	1.5%

The Faraday based current sensor concept discussed in 4.1.1 is constructed and a proof of principle using TGG is presented in figure 5.1. The methods discussed in 4.3.1 have been applied. In figure 5.1 it can be observed that the slope is negative. The measurement methods, in blue and red, differ slightly showing a repeatability problem. This is discussed in appendix F.3.1 and is expected to influence the gain to be 6% different. The mean gain (in black) is found to be $(-6.35 \pm 0.08) * 10^{-2}$ rad/T. A summary of the derived values can be found in table 5.1. The mean Verdet constant is evaluated using the mean thickness and is lower than literature values. The wavelength of 658 nm is higher than those in literature, i.e. 633 nm. As shortly discussed in section 4.2.2 the measured Verdet constant should be increased by roughly 7%. With correction it is comparable to the Verdet constant found in literature. The average total error in the experiment is roughly 3%, equivalent to a measurement resolution of ~ 20 μrad, which is twice the value discussed in section 4.1.1. Without any optimization this total error is already comparable to that of some hall sensors, but with a much higher bandwidth. In order to further improve this Faraday based current sensor different scenarios will be investigated. Fundamental error contributions and its scaling will be discussed in the next section.

5.1.1 Error Investigations

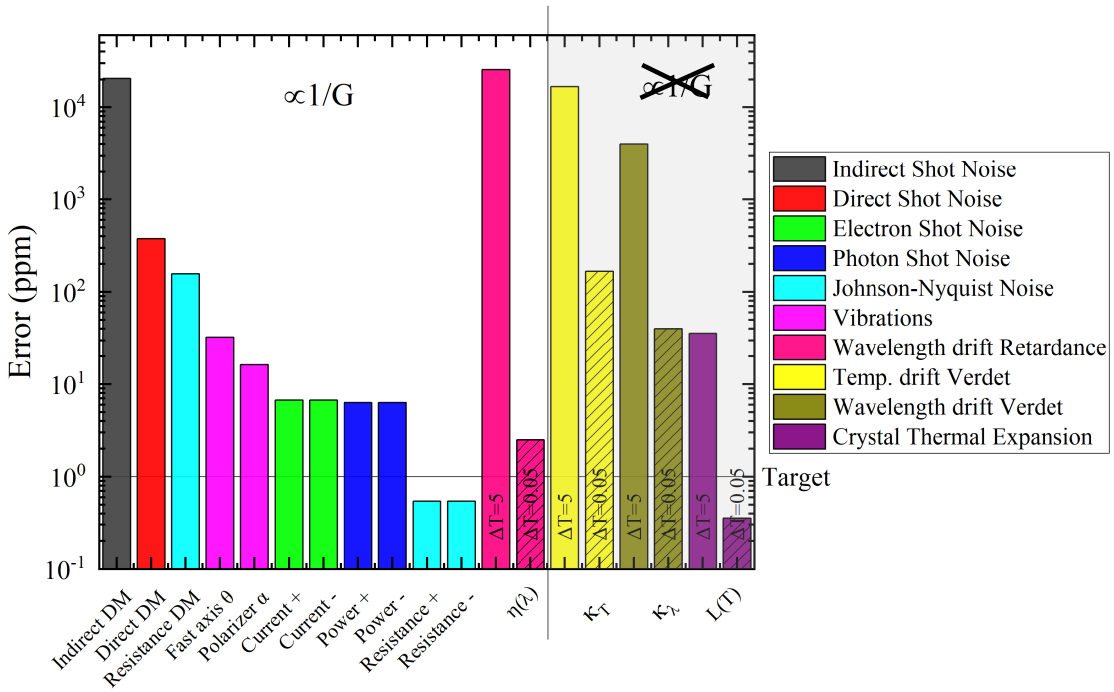

Figure 5.2: The contributions of different types of error sources for a 0.5 mm TGG crystal. On the right the open bar is for the $\Delta T = 5$ K scenario and the dashed bars is for the $\Delta T = 0.05$ K scenario. The total error for the $\Delta T = 5$ K is 66724 ppm and 20725 ppm for $\Delta T = 0.05$ K.

The results of the theoretical estimations of the errors are shown in figure 5.2. The evaluation of the different error terms is presented in appendix E.1. For each error that originates from a temperature drift two scenarios are considered. The first one is a fluctuation of $\Delta T = 5$ K. The second one is associated with a typical temperature bath with a temperature stability of $\Delta T = 0.05$ K. In both cases the wavelength drift is assumed to be the wavelength drift for a typical laser, HL6319G, 0.25 nm/K. The total error at $\Delta T = 5$ K and $\Delta T = 0.05$ K are roughly 6.7% and 2.1%, respectively. Comparing to the measured total error of 3% in section 5.1 both scenarios show the same order of magnitude total error. The large difference between the temperature scenarios originates from the large temperature drift of the Verdet constant that has been discussed in section 3.3.2. It is experimentally confirmed that $\kappa_T \approx 0.3\%/\text{K}$ (see in appendix G.1). This is comparable to literature values [34, 35, 37]. At $\Delta T = 5$ K and $\Delta T = 0.05$ K this means a contribution to the total error of $5\text{K} * 0.3\%/\text{K} = 1.5\%$ and $0.05\text{ K} * 0.3\%/\text{K} = 0.015\%$, respectively. Note that for the $\Delta T = 5$ K this 100 times larger error with the other temperature drifts make up the difference between the total error of both scenarios. Consequently, to achieve a low total error it is necessary to use a low temperature stability, $\Delta T = 0.05$ K, by e.g. using a temperature bath.

In both ΔT scenarios in figure 5.2 the shot noise at the DM output is one of the largest contributors. Specifically, the indirect DM shot noise, shown at the far left in dark grey, stemming from fluctuations in the two diode currents. Remember that $I_{DM} = I_+ - I_-$ is a subtraction but individual (stochastic) noise adds up. The largest Johnson-Nyquist noise, shown in cyan, comes from the resistance at the DM output. The contribution from the monitors is lower than the target. The vibrations in the fast axis of the phase retarder θ and polarizer angle α, shown in purple, introduce noise that is only 1 order of magnitude higher than the target of 1 ppm. As mentioned before, the Verdet constant has a significant temperature drift and a slightly smaller wavelength drift. Both cases have a much lower error than the indirect DM shot noise when a temperature bath is applied.

Please note that the above error estimation is not complete since the employed fast Fourier transform of measurement showed that low frequency error is dominated by 1/f noise (see in appendix G.2). Because the laser was not properly filtered out some 1/f noise of the laser still goes through [70]. Additionally the photodiode itself may contains some 1/f noise when active. Using high frequency (>> 1 MHz) modulation may remove this effect. How exactly these errors scale towards this 1 ppm is what will be treated in the next paragraph.

5.1.2 How to scale to 1 ppm error?

In section 3.2 it has been discussed that only portion of the error scales with the gain. The error sources in figure 5.2 are categorized by their scaling, i.e. those that diminish when the gain $G = \theta_F/B$ (rad/T) increases (left area) or those that are remain the same (right greyish area). The first type of error, termed sum square noise (SSN), can be scaled through to gain to eventually reach the target of 1 ppm. Their uncertainty is assumed to be 68% due to their stochastic behaviour. The exception is the wavelength drift of the retardance, which is assumed to have a 100% uncertainty. The second type of error, linear error (LE) (e.g. temperature drift), requires compensation schemes or selecting other materials with lower Verdet constant T-dependencies (κ_T) can help. This type of error is assumed to have 100% uncertainty as they have a direction. As a result they can compensate each other. This can lead to a reduced total LE, e.g. the crystal expands by a factor that is equal and opposite to the decrease in Verdet constant. A major difference between SSN and LE is that only the SSN contains a bandwidth dependency. For high bandwidths ($\gg$ 1 MHz) it is, therefore, necessary to lower the SSN significantly. It can be seen in figure 5.2 that only by using a temperature bath the LN to be much lower than the SSN. Therefore, in the next sections it is assumed that such a temperature bath is used and the focus will be to lower SSN by increasing the gain. A return is made when the SSN becomes comparable to the LN in section 5.3.2. With the method of increasing the gain through the Verdet constant being discussed in section 3.4, increasing the path length will be discussed in the next section.

5.2 Possibilities in enhancing the path length

There are two distinct ways to increase the path length. The first is increasing the crystal length, by means of a very long fiber. The second is to send the light through the crystal multiple times. In this case advantage of the non-reciprocal nature of the Faraday rotation is taken.

5.2.1 Increasing Crystal dimensions

In section 5.1 the path length is only 0.5 mm. From equation 3.2 it is clear that by increasing this path length the gain increases linearly. However, because the magnetic field scales with $\propto \frac{1}{r}$, discussed in section 3.2.1, the crystal length is limited to the proportions of the wire. That would allow a linear increase of the gain by roughly a factor ~ 10 up to ~ 5 mm. In figure 5.3 the result of increasing the path length by increasing the length of the crystal is shown for both TGG and glass. The averaging method of section 4.3.1 is applied. When the path length increases the gain, θ_F/B, increases linearly for both the TGG and glass. By comparing TGG and glass it can be seen that TGG has a much larger gain. The linear fits of equation 3.2 are forced through the origin as there is no Faraday effect present when the path length is zero. The Verdet constant is found to be 3.4 ± 0.5 rad/(T.m) for glass which is comparable with the literature values of roughly 4 rad/Tm [20, 53]. A fit of the TGG gives a Verdet constant of 132 ± 2 rad/(T.m), which is roughly 6% higher that the mean Verdet constant found in section 5.1. This may be explained by the measurement point at large path lengths being larger than expected. This deviation from the fit could indicate a non-linearity or other effects. Some of the possibilities for this non-linearity are speculated on in Appendix H.1. In general, the gain shows the expected linear increase with path length.

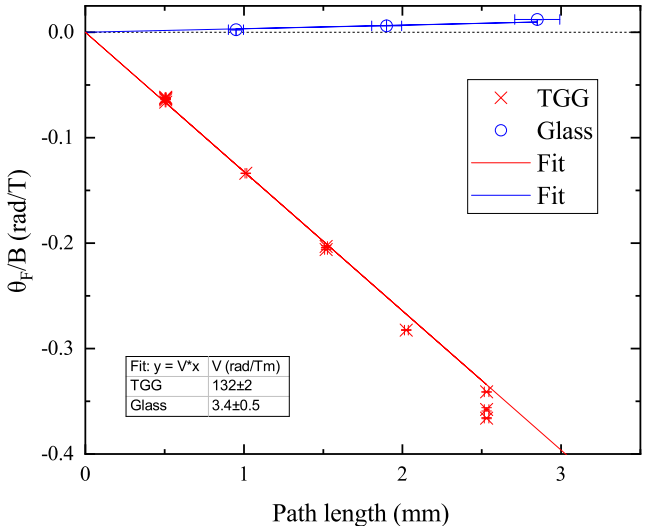

Figure 5.3: The gain $\frac{\theta_F}{B}$ (rad/T) of the setup for different path lengths obtained by placing an integer number of crystals against each other. The red crosses refer to 0.5 mm TGG crystals and the blue circles are for 0.95 mm glass plates. The solid lines represent a linear fits of equation 3.2. The fit parameters are shown in the table in the figure. The fitting is shortly discussed in Appendix H.

In this section it has been shown that increasing the path length is very effective to increase the gain of the current sensor. Furthermore, current sensors based on TGG will have a gain that is almost a factor 40 higher than that for to glass. A complication is that the magnetic field lines of current wire follow a circular path. For a proper Faraday effect the wave vector of the light must be parallel to the magnetic field. So, this vector must also follow this circular path. This

makes an increase of the crystal length for lengths larger than the $\sim$ 3 mm thick current wire impractical. Therefore, it will be limited to a factor increase of roughly 10. This means a crystal length of 5 mm. Consequently, this results in a total error of roughly 0.2%. This is comparable to the fiber-optics current sensor. To overcome the above restrictions a second method based on reflections is introduced in the next section.

5.3 Reflections

Reflections allow for the light to pass the same crystal multiple times resulting in a accumulation of the Faraday rotation. Because of the non-reciprocity it does not matter which direction the light travels through the crystal as long as its collinear with the magnetic field. However, at an interface not all light is reflected as parts are also transmitted or absorbed. Equally important is the induced relative phase shift on the polarization state of the light. This relative phase shift causes interference between the two orthogonal polarizations, i.e. s- and p-polarization, of the light. when a s- to p-polarization conversion occurs. Both these effect can reduce the potential gain significantly.

Next, the effects of reflections on the polarization state is discussed with the aid of the Fresnel equations. As an example, the reduction in potential gain will be shown using a simple experiment where the ideal gain of 2 will be reduced to $\sim$ 1.7 due to reflections at mirrors. The scaling of the gain in combination with this reduction will be extrapolated to a design with multiple reflections. Different cases are considered where this imperfection of the reflection might be negligible. Furthermore, the total error in each case is determined and compared. The lowest total error of 506 ppm is theorized. A further reduction to 280 ppm is conjectured when compensating for the non-linearity of the output.

5.3.1 Effects of using reflections on the Faraday rotation

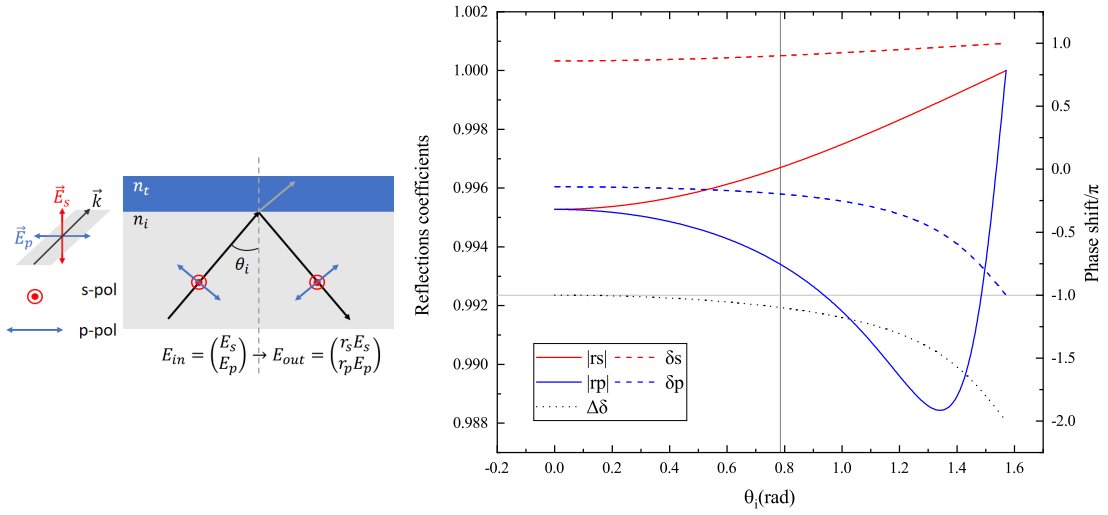

Figure 5.4: The left shows a schematic view of a reflection at the interface with the complex reflection coefficients. In the right graph the reflections coefficient, solid lines, and the phase shift, dashed lines, against the angle of incidence for a air ($n_i = 1$) to silver ($n_t = 0.049816 - 4.4764i$ [71, 72]) interface calculated using equations 5.1 and 5.2 are shown. Red represents s-polarized light and blue p-polarized light. The black dotted line is the relative phase shift between s- and p-polarization.

Because a reflection affects the polarization state of the light it can change the output of the Faraday based current sensor. Therefore, it is necessary to determine its influences on the polarization state and on its magnitude. Reflection at an interface is schematically shown for both s- and p-polarizations on the left in figure 5.4. The impact of a reflection on the electric field components, E_s and E_p, is denoted by the complex reflection coefficients r_s and r_p. Snell's law is used to calculate the angle of transmittance. Adding this result in Fresnel's equations for the complex reflection coefficients gives:

$$r_s = \frac{E_{out,s}}{E_{in,s}} = \frac{n_i \cos\theta_i - n_t\sqrt{1 - \frac{n_i^2 \sin^2\theta_i}{n_t^2}}}{n_i \cos\theta_i + n_t\sqrt{1 - \frac{n_i^2 \sin^2\theta_i}{n_t^2}}} \tag{5.1}$$

$$r_p = \frac{E_{out,p}}{E_{in,p}} = \frac{n_t \cos\theta_i - n_i\sqrt{1 - \frac{n_i^2 \sin^2\theta_i}{n_t^2}}}{n_t \cos\theta_i + n_i\sqrt{1 - \frac{n_i^2 \sin^2\theta_i}{n_t^2}}} \tag{5.2}$$

where n_i and n_t are the refractive indices of the initial and transmitted medium, respectively, and θ_i is the angle of incidence [73]. These complex reflection coefficients can be separated into two quantities: the reflection coefficient, $|r_{s,p}|$ (modulus), and the phase, $\delta_{s,p}$ (argument). The relative phase difference, ($\Delta\delta = \delta_p - \delta_s$), between s- and p-polarization cause a change in the polarization states in the reflected light, e.g. linear birefringence. In figure 5.4 the reflection coefficients and phase changes for a typical silver mirror used in an experiment to redirect light are shown on the right. The reflection coefficients are large over the entire range of θ_i meaning that the intensity of the reflected light remains large. This is attributed to the large imaginary part of the refractive index n_t, i.e. the absorption, of silver. Then, in approximation equation 5.1 and 5.2 approach unity. An ideal mirror would reflect the light backwards in a mirrored way. This occurs when the relative phase shift is π. It can be observed in figure 5.4 that only at small angles of incidence this ideal π-shift is reached. Deviations become significant when θ_i increases. These deviations can cause destructive interference between the s- and p-polarization when conversion between s- and p-polarized light occurs. Because the Faraday rotation causes such a conversion it will reduce the accumulated Faraday rotation, resulting in a reduced gain.

To illustrate the above a measurement is performed where light is forced to pass the crystal twice. Two different setups were made as shown in figures 5.5 and 5.6. Figure 5.5 shows the beam-splitter (BS) setup where the light always enters the TGG crystal from the same direction. Figure 5.6 shows the mirror setup (MS) where the light enters the TGG crystal from opposite directions. Both set-ups use multiple silver mirrors at roughly 45 degrees inducing a relative phase of roughly 0.3 rad as presented by the vertical gray line in figure 5.4.

Figure 5.7 shows the results of measurements using the sweep method as described in section 4.3. When the light entered the crystal twice (red and blue) the signal increased significantly compared to when it passed only once (black). It has been proven that the two passes and the non-reciprocal effect benefit the gain of the sensor. Because the MS setup had an odd number of mirrors the resulting rotation is flipped compared to an even number of mirrors. This effect is demonstrated by the obtained positive slope of the MS setup. As a reference, measurements were carried out with a single in the BS setup. After comparison, the enhancement of the gain of the BS setup and MS setup is found to be 1.669 ± 0.003 and 1.747 ± 0.003, respectively. Both increases in gain deviate from the ideal factor of 2. This indicates that the reflections do indeed cause a reduction in gain, this will be further investigated using Jones formalism.

The effect of the mirrors in the BS and MS-setup can be estimated by evaluating equations 5.1 and 5.2. Estimated values of the reflection coefficient and the relative phase shift are obtained by assuming deviations from an ideal mirror. The parameters $\Delta r = |r_s| - |r_p|$ and $\Delta\delta$ are shown near their respective elements in figures 5.5 and 5.6. The BS setup is represented using Jones Formalism by

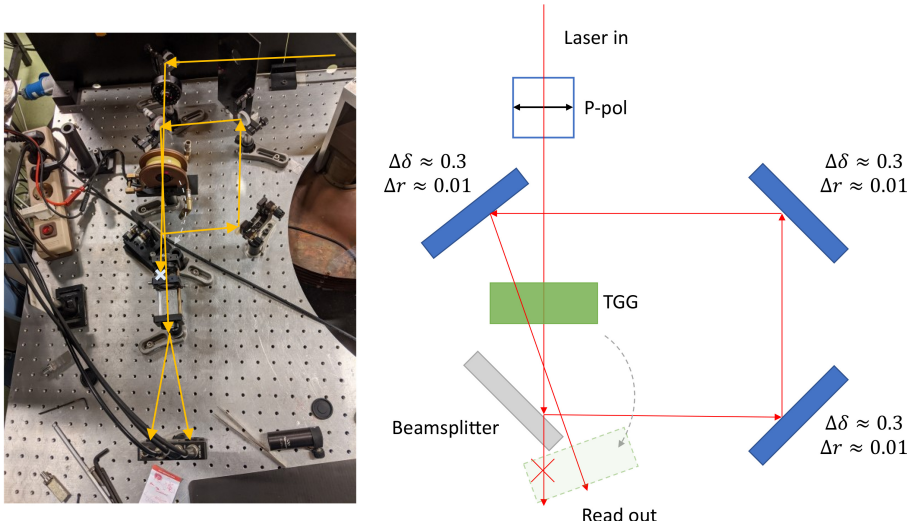

Figure 5.5: A photo of the setup (left) with a beamsplitter (BS) to transmit the light through the TGG twice from the same direction. On the right a schematic view of the setup. The dashed grey arrow indicates where the TGG with coil is placed to obtain a measurement of a single pass through the TGG. The values of the $\Delta\delta$ and Δr are for a reflection of a typical silver mirror at approximately 45 degrees (See figure 5.4).

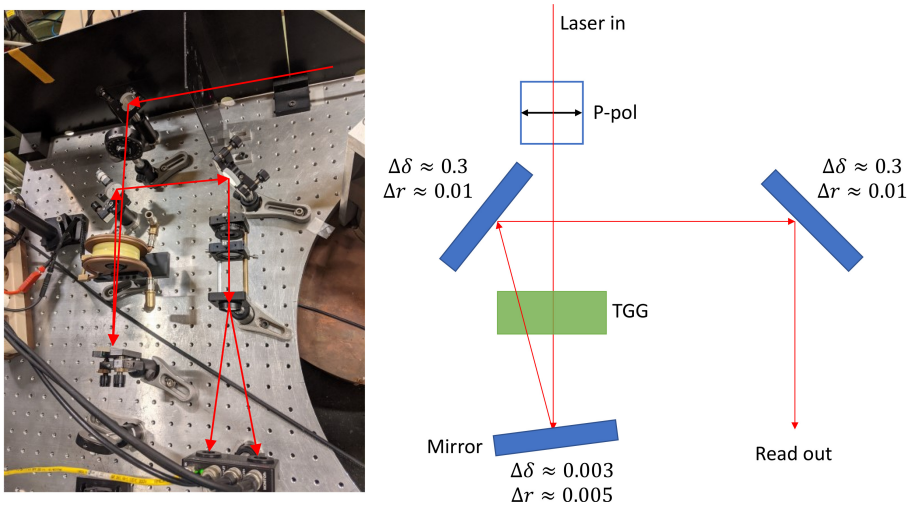

Figure 5.6: A photo of the setup (left) with a mirror (MS) to reflect the light towards the TGG in the opposite direction. On the right a schematic view of the setup. The values of the $\Delta\delta$ and Δr are for a reflection of a typical silver mirror at approximately 0 (bottom) and 45 degrees (top x2) (See figure 5.4).

$$E_{out} = FR_4R_3R_2R_1FE_{in}, \tag{5.3}$$

where $R_2 \approx R_3 \approx R_4$ represent the reflection matrices of the mirrors and R_1 represents the reflection matrix for the beamsplitter. Typically, the latter has a difference in reflectance between s- and p-polarized light of 20%. The MS setup can be represented using

$$E_{out} = R_3R_2FR_{1,M}FE_{in}, \tag{5.4}$$

where $R_{1,M}$ is the reflection matrix for the small angle mirror and $R_2 \approx R_3$ represent the matrices

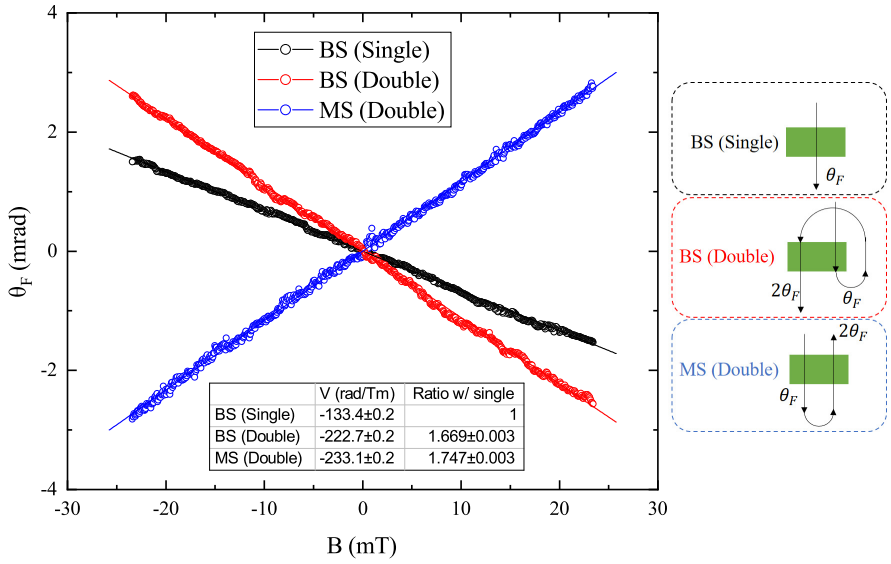

Figure 5.7: The Faraday rotation θ_F versus the magnetic field B applied in a 0.5 mm TGG crystal. In black the beamsplitter setup (BS) of figure 5.5 when the light passes the TGG only once. In red the BS setup where the light passes the crystal twice from the same direction. In blue the mirror setup (MS) of figure 5.6 where the light passes the crystal twice from opposite directions. The open circles represent measurement data. The solid line are the linear fits used to determine the Verdet constants as listed in the table as inset. In the table the ratio with the BS single pass is also shown.

Table 5.2: The relative gain increases for the MS and BS setups.

	BS	MS
Measurement	1.669 ± 0.003	1.747 ± 0.003
Calculated	1.72	1.69

for the mirrors after the second Faraday rotation. By applying equations 5.3 and 5.4 the expected increase in gain is calculated. Results are shown in table 5.2. The calculated value are close to the experimental values. The differences can be explained by the mirrors not reflecting the light at exactly 45 degrees. Consequently, the relative phase difference in figure 5.4 to changes by roughly 0.02 rad per degree. This can change the factor for the BS setup from 1.72 to 1.66, i.e. an uncertainty of 3%. The effects of the mirrors is discussed in appendix I.1.

It has been show that using two passes through the crystal increases the gain by a factor ~ 1.7. This number deviates from the ideal number 2 due to non-ideal reflections that influence the polarization state. The next question is how the reducing factor propagates in the case of multiple reflections. Li et al. have investigated this effect for up to 6 reflections [74]. A significant effect on the output was found. They found that the decrease in intensity scales almost linearly with the number of reflection. The decreasing reflection coefficients r_s and r_p lowered the sensitivity. Bush et al. found an identical issue when investigating the effect of linear birefringence in the path itself [75]. Ning et al. have used the critical angle to overcome the linear birefringence for more than 10 reflections when using glass [76]. However, deviation from this critical angle will introduce new error sources [77]. Although the effect of the imperfect reflections has been investigated in the past it is still unclear where the limits lie concerning the number of reflection and whether this can be adapted for different materials.

5.3.2 Multiple reflections to increase the gain

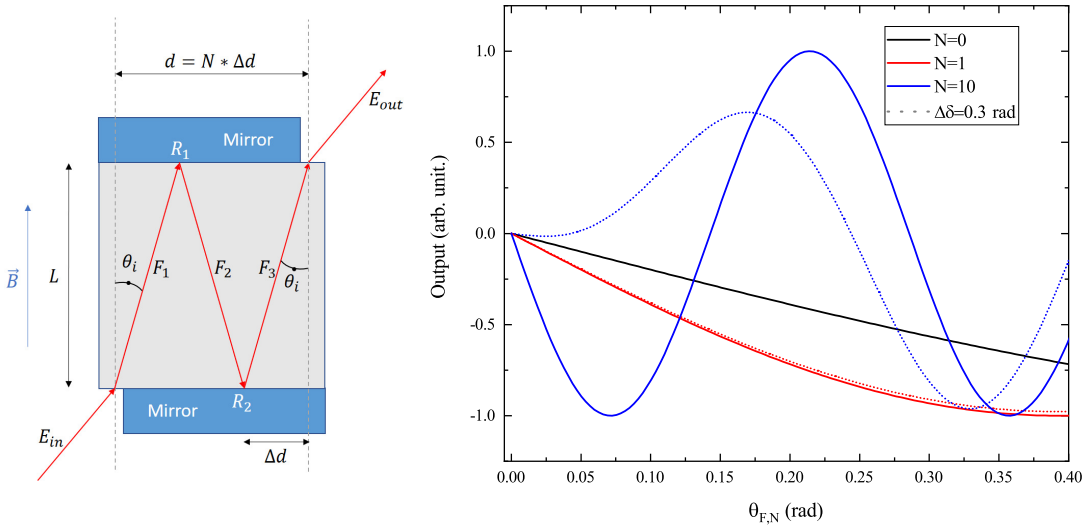

Figure 5.8: On the left the design using multiple reflection is schematically shown. The light enters the crystal of width d and length L. It experiences a Faraday rotation due to the magnetic field, B, represented by the Jones matrix F_1. Then the light reflects from a highly reflective mirror represented by matrix R_1. It experiences an addition Faraday rotation represented by matrix F_2 before reflecting again represented by matrix R_2. Finally it experiences the last Faraday rotation represented by matrix F_3. The number of reflections can be calculated by $N \approx \frac{d}{\Delta d} = \frac{d}{L \tan(\theta_i)}$. On the right the output of the sensor versus the Faraday rotation per reflections for various numbers of reflections is shown. In black no reflections are used. In red one reflection is used and in blue 10 reflections are present. The dotted lines represent the cases when each reflections adds a relative phase shift $\Delta\delta$ of 0.3 rad.

In figure 5.8 a simple design is shown where two reflections ($N = 2$) occur from two mirror. In this way three times the path length is obtained within the same crystal. If the losses by coupling in and out of the crystal are neglected the electric field exiting the crystal is given by

$$E_{out} = F_3(\theta_{F,N}) R_2 F_2(-\theta_{F,N}) R_1 F_1(\theta_{F,N}) E_{in}, \tag{5.5}$$

where F_i is the Jones matrix for the ith Faraday rotation, $\theta_{F,N}$ is the Faraday rotation per reflection (N) and R_i is the Jones matrix for the ith reflection. In this equation it can be seen that subsequent Faraday rotation alter in sign. This means an accumulation only occurs if a mirror reflects the light back with a flipped rotation, e.g. a relative phase shift of π is required. A simplification of equation 5.5 is achieved by assuming the Faraday rotation to be always positive for every reflection. The only disadvantage of this assumption is that after the light passes a phase retarder the direction of the rotation will become either positive or negative depending on whether N is odd or even. Then, equation 5.5 can be expanded for N reflection to

$$E_{out} = F(\theta_{F,N})(RF(\theta_{F,N}))^N E_{in}. \tag{5.6}$$

Calculated results are shown in figure 5.9 for using different numbers of reflections. Ideally for a single reflection (red solid line) the output is increased by a factor 2 at lower $\theta_{F,N}$. For 10 reflections (blue solid line) the output increases by a factor up to 10. Also, note the sinusoidal behaviour of the output. This becomes apparent at large number of reflections and already at lower $\theta_{F,N}$. This effect is caused by the accumulation of the Faraday rotation with each subsequent reflection. The influence of a typical silver mirror with a relative phase difference of $\Delta\delta = 0.3$ rad

at 45 degrees incidence is depicted by the dotted lines in figure 5.9. For this, a single reflection reduces the output by roughly 3 to 5%. Furthermore, in the case of 10 reflections this effect brings the output to nearly zero at small Faraday rotations per reflection.

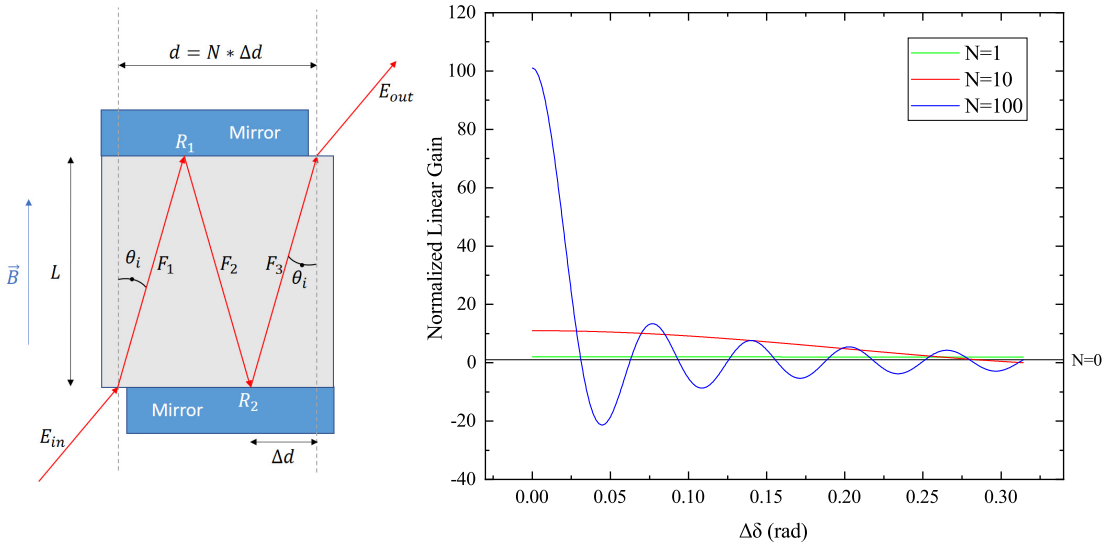

Figure 5.9: The design using multiple reflection as in figure 5.8 on the left. On the right the normalized linear gain $G_{refl}(N, \Delta\delta)/G_{refl}(0, \Delta\delta)$ against the relative phase shift $\Delta\delta$ shown for different number of reflections. The black line is attributed to the case of no reflections. The green line represent 1 reflection and red is associated with 10. The blue line is for 100 reflections.

The effect of the relative phase shift on the gain of the sensor can be estimated by combining equation 5.6 and equation 4.4 and evaluating a first order Taylor expansion with $\theta_{F,N} << 1$. Neglecting the influence of the reflection coefficients the gain can now be approximated as

$$G_{refl}(N, \Delta\delta) \approx 2\frac{\sin((N+1)\Delta\delta/2)}{\sin(\Delta\delta/2)}\cos(N\Delta\delta/2) \tag{5.7}$$

where $\Delta\delta$ is the relative phase shift and N is the number of reflections. In figure 5.9 the effect of small relative phase shift on the normalized linear gain can be observed for several number of reflections. For a single reflection the relative phase shift has little to no effect on the gain. However, for 10 reflections a decrease is noticeable when the relative phase shift increases. It even reduces to zero at ~ 0.28 rad. This also appears in figure 5.8 for small Faraday rotations. Further increasing the number of reflections to $N = 100$ invokes a very rapid decrease for very small relative phase shifts. An oscillatory behaviour appears with multiple point of zero gain. Therefore, to keep a large gain it is therefore necessary to reduce the relative phase shift when the applied number of reflections increases.

The maximum allowed relative phase shift to keep the gain at 95% of the ideal gain is shown in table 5.3. It shows that each order of magnitude increase in the number of reflections also decreases the required relative phase shift by an order of magnitude. To make 100 reflections feasible a reflection interface must be found that has a relative phase shift below 5 mrad. Additionally, a the reflection coefficient near unity is required to reduce optical losses. For a high reflective (HR) coating such as silver this might be achieved for θ_i up to 4 degrees. This is discussed in appendix I.3. For a total internal reflection (TIR) situation this is only feasible by using a refractive index difference smaller than 0.3% in the case of TGG ($n = 1.965$ [78]) or by using the critical angle where the relative phase shift is exactly zero. This is shown in appendix I.4. Therefore, it can

Table 5.3: The relative phase shift $\Delta\delta$ that causes a reduction of the gain to 95% of the ideal gain for different number of reflections.

N	$\Delta\delta$ (rad)
1	0.45
10	0.054
100	0.0055
1000	0.00055

be possible to obtain a gain increase of factor $\sim$ 100 by using reflections with these types of coatings. A case with 1000 reflections is not considered because the required relative phase shift is practically impossible to reach, yet. For instance, the TIR case would require a $\Delta n = 0.05\%$ and angle of incidence above 89 degrees. It should be noted that equation 5.6 does not take into account the drop in the magnetic field, and consequently in the Faraday rotation, when the light moves further away from the current wire. This effect is briefly discussed in appendix I.2. It could potentially reduce the gain by a factor 2. In the next section a full error investigation is executed again, but now with the addition of errors from the refractive index and the angle of incidence in case of these types of coatings. This is done to determine the cases that scale the best and can be used in the current sensor.

Consequences for the Current Sensor

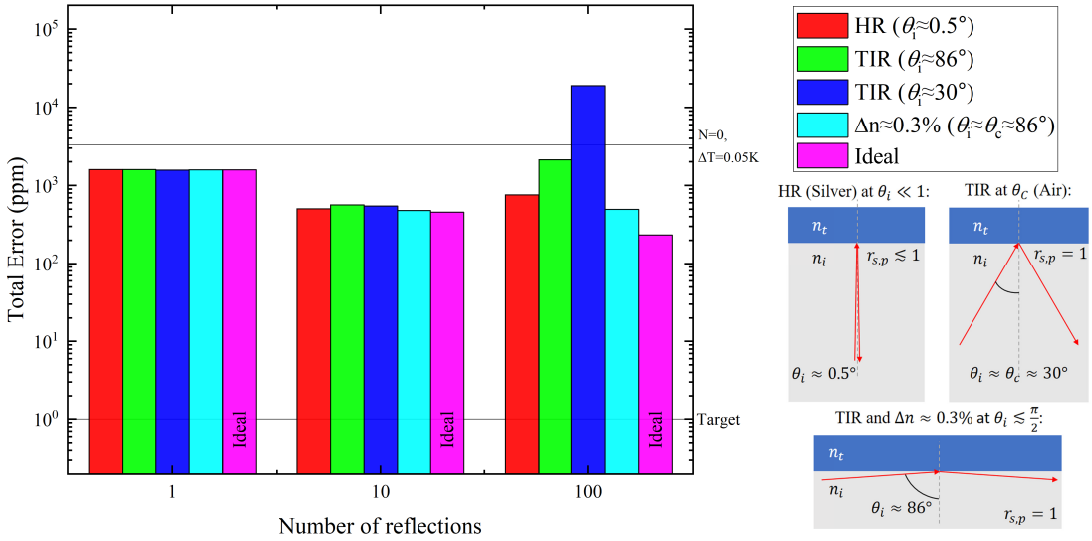

Figure 5.10: The total error for different number of reflections in a 5 mm TGG crystal. In red the High reflectance case (HR) with $\theta_i \ll 1$. In green the case of total internal reflection (TIR) case when $\theta_i \lesssim \frac{\pi}{2}$. In blue the TIR case when θ_i is near the critical angle. In cyan the TIR case when both layers have a refractive indices difference of 0.3% and $\theta_i \lesssim \frac{\pi}{2}$. In magenta the ideal case if no additional error sources are introduced and no optical loss is present. The temperature variation is 0.05 K. The top solid line in the graph represents the total error if no reflections $N = 0$ are used. The bottom solid line is the target of 1 ppm.

In order to investigate the scaling effects of the number of reflections several designs are considered. Each case is shown on the right of figure 5.10. The first one has a high reflective (HR) interface where the light reflects from a silver coating. Silver is chosen for its small real part and high imaginary part of the refractive index. This causes a high reflectance and embodies a lower

relative phase shift. This is discussed in appendix I.3. The second case is about total internal reflection (TIR) at the TGG to Air interface. There when a large angle of incidence is used. The third case is identical to the second one but now θ_i is close to the critical angle of TIR. This is equivalent to the design used by Yi et al. [79]. Both cases exhibit relative small relative phase shifts as shown in appendix I.4. The final case concerns an imaginary coating with a refractive index that differs only by 0.3% from TGG. It is equivalent to optical fibers where the relative phase shift are small (See appendix I.4).

In figure 5.10 the total error is presented for the different reflection cases. This consists of error source previously taken into account augmented with fluctuation in the refractive indices and the angle of incidence. For all these cases addition of a single reflection lowers the total error by roughly 50%. Changing to 10 reflections the above cases differentiate. The HR case (red) and the case with small Δn (cyan) have the lowest total error of roughly 500 ppm. Going from 10 reflection to 100 reflections all cases show an increase in the total error. The large increase for the case near critical angle (blue) is caused by the large first order derivative of the relative phase shift near the critical angle [77]. The increase for TIR ($\theta_i \lessapprox \frac{\pi}{2}$) (green) originates from the relative phase shift, $\Delta\delta \approx 0.12$ rad. This is much larger than the required 5 mrad as shown in table 5.3. This illustrates the issue with high relative phase shift. The increase in the HR case (red) is attributed to the reflection coefficients of ~ 0.992. For 100 reflections this gives a further reduction of the transmission to 45% [74]. However, even the best case Δn (cyan) is still a factor 3 apart from the ideal (magenta). This is partially due to the absorption reducing the intensity to $\sim 47\%$ causing a factor $1/\sqrt{0.47} \approx 1.5$ increase in the error. The main effect can be explained by the maximum Faraday rotation surpassing 0.4 rad crossing over into the non-linear regime of equation 4.4 which has been shortly discussed in section 4.1.1. The consequences of this non-linearity will be discussed next.

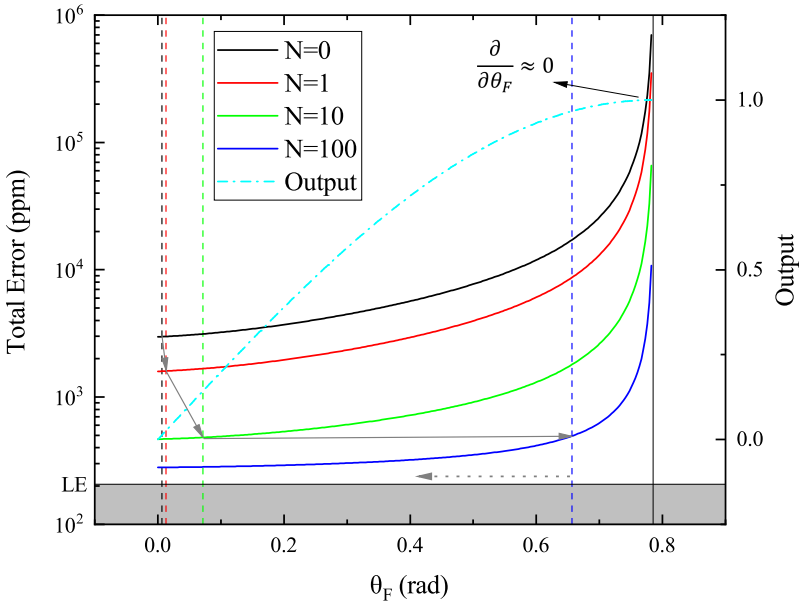

Figure 5.11: The total error versus the total accumulated Faraday rotation for different number of reflections. The dashed dotted line refers to the output of the current sensor (described by equation 4.4). The dashed lines represent the maximum Faraday rotation. The solid grey arrows indicate the path traced when going from 0 to 100 reflections. The grey area below 200 ppm is the LE dominated regime.

In figure 5.11 the total error versus the Faraday rotation is shown for different number of

reflections. For all of the error increases significantly when the Faraday rotation of $\pi/4$ rad is approached. This is caused by the output (dashed dotted line) for which the first order derivative is nearly zero at $\pi/4$ rad. At a low number of reflections this is not an issue because the maximum rotation (dashed vertical lines) does not reach this problematic region. The solid grey arrows indicate the movement of the maximum Faraday rotation when the number of reflections is increased, i.e. moving from $N = 0 \rightarrow N = 1 \rightarrow N = 10 \rightarrow N = 100$. Changing from $N = 10$ to 100 the grey arrow is nearly horizontal as the total error does not change. For $N = 100$ the maximum Faraday rotation is 0.6565 rad. This is too close to $\pi/4 \approx 0.79$ rad. Therefore, the increase in error deteriorate the enhancement due to the larger path length. By employing multiple outputs or a feedback scheme large maximum Faraday rotation can compensated for. They can reduce the effective maximum Faraday rotation (dashed grey arrow) towards a total error improved by a factor ~ 6.

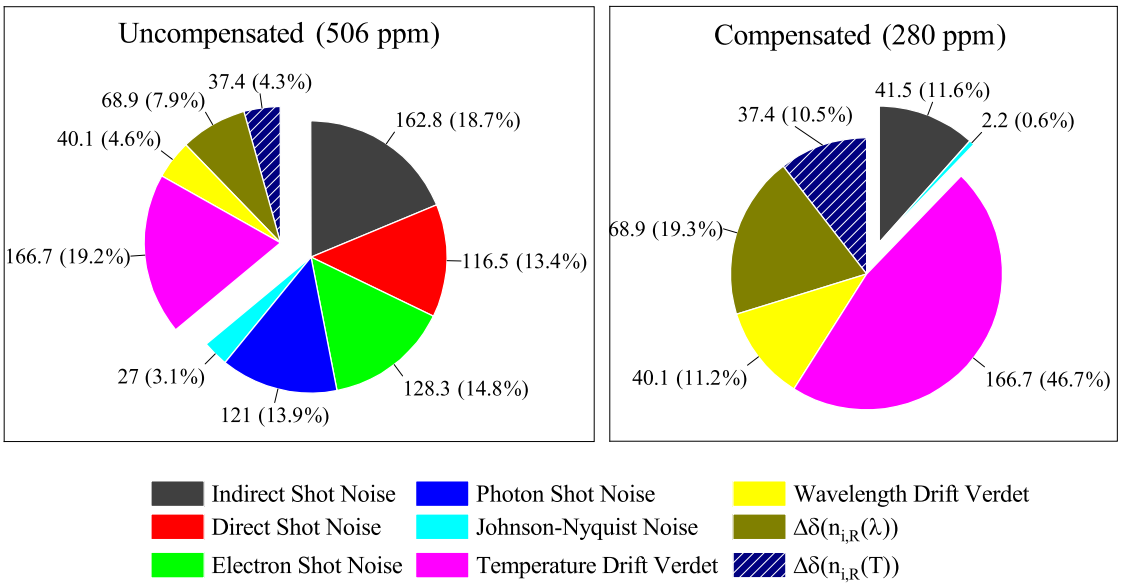

Figure 5.12: The error in ppm and percentage of the total in case of $\Delta n \approx 0.3\%$ and N=100. On the left the uncompensated case with $\theta_{F,max} = 0.6565$ rad. O the right and the compensated case with $\theta_{F,max} = 0$ rad. The exploded part on the left is linear error (LE) the rest is sum square noise (SSN). On the right the SSN is exploded compared to the LE. Any effect below 1 ppm or 1% has been removed for clarity. The dashed slice in the $\Delta n \approx 0.3\%$ case has a negative direction compared to the other LEs. The total error has been calculated and is placed at the top, the linear error is linearly added while the SSN is added as the root sum of squares.

Consider setting the maximum Faraday rotation when using 100 reflections to be either 0.6565 rad or 0 rad. Figure 5.12 shows the comparison between these maximum Faraday rotations for the case of small Δn. On the left the maximum Faraday rotation is not compensated. i.e. $\theta_{F,max} = 0.6565$ rad. In this case the sum square noise (SSN) (non-exploded) is higher than the linear error (LE) (exploded). On the other hand, when the maximum Faraday rotation is compensated back to zero the SSN (exploded part) is now much lower than the LE (non-exploded). Furthermore, the total error has decreased from 506 ppm to 280 ppm. Because the LE remains equal (238 ppm) this lower error comes from the decrease in SSN of 268 ppm to 42 ppm when changing from uncompensated to compensated, respectively. The error that lowers significantly are the photon (blue) and electron (red) shot noise in the monitor outputs and the direct (red) shot noise in the DM output. The indirect shot noise (dark grey) reduces by a factor 4 but does

not disappear. Equivalently, the Johnson-Nyquist noise (cyan) of the DM output is reduces from 27 to 2 ppm. This effect, where the contribution of the monitors is reduce when the output is reduced to zero, is typical of an optical bridge (see section 4.1.1). Thus, using a compensation technique reduces the SSN by a factor of ~ 6 and consequently reduces the total error by a factor ~ 2.

As a note, the drift of the refractive index becomes significant at $N = 100$. It has an effect on the relative phase shift, $\Delta\delta(n_{i,R}(T)$ and $\Delta\delta(n_{i,R}(\lambda)$. The contribution of the drift in the refractive index is 32 ppm. This can be reduced significantly by optimizing the angle of incidence towards a regime where the first derivative of the relative phase shift is zero. Error contributions from changes in the reflection coefficients caused by drift in the refractive index are found to be negligible. Likewise, vibrations of the angle of incidence is not significant.

At the start of this chapter the error has been found to be $\sim 3\%$ for a TGG based Faraday current sensor. Two major contributions to the total error have been identified; errors that scale with the gain (SSN) and errors that do not scale with the gain (LE). In methods with temperature stability the LE can be reduced to 200 ppm. This made it a minor contribution to the total error. The remaining SSN can be reduced by increasing the crystal size. This results in a a linear increase of the gain of the current sensor and reduces the error to $\sim 0.2\%$. A further increase in the gain has been observed by using reflections. A theoretical estimation showed that the error can potentially go down to 280 ppm with 100 reflections. This can only be achieved if the output of the current sensor is kept in its linear regime. A compensation scheme to achieve this will be presented in the next chapter. In addition, considerations for higher bandwidths are presented.

Chapter 6

Further Improvements

In the previous chapter it was found that the total error is constituted by 42 ppm SSN and 238 ppm LN. By maintaining the maximum Faraday rotation at zero allows for significant reduction of the error. This chapter will discuss how to achieve this with a feedback system. It properties and consequences for the current sensor are shortly discussed. This chapter will also elaborate on theoretical possibilities that further lower the error at high bandwidths by tuning the wavelength and the laser power. Finally, the Faraday based current sensor is compared to typical Fluxgates for different bandwidth.

6.1 Compensation schemes

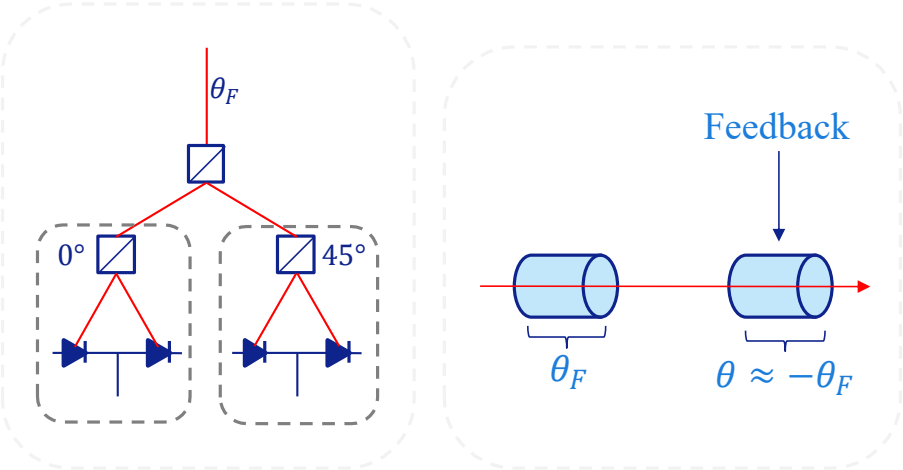

Figure 6.1: Two possible designs used to measure polarization rotation much larger than $\pi/4$ rad. On the left a setup uses two outputs that to are rotated 45 degrees relative to each other. On the right the first crystal causes the Faraday rotation θ_F. The second crystal reverts the polarization rotation to zero by means of a feedback mechanism.

Two concepts that can solve the issue with large Faraday rotations are shown in figure 6.1. On the left a design by Gerber et al. where a beamsplitter is used to create two outputs that are rotated by 45° relative to each other [11]. When an output reaches the rotation of 45 degrees the other output is used. This allows one to avoid the peaking error (See appendix D.1.1). This concept can help to reduce the SSN to roughly 90 ppm. The design on the right in figure 6.1 may achieve an even further reduction of the SSN to 42 ppm. It is similar to the work of Beltran et al. who used a second Faraday crystal driven by a coil to reduce the Faraday rotation back to zero

using a feedback system [80]. The current used to generate the feedback rotation is proportional to the current to be measured. Despite the reduction of the SSN to 42 ppm the LE of 238 ppm remains.

A major advantage of the feedback mechanism of Beltran et al. is that it the two crystals can be combined into one crystal. This gives the same temperature dependencies which reduces the LE. A possible way of implementing this technique with one crystal is shown in figure 6.2. On the left a design using HR at a small angle is shown and on the right a design using TIR at large angle of incidence is shown. In both cases two loops are wound around the crystal. The primary current, I_P, generates an magnetic field B_P while the feedback current, I_f, generates a opposite magnetic field, B_f. Both fields interact with the light passing through the crystal resulting in a Faraday rotation of

$$\theta_{tot} = a(T)B_P + b(T)B_f, \tag{6.1}$$

where $a(T) = V_p(T)L_p(T)$ and $b(T) = V_f(T)L_f(T)$ are the temperature dependent gain given by equation 3.2 concerning the primary and feedback loops. Because the interaction occurs in the same crystal it can be assumed that $a(T) = b(T)$. This reduces equation 6.1 to $\theta_{tot} = a(T)(B_P + B_f)$. Now, tuning θ_{out} to zero by tuning the feedback current to give $B_f = -B_P$ the gain $a(T)$ falls out of the equation. Hence, the temperature dependence of the gain becomes irrelevant. This requires a fast feedback system with a bandwidth much higher than is required of the current sensor. If such a system could be made the temperature effect could be entirely eliminated. Some other effects that may aid in reducing the effect of the temperature drift are discussed in the outlook.

In the rest of this chapter it is assumed that the above approach works perfectly and the only relevant error is the SSN of 42 ppm. While not entire correct the following methods may allow for an easier way to reach a low error instead of using complicated designs to implement a large number of reflections. Besides, for a Faraday based current sensor with a desired bandwidth beyond 1 MHz these methods can help significantly as the SSN eventually becomes larger than the LE.

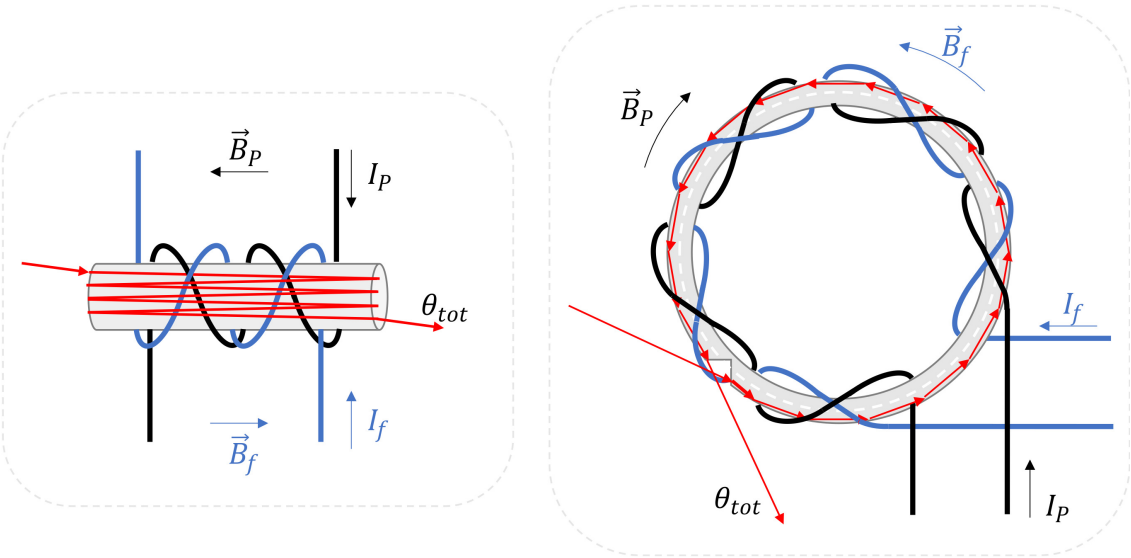

Figure 6.2: A schematic overview of using a feedback current wire to generate an opposite field in the same crystal. On the left a HR design with small angle of incidence and on the right a TIR design with large angle of incidence.

Table 6.1: The Verdet Constant, $\mathcal{V}$, and figure of merits, $\frac{\mathcal{V}}{\mu}$, of TGG and the Responsivity, $R(\lambda)$, of typical photodiodes for different wavelengths. The maximum path length, L, is calculated from the linear absorption coefficient, μ, where the optimum is twice this length discussed in Appendix E.3. The maximum Faraday Rotation, θ_F, is determined for 10 mT. Values taken from [38] and Thorlabs [81].

λ (nm)	$\mathcal{V}$ (rad/Tm)	$\frac{\mathcal{V}}{\mu}$ (rad/T)	$R(\lambda)$ (A/W)	Max. L, $\frac{2}{\mu}$ (m)	Max. θ_F (rad)
532	190	47.5	0.34	0.5	0.475
633	130	86.7	0.42	1.34	0.867
1064	40	266.7	0.74	13.34	2.67

6.2 Wavelength and Power Considerations

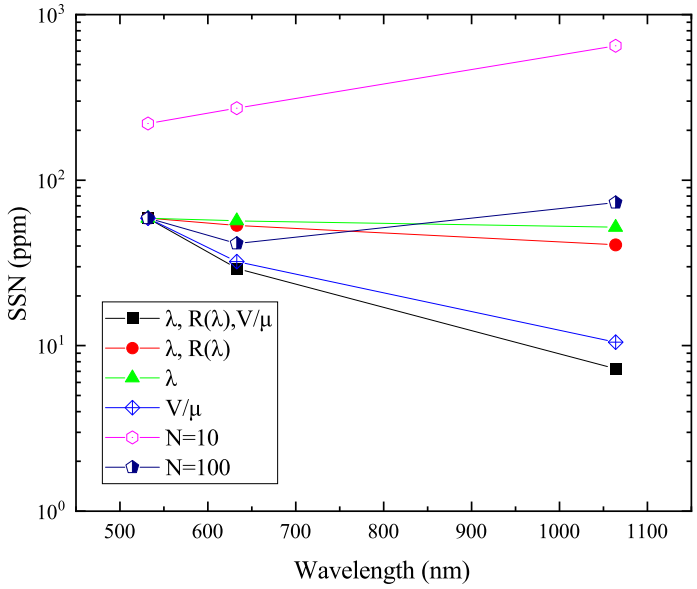

Figure 6.3: The ideal and non-ideal sum square noise (SSN) for different wavelengths when using a 5 mm TGG crystal. The black squares represents the sum of all effects. The red circles when only the changing wavelength and responsivity is taken into account. The green triangle only considers the change in wavelength and the blue diamond only considers the change in the figure of merits. The magenta hexagon and navy pentagon is when the path length is limited to 10 reflection or 100 reflection in a 5 mm crystal, respectively.

In chapter 5.1.2 it was discussed that a material with large FOM is desired. On the other hand, in chapter 5.2 it was found that large path lengths are difficult to achieve or even limited. This means that the path length in case of significant absorption can not always be reached. Therefore, higher Verdet constant might be preferred. One of the parameter that has a prominent influence on this selection is the wavelength as discussed in section 3.3.2. Additionally, the wavelength has an effect on the selection of the photodiode and the measurement resolution.

In figure 6.3 the theoretical effect of both the ideal and non-ideal effect of changing the wavelength on different parameters is shown for TGG. The values of the parameters are found in table 6.1 for wavelengths for which TGG is transparent and literature value are available. The

combined effect (black) of changing the wavelength, responsivity and figure of merits (FOM) can decrease the SSN by almost an entire order of magnitude when using large wavelengths. The variation of the FOM (blue) contributes the most to the decrease in the SSN. The wavelength (green triangles) slightly lowers the SSN. This is caused by the larger number of photons per energy unit at higher wavelengths which decreases the shot noise. However, if the responsivity is not changed the quantum efficiency of the conversion of photons to electrons reduces with increasing wavelength. When taking into account a change in responsivity for typical Si (FD11A) and InGaAs (FGA10) photodiodes from Thorlabs [81] the effect of changing the wavelength (red) has a slightly higher effect.

Remarkably when the path length is limited 10 reflections (magenta hexagons) the SSN increases with the wavelength. For this case, the decrease of the Verdet Constant dominates and this reduces the signal. The 100 reflections case (navy pentagon) is slightly different as it has a minimum SSN at 633 nm. The path length is long enough for the decrease in absorption to overcome the decrease in Verdet constant. For the 1064 nm case, however, the path length is not long enough.

In summary the choice of the wavelength depends on the path length of the final design. If it is much smaller than the maximum path length the Verdet constant is the most important parameter. When it is close to the maximum path length the FOM becomes the dominant parameter. In case of 100 reflections the optimum for TGG is at a wavelength of 633 nm. This means that the SSN will remain at 42 ppm.

Similarly to arguments such as absorption and transmission it is possible to also increase the total power of the laser. The relative shot noise decreases when the laser power increase due to larger number of photons and electrons. This is briefly discussed is appendix E.1.1. The relative Johnson-Nyquist noise also reduces at higher powers. This is discussed in appendix E.2.1. So the SSN scales with $\propto \frac{1}{\sqrt{P}}$. But increasing the laser power is limited. Typical photodiodes saturate at 20 mW. At higher power the photodiode will respond non-linearly [82]. Detecting higher powers is possible but the responsivity of these photodiodes drop drastically [83]. Additionally, heat can build up quicker. This increases the temperature instability of the current sensor. For powers > 1 W instabilities such as depolarization occur [84]. Melting may take place at, e.g. the silver coating of the HR design due to its high absorption. Concluding, a reductiong of the SSN can be achieved by moving from 1 mW to 20 mW. This gives an new SSN of $\frac{\sqrt{1\text{ mW}}}{\sqrt{20\text{ mW}}} * 42$ ppm ≈ 9 ppm. It is close to the value of 5 ppm found by Gerber et al [11]. This SSN is only an order of magnitude apart from the desired 1 ppm. How this compares to the presently used current sensor, i.e. the Fluxgate, will be discussed next.

6.3 Faraday based current sensor versus Fluxgates

The total error of typical Fluxgates can go down to 0.1 ppm [1, 85]. Fluxgates, however, have a limited bandwidth. For instance, one of the best commercially available Fluxgates, XPCS series from Prodrive, has a bandwidth limit of 800 kHz [86]. Similarly the Fluxgate from LEM, the IT 200-S ULTRASTAB, has a bandwidth limit of 500 kHz [87]. The effect of the bandwidth on the total error of the Fluxgate and the Faraday current sensor is compared in figure 6.4. The black curve represents the ideally compensated Faraday current sensor. It has total error that is roughly twice that of the XPCS series (blue) but is roughly an order of magnitude lower than the IT 200S ULTRASTAB (red). However, when the LE is not perfectly filtered out (green) the total error is 2 orders of magnitude higher than the Fluxgates at low bandwidths. Only at bandwidths above 1 GHz is the contribution of the LE minor. Concluding, The Faraday based current sensor, therefore, performs worse than the Fluxgates at low bandwidths (< 1 MHz) but works where Fluxgates cannot be applied at roughly twice the total error of the best Fluxgate at high bandwidth (~ 1 GHz).

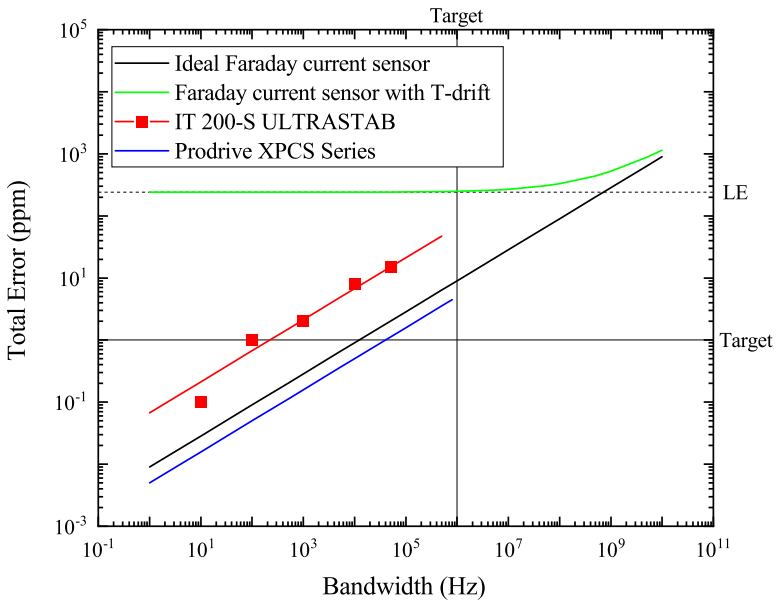

Figure 6.4: The total error in ppm against the bandwidth of the sensor. In black the case of a ideally compensated Faraday current sensor, e.g. SSN. In green a Faraday current sensor where the LE (Temperature drift) is still present. In red the total error of the Fluxgate IT 200-S ULTRASTAB from LEM and in blue the total error of XPCS series Fluxgate of Prodrive. The total errors are assumed to be white, e.g. the slope is a 1/2.

Chapter 7

Conclusions and Outlook

7.1 Conclusion

In chapter 3.2 the concept of a Faraday based current sensor has been introduced. The magnetic field gain, Verdet constant and path length were determined to be the main factors to reduce the total error. In chapter 3 different materials with varying Verdet constants were discussed. TGG has been found to be one of the optimal materials for measuring small currents. In chapter 4 the measurement technique has been discussed. The total error was estimated to be 1.5%. This was verified in chapter 5.1 to be twice the expected value, e.g. 3%. However, an issue with repeatability in the experimental methods was found. The main error contributions were estimated to be the shot noise and the temperature drift of the Verdet constant. In section 5.1.2 it has been argued that a temperature bath is required to lower the total error. This led to a theoretical shot noise limit of 2%. The gain is enhanced by increasing the crystal length up to a factor of ~ 10. This gave a total error of 0.2%. Further increases were obtained by using reflections. In experiments a verified gain increase of factor ~ 1.7 was obtained. Theoretically it has been derived that with 100 reflection the total error can be lowered to 280 ppm. This total error is mainly limited by the presence of a temperature drift of 238 ppm. In chapter 6 a compensation loop is proposed which avoids the non-linearity and can remove the temperature drift. Furthermore, the optimal wavelength to be used for TGG was determined to be 633 nm. The above combined with an increase in the laser power gives a total error to 9 ppm under ideal circumstances. This is only 1 order of magnitude away from the desired 1 ppm. In section 6.3 a comparison with Fluxgates showed that the Faraday based current sensor performs worse at low bandwidths (< 1 MHz). A big difference is that it works at at bandwidths where Fluxgates cannot be applied (> 1 MHz) and potentially up to several GHz.

7.2 Outlook

In section 6.1 a compensation scheme was discussed that could remove the temperature drift. However, this may be limited to only a factor ~ 10 or less and should be tested. Additionally, it is uncertain if 100 reflection within the bulk TGG is feasible. Equally important is the repeatability issue. For this the peripheral equipment should be changed to allow for both the current and the multiple outputs of the current sensor to be measured at the same time. This could be achieved by allowing accumulation and extracting the data at an equal time.

For the low and intermediary frequencies a GMI based current sensor shows promise [2, 4, 88]. With a error of ~ 10 pT$/\sqrt{\text{Hz}}$ the 1 ppm is reachable [3]. Additionally, the issue with the required ultra low error and high frequency carrier current may be solved by using the proposed FR current sensor to monitor this carrier current.

Table 7.1: Methods that might enhance the performance of the Faraday current sensor.

Method	Effective on:	factor enhancement	reference
Magnetic field modulation	temperature drift	~ 10	[89]
Thermal expansion in B-field	temperature drift	~ 10	[90]
High Circular Birefringence	gain	> 10	[75]
Cavity	gain	0-100	[22, 91, 92]
Flux Concentrator	gain	~ 40	[54, 79]
Calibration methods	systematic error	0-100	[93]
PICs	cost	$<< 2000$	[94]

A main disadvantage of the Faraday based current sensor is its cost. This originates from their large size and general high complexity. By transforming the Faraday based current sensor to a photonic integrated circuit (PIC) it may be possible to significantly reduce costs and sizes (< 1 mm). The TU/e research group Photonic Integration is presently capable of measuring polarization extinction of 30 dB. This means that the smallest measureable Faraday rotation is roughly 1 mrad giving a possible error of $\frac{1 \text{ mrad}}{10 \ \mu\text{rad}} * 9$ ppm $\approx 0.1\%$. This accuracy of the PICs is almost equivalent to the temperature drift of the Verdet constant of TGG. This makes them interesting replacements for current sensors in the 0.1% accuracy regime but with a significantly higher bandwidth. PICs also show potential to reach the 1 ppm required by ASML. Due to possibilities in geometries of PICs it might also allow for easier control of the relative phase shift incurred in reflections. This allows for greater possibilities in the designs for 100 reflections or even more. Furthermore, the error could be lowered by using averaging methods with a large number of the small sized PICs. To achieve this it is recommended to investigate materials with high Verdet constants in the NIR wavelength range as most PICs use InP which is transparent for NIR wavelengths. Alternatively PICs could be developed in the visible wavelength range. Their size is also an advantage in temperature control.

Some further possible improvements on the Faraday current sensor are summarized in table 7.1. They are shortly discussed in the Appendix J.

Bibliography

[1] Silvio Ziegler, Robert C. Woodward, Herbert Ho Ching Iu, and Lawrence J. Borle. Current sensing techniques: A review. *IEEE Sensors Journal*, 9(4):354–376, 2009. ISSN 1530437X. doi: 10.1109/JSEN.2009.2013914. 4, 42

[2] A. E. Mahdi, L. Panina, and D. Mapps. Some new horizons in magnetic sensing: High-Tc SQUIDs, GMR and GMI materials. *Sensors and Actuators, A: Physical*, 105(3):271–285, 2003. ISSN 09244247. doi: 10.1016/S0924-4247(03)00106-7. 4, 44

[3] Lehui Ding, Sébastien Saez, Christophe Dolabdjian, Luiz G.C. Melo, Arthur Yelon, and David Ménard. Equivalent magnetic noise limit of low-cost GMI magnetometer. *IEEE Sensors Journal*, 9(2):159–168, 2009. ISSN 1530437X. doi: 10.1109/JSEN.2008.2011067. 5, 44

[4] Christophe Dolabdjian and David Ménard. *Giant Magneto-Impedance (GMI) Magnetometers*, pages 103–126. Springer International Publishing, Cham, 2017. ISBN 978-3-319-34070-8. doi: 10.1007/978-3-319-34070-8_4. URL `https://doi.org/10.1007/978-3-319-34070-8_4`. 5, 44

[5] fibre optic current sensor abb. `https://new.abb.com/power-electronics/focs`. Accessed: 2021-01-25. 5

[6] Klaus Bohnert, Andreas Frank, Lin Yang, Xun Gu, and Georg M Müller. Polarimetric Fiber-Optic Current Sensor With Integrated-Optic Polarization Splitter. *Journal of Lightwave Technology*, 37(14):3672–3678, 2019. 5

[7] R Ulrich, S C Rashleigh, and W Eickhoff. Bending-induced birefringence in single-mode fibers I ,,,. 5(6):273–275, 1980. 5, 80

[8] Ricardo M. Silva, Hugo Martins, Ivo Nascimento, José M. Baptista, António Lobo Ribeiro, José L. Santos, Pedro Jorge, and Orlando Frazão. Optical Current Sensors for High Power Systems: A Review. *Applied Sciences*, 2(3):602–628, 2012. ISSN 2076-3417. doi: 10.3390/app2030602. 5

[9] A H Rose, M N Deeter, and G W Day. Submicroampere Per Root Hz, High Bandwidth Current Sensor Based on the Faraday Effect in Ga:YIG. pages 394–397, 1991. 5, 17, 82

[10] K. B. Rochford, A. H. Rose, M. N. Deeter, and G. W. Day. Faraday effect current sensor with improved sensitivity–bandwidth product. *Optics Letters*, 19(22):1903, 1994. ISSN 0146-9592. doi: 10.1364/ol.19.001903. 5

[11] Dominic Gerber and Juergen Biela. High-Dynamic and High-Precise Optical Current Measurement System Based on the Faraday Effect. *IEEE Transactions on Plasma Science*, 43 (10):3550–3554, 2015. ISSN 00933813. doi: 10.1109/TPS.2015.2437395. 5, 39, 42

[12] Weizhong Zhao. Magneto-optic properties and sensing performance of garnet YbBi:YIG. *Sensors and Actuators, A: Physical*, 89(3):250–254, 2001. ISSN 09244247. doi: 10.1016/S0924-4247(00)00560-4. 5, 17

[13] John S. McCloy and Brian Walsh. Sublattice magnetic relaxation in rare earth iron garnets. *IEEE Transactions on Magnetics*, 49(7):4253–4256, 2013. ISSN 00189464. doi: 10.1109/TMAG.2013.2238510. 5, 17

[14] Stefan Rietman and Jurgen Biela. Sensor design for a current measurement system with high bandwidth and high accuracy based on the faraday effect. *2019 21st European Conference on Power Electronics and Applications, EPE 2019 ECCE Europe*, pages 1–10, 2019. doi: 10.23919/EPE.2019.8915122. 5

[15] Atsufumi Hirohata, Keisuke Yamada, Yoshinobu Nakatani, Lucian Prejbeanu, Bernard Diény, Philipp Pirro, and Burkard Hillebrands. Review on spintronics: Principles and device applications. *Journal of Magnetism and Magnetic Materials*, 509(March), 2020. ISSN 03048853. doi: 10.1016/j.jmmm.2020.166711. 5

[16] M. Belal, Z. Song, Y. Jung, G. Brambilla, and T. P. Newson. Optical fiber microwire current sensor. *Optics Letters*, 35(18):3045, 2010. ISSN 0146-9592. doi: 10.1364/ol.35.003045. 5

[17] Herbert S. Bennett and Edward A. Stern. Faraday effect in solids. *Physical Review*, 137 (2A), 1965. ISSN 0031899X. doi: 10.1103/PhysRev.137.A448. 7

[18] J. M. D. Coey. *Magnetism and Magnetic Materials*. Cambridge University Press, 2010. doi: 10.1017/CBO9780511845000. 7, 57

[19] Zhe Chen, Lei Yang, Yin Hang, and Xiangyong Wang. Preparation and characterization of highly transparent Ce3+ doped terbium gallium garnet single crystal. *Optical Materials*, 47:39–43, 2015. ISSN 09253467. doi: 10.1016/j.optmat.2015.06.050. URL `http://dx.doi.org/10.1016/j.optmat.2015.06.050`. 8, 17, 23, 26

[20] Egberto Munin, J. A. Roversi, and A. Balbin Villaverde. Faraday effect and energy gap in optical materials. *Engineering optics*, 6(1):61–65, 1993. ISSN 09528911. 8, 28

[21] Aantal amperes en draaddikte van krachtstroomkabels. `https://www.bouwplaats-inrichting.nl/blog-en-nieuws/aantal-amperes-en-draaddikte-van-krachtstroomkabels`. Accessed: 2021-01-15. 10

[22] Chia-Yu Chang and Jow-Tsong Shy. Cavity-enhanced Faraday rotation measurement with auto-balanced photodetection. *Applied Optics*, 54(28):8526, 2015. ISSN 0003-6935. doi: 10.1364/ao.54.008526. 10, 16, 45, 80

[23] A. C.H. Rowe, I. Zhaksylykova, G. Dilasser, Y. Lassailly, and J. Peretti. Polarizers, optical bridges, and Sagnac interferometers for nanoradian polarization rotation measurements. *Review of Scientific Instruments*, 88(4), 2017. ISSN 10897623. doi: 10.1063/1.4980038. URL `http://dx.doi.org/10.1063/1.4980038`. 10, 20

[24] Jiaming Li, Le Luo, Jeff Carvell, Ruihua Cheng, Tianshu Lai, and Zixin Wang. Shot-noise-limited optical Faraday polarimetry with enhanced laser noise cancelling. *Journal of Applied Physics*, 115(10), 2014. ISSN 10897550. doi: 10.1063/1.4867743. 10, 21

[25] A. Mang, K. Reimann, and St Rübenacke. Band gaps, crystal-field splitting, spin-orbit coupling, and exciton binding energies in ZnO under hydrostatic pressure. *Solid State Communications*, 94(4):251–254, 1995. ISSN 00381098. doi: 10.1016/0038-1098(95)00054-2. 12

[26] A. L. Companion and M. A. Komarynsky. Crystal field splitting diagrams. *Journal of Chemical Education*, 41(5):257–262, 1964. ISSN 00219584. doi: 10.1021/ed041p257. 12

[27] H Ebert. Magneto-optical effects in transition metal systems. *Reports on Progress in Physics*, 59(12):1665–1735, dec 1996. doi: 10.1088/0034-4885/59/12/003. URL `https://doi.org/10.1088/0034-4885/59/12/003`. 12

[28] Overview electronic structures of periodic table. `https://ptable.com`. Accessed: 2021-01-15. 12

[29] Jiehui Yang, You Xu, and Maurice Guillot. The effect of the spin-orbit interaction strengths on the Faraday rotation in Pr-substituted yttrium iron garnet and in praseodymium trifluoride. *Journal of Physics Condensed Matter*, 11(16):3299–3314, 1999. ISSN 09538984. doi: 10.1088/0953-8984/11/16/011. 12, 17

[30] Fang Zhang, You Xu, Jiehui Yang, and Maurice Guillot. A theoretical study of the magnetic and magneto-optical properties of Nd-substituted yttrium iron garnets. *Journal of Physics Condensed Matter*, 12(32):7287–7294, 2000. ISSN 09538984. doi: 10.1088/0953-8984/12/32/312.

[31] Ryan Nakamoto, Bin Xu, Changsong Xu, Hu Xu, and L. Bellaiche. Properties of rare-earth iron garnets from first principles. *Physical Review B*, 95(2):1–8, 2017. ISSN 24699969. doi: 10.1103/PhysRevB.95.024434. 12, 17

[32] David Vojna, Ondřej Slezák, Antonio Lucianetti, and Tomáš Mocek. Verdet constant of magneto-active materials developed for high-power Faraday devices. *Applied Sciences (Switzerland)*, 9(15), 2019. ISSN 20763417. doi: 10.3390/app9153160. 13, 14, 15, 17, 18

[33] Aleksey V. Starobor, Dmitry S. Zheleznov, Oleg V. Palashov, and Efim A. Khazanov. Magnetoactive media for cryogenic Faraday isolators. *Journal of the Optical Society of America B*, 28(6):1409, 2011. ISSN 0740-3224. doi: 10.1364/josab.28.001409. 15

[34] Ondřej Slezák, Ryo Yasuhara, Antonio Lucianetti, and Tomáš Mocek. Temperature-wavelength dependence of terbium gallium garnet ceramics Verdet constant. *Optical Materials Express*, 6(11):3683, 2016. ISSN 2159-3930. doi: 10.1364/ome.6.003683. 16, 27

[35] Hassaan Majeed, Amrozia Shaheen, and Muhammad Sabieh Anwar. Complete Stokes polarimetry of magneto-optical Faraday effect in a terbium gallium garnet crystal at cryogenic temperatures. *Optics Express*, 21(21):25148, 2013. ISSN 1094-4087. doi: 10.1364/oe.21.025148. 16, 27, 70, 71

[36] Sarita Kumari and Sarbani Chakraborty. Study of different magneto-optic materials for current sensing applications. *Journal of Sensors and Sensor Systems*, 7(1):421–431, 2018. ISSN 2194878X. doi: 10.5194/jsss-7-421-2018. 17

[37] N P Barnes, L B Petway, Norman P Barnes, and Larry B Petway. Terbium Gallium Garnet. *October*, 9(10):1912–1915, 1992. 17, 27, 70, 71

[38] Ondrej Slezak, Ryo Yasuhara, Antonio Lucianetti, and Tomas Mocek. Wavelength dependence of magneto-optic properties of terbium gallium garnet ceramics. *Optics Express*, 23 (10):13641, 2015. ISSN 1094-4087. doi: 10.1364/oe.23.013641. 17, 18, 23, 26, 41

[39] Ilya L. Snetkov, Ryo Yasuhara, Aleksey V. Starobor, Evgeniy A. Mironov, and Oleg V. Palashov. Thermo-Optical and Magneto-Optical Characteristics of Terbium Scandium Aluminum Garnet Crystals. *IEEE Journal of Quantum Electronics*, 51(7), 2015. ISSN 00189197. doi: 10.1109/JQE.2015.2431611. 17

[40] Jiawei Dai, I. L. Snetkov, O. V. Palashov, Yubai Pan, Huamin Kou, and Jiang Li. Fabrication, microstructure and magneto-optical properties of Tb3Al5O12 transparent ceramics. *Optical Materials*, 62:205–210, 2016. ISSN 09253467. doi: 10.1016/j.optmat.2016.09.075. URL `http://dx.doi.org/10.1016/j.optmat.2016.09.075`. 17

[41] E. A. Mironov, O. V. Palashov, and D. N. Karimov. EuF2-based crystals as media for high-power mid-infrared Faraday isolators. *Scripta Materialia*, 162:54–57, 2019. ISSN 13596462. doi: 10.1016/j.scriptamat.2018.10.039. URL `https://doi.org/10.1016/j.scriptamat.2018.10.039`. 17, 18

[42] Amir A. Jalali, Evan Rogers, and Kevin Stevens. Characterization and extinction measurement of potassium terbium fluoride single crystal for high laser power applications. *Optics Letters*, 42(5):899, 2017. ISSN 0146-9592. doi: 10.1364/ol.42.000899. 17, 18

[43] David Vojna, Martin Duda, Ryo Yasuhara, Ondřej Slezák, Wolfgang Schlichting, Kevin Stevens, Hengjun Chen, Antonio Lucianetti, and Tomáš Mocek. Verdet constant of potassium terbium fluoride crystal as a function of wavelength and temperature. *Optics Letters*, 45(7):1683, 2020. ISSN 0146-9592. doi: 10.1364/ol.387911. 17, 18

[44] Valentyn Vasyliev, Encarnacion G. Villora, Masaru Nakamura, Yoshiyuki Sugahara, and Kiyoshi Shimamura. UV-visible faraday rotators based on rare-earth fluoride single crystals: LiREF4 (RE=Tb, Dy, Ho, Er and Yb), PrF3 and CeF 3. *Key Engineering Materials*, 582 (13):194–197, 2014. ISSN 16629795. doi: 10.4028/www.scientific.net/KEM.582.194. 17, 18

[45] Feiyun Guo, Qiyuan Li, Huaimin Zhang, Xiongsheng Yang, Zhen Tao, Xin Chen, and Jianzhong Chen. Czochralski growth, magnetic properties and faraday characteristics of CeAlO3 crystals. *Crystals*, 9(5), 2019. ISSN 20734352. doi: 10.3390/cryst9050245. 17, 18

[46] Younghun Hwang, Soo Seong Chung, and Youngho Um. Giant Faraday rotation in Cd1-xMnxTe (0 <; x < 0.82) crystals. *Physica Status Solidi (C) Current Topics in Solid State Physics*, 4(12):4453–4456, 2007. ISSN 18626351. doi: 10.1002/pssc.200777156. 17, 18

[47] Noboru Mikami, Chie Nagao, Takao Sawada, Hisamitsu Takahashi, Yoshinari Furukawa, and Eiya Aikawa. Temperature dependence of magnetic field sensors using (Cd 1-xMnx)Te and a light-emitting-diode light source. *Journal of Applied Physics*, 69(1):433–438, 1991. ISSN 00218979. doi: 10.1063/1.347680.

[48] Nils Kullendorff and Bertil Hök. Temperature independent Faraday rotation near the band gap in Cd1-xMnxTe. *Applied Physics Letters*, 46(11):1016–1018, 1985. ISSN 00036951. doi: 10.1063/1.95795. 17, 18

[49] Ondřej Slezák, Ryo Yasuhara, David Vojna, Hiroaki Furuse, Antonio Lucianetti, and Tomáš Mocek. Temperature-wavelength dependence of Verdet constant of Dy2O3 ceramics. *Optical Materials Express*, 9(7):2971, 2019. ISSN 2159-3930. doi: 10.1364/ome.9.002971. 17, 18

[50] Akio Ikesue, Yan Lin Aung, Shinji Makikawa, and Akira Yahagi. Total performance of magneto-optical ceramics with a Bixbyite structure. *Materials*, 12(3):1–13, 2019. ISSN 19961944. doi: 10.3390/ma12030421. 18

[51] Philippe Veber, Matias Velázquez, Grégory Gadret, Daniel Rytz, Mark Peltz, and Rodolphe Decourt. Flux growth at 1230 °c of cubic Tb2O3 single crystals and characterization of their optical and magnetic properties. *CrystEngComm*, 17(3):492–497, 2015. ISSN 14668033. doi: 10.1039/c4ce02006e. 17, 18

[52] Paul A Williams, A H Rose, G W Day, T E Milner, and M N Deeter. Temperature dependence of the Verdet constant in several diamagnetic glasses. *Applied Optics*, 30(10), 1991. 17, 18

[53] C.Z Tan and J Arndt. Wavelength dependence of the faraday effect in glassy sio2. *Journal of Physics and Chemistry of Solids*, 60(10):1689 – 1692, 1999. ISSN 0022-3697. doi: https://doi.org/10.1016/S0022-3697(99)00032-3. URL `http://www.sciencedirect.com/science/article/pii/S0022369799000323`. 17, 18, 28

[54] Merritt N Deeter. Sensor Based on Flux Concentrators. *Applied Optics*, pages 2–5, 1996. 17, 45, 82

[55] M. Deb, E. Popova, A. Fouchet, and N. Keller. Magneto-optical Faraday spectroscopy of completely bismuth-substituted Bi 3Fe 5O 12 garnet thin films. *Journal of Physics D: Applied Physics*, 45(45), 2012. ISSN 00223727. doi: 10.1088/0022-3727/45/45/455001. 17

[56] Shoujun Ding, Haotian Zhang, Renqin Dou, Wenpeng Liu, Dunlu Sun, and Qingli Zhang. Theoretical and experimental studies of electronic, optical and luminescent properties for Tb-based garnet materials. *Journal of Solid State Chemistry*, 263(March):123–130, 2018. ISSN 1095726X. doi: 10.1016/j.jssc.2018.04.028. URL `https://doi.org/10.1016/j.jssc.2018.04.028`. 17

[57] Mikio Geho, Takenori Sekijima, and Takashi Fujii. Growth of terbium aluminum garnet (Tb3Al5O 12; TAG) single crystals by the hybrid laser floating zone machine. *Journal of Crystal Growth*, 267(1-2):188–193, 2004. ISSN 00220248. doi: 10.1016/j.jcrysgro.2004.03.068.

[58] E. A. Mironov and O. V. Palashov. Faraday isolator based on TSAG crystal for high power lasers. *Optics Express*, 22(19):23226, 2014. ISSN 1094-4087. doi: 10.1364/oe.22.023226. 17

[59] Zhe Chen, Lei Yang, Yin Hang, and Xiangyong Wang. Faraday effect improvement by Dy3+-doping of terbium gallium garnet single crystal. *Journal of Solid State Chemistry*, 233:277–281, 2016. ISSN 1095726X. doi: 10.1016/j.jssc.2015.10.041. URL `http://dx.doi.org/10.1016/j.jssc.2015.10.041`. 17, 18

[60] Peiwen Man, Fengkai Ma, Tao Xie, Jingxin Ding, Anhua Wu, Liangbi Su, Huanying Li, and Guohao Ren. Magneto-optical property of terbium-lutetium-aluminum garnet crystals. *Optical Materials*, 66:207–210, 2017. ISSN 09253467. doi: 10.1016/j.optmat.2017.02.011. URL `http://dx.doi.org/10.1016/j.optmat.2017.02.011`. 17

[61] N. M. Ravindra, Preethi Ganapathy, and Jinsoo Choi. Energy gap-refractive index relations in semiconductors - An overview. *Infrared Physics and Technology*, 50(1):21–29, 2007. ISSN 13504495. doi: 10.1016/j.infrared.2006.04.001. 18

[62] Yi Huang, Huangchao Chen, Weilong Dong, Fufei Pang, Jianxiang Wen, Zhenyi Chen, and Tingyun Wang. Fabrication of europium-doped silica optical fiber with high Verdet constant. *Optics Express*, 24(16):18709, 2016. ISSN 1094-4087. doi: 10.1364/oe.24.018709. 18

[63] Pramod R. Watekar, Seongmin Ju, Su-Ah Kim, Seongmook Jeong, Youngwoong Kim, and Won-Taek Han. Development of a highly sensitive compact sized optical fiber current sensor. *Optics Express*, 18(16):17096, 2010. ISSN 1094-4087. doi: 10.1364/oe.18.017096. 18

[64] Tanja Graf, Claudia Felser, and Stuart S.P. Parkin. Simple rules for the understanding of Heusler compounds. *Progress in Solid State Chemistry*, 39(1):1–50, 2011. ISSN 00796786. doi: 10.1016/j.progsolidstchem.2011.02.001. URL `http://dx.doi.org/10.1016/j.progsolidstchem.2011.02.001`. 18

[65] Bo Fan, Mazhar E. Nasir, Luke H. Nicholls, Anatoly V. Zayats, and Viktor A. Podolskiy. Magneto-Optical Metamaterials: Nonreciprocal Transmission and Faraday Effect Enhancement. *Advanced Optical Materials*, 7(14):1–9, 2019. ISSN 21951071. doi: 10.1002/adom.201801420. 18

[66] Yong Zhao, Di Wu, Ri Qing Lv, and Jin Li. Magnetic Field Measurement Based on the Sagnac Interferometer With a Ferrofluid-Filled High-Birefringence Photonic Crystal Fiber. *IEEE Transactions on Instrumentation and Measurement*, 65(6):1503–1507, 2016. ISSN 00189456. doi: 10.1109/TIM.2016.2519767. 18

[67] Guido Frosio and René Dändliker. Reciprocal reflection interferometer for a fiber-optic Faraday current sensor. *Applied Optics*, 33(25):6111, 1994. ISSN 0003-6935. doi: 10.1364/ao.33.006111. 22

[68] Klaus Bohnert, Philippe Gabus, Jürgen Nehring, Hubert Brändle, and Martin Georg Brunzel. Fiber-optic current sensor for electrowinning of metals. *Journal of Lightwave Technology*, 25(11):3602–3609, 2007. ISSN 07338724. doi: 10.1109/JLT.2007.906795. 22

[69] F. Guattari, S. Chouvin, C. Molucon, and H. Lefevre. A simple optical technique to compensate for excess RIN in a fiber-optic gyroscope. *2014 DGON Inertial Sensors and Systems, ISS 2014 - Proceedings*, 2014. doi: 10.1109/InertialSensors.2014.7049411. 22

[70] O. Llopis, S. Azaizia, K. Saleh, A. Ali Slimane, and A. Fernandez. Photodiode 1/f noise and other types of less known baseband noises in optical telecommunications devices. *2013 22nd International Conference on Noise and Fluctuations, ICNF 2013*, pages 31–34, 2013. doi: 10.1109/ICNF.2013.6579014. 27, 71

[71] Overview refractive indices: Silver. `https://refractiveindex.info/?shelf=main&book=Ag&page=Babar`. Accessed: 2021-01-18. 29, 76

[72] Shaista Babar and J. H. Weaver. Optical constants of Cu, Ag, and Au revisited. *Applied Optics*, 54(3):477, 2015. ISSN 1559-128X. doi: 10.1364/ao.54.000477. 29, 76

[73] E. Hecht. *Optics*. Always learning. Pearson, 2016. ISBN 9781292096933. 30

[74] G. D. Li, R. A. Aspey, M. G. Kong, J. R. Gibson, and G. R. Jones. Elliptical polarization effects in a chromatically addressed faraday current sensor. *Measurement Science and Technology*, 10(1):25–30, 1999. ISSN 09570233. doi: 10.1088/0957-0233/10/1/008. 32, 36

[75] Simon P. Bush and David A. Jackson. Numerical investigation of the effects of birefringence and total internal reflection on Faraday effect current sensors. *Applied Optics*, 31(25):5366, 1992. ISSN 0003-6935. doi: 10.1364/ao.31.005366. 32, 45, 80

[76] Y. N. Ning, B. C. B. Chu, and D. A. Jackson. Miniature Faraday current sensor based on multiple critical angle reflections in a bulk-optic ring. *Optics Letters*, 16(24):1996, 1991. ISSN 0146-9592. doi: 10.1364/ol.16.001996. 32

[77] Benshun Yi, B. C.B. Chu, K. S. Chiang, and Henry S.H. Chung. New design of optical electric-current sensor for sensitivity improvement. *IEEE Transactions on Instrumentation and Measurement*, 49(2):418–423, 2000. ISSN 00189456. doi: 10.1109/19.843089. 32, 36

[78] U. Schlarb and B. Sugg. Refractive Index of Terbium Gallium Garnet. *Physica Status Solidi (B)*, 182(2):K91–K93, 1994. ISSN 15213951. doi: 10.1002/pssb.2221820238. 34

[79] B. Yi, B.C.B. Chu, and K.S. Chiang. Magneto-optical electric-current sensor with enhanced sensitivity. *Measurement Science and Technology*, 13(7), 2002. 36, 45, 82

[80] Hugo C. Beltran, Jorge L. Flores, José A. Ferrari, Guillermo García-Torales, and Javier Cabrera. Optical current sensor by self-compensating the Faraday effect. *Infrared Remote Sensing and Instrumentation XIX*, 8154(September 2011):815414, 2011. ISSN 0277786X. doi: 10.1117/12.894119. 40

[81] Photodiodes thorlabs. `https://www.thorlabs.com/newgrouppage9.cfm?objectgroup_id=285`, . Accessed: 2021-01-25. 41, 42

[82] Photodiodes lab facts. `https://www.thorlabs.com/images/TabImages/Photodetector_Lab.pdf`, . Accessed: 2021-01-25. 42

[83] Optical power meters. `https://www.thorlabs.com/newgrouppage9.cfm?objectgroup_id=3328`, . Accessed: 2021-01-25. 42

[84] Ryo Yasuhara, Ilya Snetkov, Alexey Starobor, Dmitry Zheleznov, Oleg Palashov, Efim Khazanov, Hoshiteru Nozawa, and Takagimi Yanagitani. Terbium gallium garnet ceramic Faraday rotator for high-power laser application. *Optics Letters*, 39(5):1145, 2014. ISSN 0146-9592. doi: 10.1364/ol.39.001145. 42

[85] Pavel Ripka. Electric current sensors: A review. *Measurement Science and Technology*, 21 (11), 2010. ISSN 13616501. doi: 10.1088/0957-0233/21/11/112001. 42

[86] XPCS Series Fluxgate Prodrive. `https://prodrive-technologies.com/products/power-conversion/power-components/xpcs-series-current-sensing/`. Accessed: 2021-02-18. 42

[87] IT 200s Ultrastab from LEM. `https://www.lem.com/en/it-200s-ultrastab`. Accessed: 2021-01-25. 42

[88] J L Van Mastrigt. Ultraprecise current sensing for sub-nanometer dynamic positioning in lithography tools. 2019. 44, 55

[89] César D. Perdante and José A. Ferrari. Faraday current sensor with temperature monitoring. *Applied Optics*, 44(32):6910–6912, 2005. ISSN 15394522. doi: 10.1364/AO.44.006910. 45, 79

[90] E. A. Mironov, A. V. Voitovich, and O. V. Palashov. Faraday isolator stably operating in a wide temperature range. *Laser Physics Letters*, 13(3), 2016. ISSN 1612202X. doi: 10.1088/1612-2011/13/3/035001. 45, 79

[91] Nan Di and Jianlin Zhao. Principle and applications of Faraday-Fabry-Perot cavity. *Optoelectronic Devices and Integration III*, 7847(November 2010):784712, 2010. ISSN 0277786X. doi: 10.1117/12.870422. 45, 80

[92] Hui Sun, Yaohua Lei, Shuangli Fan, Qiaolin Zhang, and Hong Guo. Cavity-enhanced room-temperature high sensitivity optical Faraday magnetometry. *Physics Letters, Section A: General, Atomic and Solid State Physics*, 381(3):129–135, 2017. ISSN 03759601. doi: 10.1016/j.physleta.2016.10.045. URL `http://dx.doi.org/10.1016/j.physleta.2016.10.045`. 45, 80

[93] Stefan Rietmann and Jurgen Biela. Error Induced by the Optical Path of a High Accuracy and High Bandwidth Optical Current Measurement System. *2020 22nd European Conference on Power Electronics and Applications, EPE 2020 ECCE Europe*, pages 1–11, 2020. doi: 10.23919/EPE20ECCEEurope43536.2020.9215673. 45, 82

[94] Dzmitry Dzibrou. *Building blocks for control of polarization in photonic integrated circuits.* Number 2014. 2014. ISBN 9789038636030. doi: 10.6100/IR772730. 45, 82

[95] Bert Koopmans. *Laser-Induced Magnetization Dynamics*, pages 256–323. Springer Berlin Heidelberg, Berlin, Heidelberg, 2003. ISBN 978-3-540-46097-8. doi: 10.1007/3-540-46097-7_8. URL `https://doi.org/10.1007/3-540-46097-7_8`. 57

[96] R Clark Jones. I . Description and Discussion of the Calculus. *Journal of the Optical Society of America*, 31(7):488–493, 1941. 58

[97] J. Zak, E. R. Moog, C. Liu, and S. D. Bader. Universal approach to magneto-optics. *Journal of Magnetism and Magnetic Materials*, 89(1-2):107–123, 1990. ISSN 03048853. doi: 10.1016/0304-8853(90)90713-Z. 59

[98] J.R. Taylor and S.L.L.J.R. Taylor. *Classical Mechanics.* G - Reference,Information and Interdisciplinary Subjects Series. University Science Books, 2005. ISBN 9781891389221. 63

[99] Georg M. Muller, Andreas Frank, Lin Yang, Xun Gu, and Klaus Bohnert. Temperature Compensation of Interferometric and Polarimetric Fiber-Optic Current Sensors with Spun Highly Birefringent Fiber. *Journal of Lightwave Technology*, 37(18):4507–4513, 2019. ISSN 15582213. doi: 10.1109/JLT.2019.2907803. 79

[100] H. Guerrero, R. Pérez Del Real, R. Fernández De Caleya, and G. Rosa. Magnetic field biasing in Faraday effect sensors. *Applied Physics Letters*, 74(24):3702–3704, 1999. ISSN 00036951. doi: 10.1063/1.123226. 80

[101] Zhengping P. Wang, Hongyu Wang, Haili Jiang, and Xiaoyu Liu. A magnetic field sensor based on orthoconjugate reflection used for current sensing. *Optics and Laser Technology*, 39(6):1231–1233, 2007. ISSN 00303992. doi: 10.1016/j.optlastec.2006.08.008. 80

[102] Matthieu Aerssens, Andrei Gusarov, Benoît Brichard, Vincent Massaut, Patrice Mégret, and Marc Wuilpart. Faraday effect based optical fiber current sensor for tokamaks. *ANIMMA 2011 - Proceedings: 2nd International Conference on Advancements in Nuclear Instrumentation, Measurement Methods and their Applications*, 2011. doi: 10.1109/ANIMMA.2011.6172868. 80

[103] V. Minier, D. Persegol, J. L. Lovato, and A. Kévorkian. Integrated Optical Current Sensor for High-Power Systems. *Optical Fiber Sensors*, We23, 1996. doi: 10.1364/ofs.1996.we23. 80

[104] L.M. Augustin. *Polarization handling in photonic integrated circuits*. Number 2008. 2008. ISBN 9789038618548. doi: 10.6100/IR634815. URL `http://alexandria.tue.nl/extra2/200810694.pdf`. 80

[105] Joseph H. Apfel. Phase retardance of periodic multilayer mirrors. *Applied Optics*, 21(4):733, 1982. ISSN 0003-6935. doi: 10.1364/ao.21.000733. 81

[106] R. R. Subkhangulov, R. V. Mikhaylovskiy, A. K. Zvezdin, V. V. Kruglyak, Th Rasing, and A. V. Kimel. Terahertz modulation of the Faraday rotation by laser pulses via the optical Kerr effect. *Nature Photonics*, 10(2):111–114, 2016. ISSN 17494893. doi: 10.1038/nphoton.2015.249. 81

[107] Mehmet C. Onbasli, Taichi Goto, Xueyin Sun, Nathalie Huynh, and C. A. Ross. Integration of bulk-quality thin film magneto-optical cerium-doped yttrium iron garnet on silicon nitride photonic substrates. *Optics Express*, 22(21):25183, 2014. ISSN 1094-4087. doi: 10.1364/oe.22.025183. 81

[108] P. Velha, V. Sorianello, M. V. Preite, G. De Angelis, T. Cassese, A. Bianchi, F. Testa, and M. Romagnoli. Wide-band polarization controller for Si photonic integrated circuits. *Optics Letters*, 41(24):5656, 2016. ISSN 0146-9592. doi: 10.1364/ol.41.005656. 81

[109] N. E. Fisher and D. A. Jackson. Vibration immunity and Ampere's circuital law for a near perfect triangular Faraday current sensor. *Measurement Science and Technology*, 7(8):1099–1102, 1996. ISSN 09570233. doi: 10.1088/0957-0233/7/8/002. 82

[110] César Daniel Perciante and José A. Ferrari. Magnetic crosstalk minimization in optical current sensors. *IEEE Transactions on Instrumentation and Measurement*, 57(10):2304–2308, 2008. ISSN 00189456. doi: 10.1109/TIM.2008.919913. 82

[111] Maria Gabriella Masi, Lorenzo Peretto, and Roberto Tinarelli. Design and performance analysis of a differential current sensor for power system applications. *IEEE Transactions on Instrumentation and Measurement*, 61(12):3207–3215, 2012. ISSN 00189456. doi: 10.1109/TIM.2012.2205513. 82

[112] Soheila Kharratian, Hakan Urey, and Mehmet C. Onbaşlı. RGB Magnetophotonic Crystals for High-contrast Magnetooptical Spatial Light Modulators. *Scientific Reports*, 9(1):1–12, 2019. ISSN 20452322. doi: 10.1038/s41598-018-37317-9. 82

Appendix A

Sensor Requirements ASML

In table A.1 the desired specification of a current sensor are given. The range is the minimum and maximum current that a sensor should be able to measure. The non-linearity is the maximum deviation of the output signal from its calibrated value. It is desired that the output is as linear as possible. The bandwidth is the maximum frequency of a signal that a sensor can measure accurately. The noise spectral density (NSD) refers to the random jitter on top of the output signal. The NSD is converted into a ppm values by multiplying it with the bandwidth and dividing it by the range of the current sensor, e.g. $(0.1\frac{\mu\text{A}}{\sqrt{\text{Hz}}} * \sqrt{1\text{MHz}})/(100\text{A}) = 1$ ppm. The gain, or sensitivity, is the slope between the output and the applied current, $G = output/input$. This gain can change in time and due to temperature fluctuations moving away from calibrated values. These give the requirements Gain time drift and Gain temperature drift. Equivalently the offset in the output can change in time and with temperature causing wrong interpretations of the output. The offset time drift and offset temperature drift must, therefore, also be small. The supply voltage of the current sensor will also contain fluctuations. To prevent these from influencing the output the current sensor has to be build to suppress these fluctuation. The ammount of suppression is defined using the Power Supply Rejection Ratio (PSRR). Random peaks in the frequency domain are called spurious signals. The final requirement that is not listed here is the shielding from surroundings. Conductors closeby may generate stray field and influence the output of the current sensor making differentiation between surroundings and the actual current difficult.

Table A.1: The requirements for a current sensor used in the wafer stage. Values are normalized to the range of the sensor. Adapted from [88].

Specification	Present	Desired
Range	$0 - 100$ A	$0 - 100$ A
Non-linearity	< 100 ppm	< 10 ppm
Bandwidth	200 kHz	≥ 1 MHz
Noise spectral density	$< 0.5\frac{\mu\text{A}}{\sqrt{\text{Hz}}}$	$< 0.1\frac{\mu\text{A}}{\sqrt{\text{Hz}}}$
Gain time drift	< 100 ppm/month	< 10 ppm/month
Gain temperature drift	< 2 ppm/K	< 0.5 ppm/K
Offset time drift	?	< 100 ppm/month
Offset temperature drift	?	< 2 ppm/K
PSRR	?	< -100 dBA/V
Spurious signal	?	1 single ray $< 2\mu\text{A}_{rms}$ and > 2 kHz

Appendix B

Theory

B.1 Dielectric Tensor

When an electromagnetic field interacts with a materials a polarization is induced. Neglecting nonlinear and nonlocal effect the response can be defined by the dielectric tensor, ε. For a cubic material the dielectric tensor is given by

$$\varepsilon = \begin{pmatrix} \varepsilon_{xx} & \varepsilon_{xy} & \varepsilon_{xz} \\ -\varepsilon_{xy} & \varepsilon_{yy} & \varepsilon_{yz} \\ -\varepsilon_{xz} & -\varepsilon_{yz} & \varepsilon_{zz} \end{pmatrix} \tag{B.1}$$

The dependency of the matrix elements on the magnetic field occurs through the induced magnetization, $M = \chi H$, where χ is the magnetic susceptibility. Additionally, the Onsager theorem adds a symmetry condition, e.g. $\varepsilon_{ij}(M) = \varepsilon_{ji}(-M)$. The consequence is that the diagonal elements are even and the off-diagonal are odd in magnetization. The diagonal elements are equal and independent on the magnetization if only first order effects in magnetization are considered, i.e. $\varepsilon_{xx} = \varepsilon_{yy} = \varepsilon_{zz}$. Therefore, by probing the off-diagonal elements can information on the magnetization be obtained. This probing can be obtained by diagonalizing equation B.1 by transforming to the cylindrical coordinates using

$$e_{\pm} = \frac{1}{\sqrt{2}}(\hat{x} \pm i\hat{y}) \tag{B.2}$$

$$e_z = \hat{z} \tag{B.3}$$

where the $+$ and $-$ represent the right and left circular sense, respectively. This gives the adapted dielectric tensor when assuming the magnetic field and light are parallel to the z-axis (e.g. $\varepsilon_{xz}, \varepsilon_{yz} = 0$) as:

$$\varepsilon' = \begin{pmatrix} \varepsilon_{xx} - i\varepsilon_{xy} & 0 & 0 \\ 0 & \varepsilon_{xx} + i\varepsilon_{xy} & 0 \\ 0 & 0 & \varepsilon_{xx} \end{pmatrix} \tag{B.4}$$

The dielectric constants for left- and right-circular polarized light are now given by

$$\varepsilon_{\pm} = \frac{1}{\sqrt{2}}(\varepsilon_{xx} \pm i\varepsilon_{xy}) \tag{B.5}$$

Assuming the relative permeability to be small the relation between the dielectric constant and the refractive index is

$$n_R = \sqrt{\varepsilon_+} \tag{B.6}$$

$$n_L = \sqrt{\varepsilon_-} \tag{B.7}$$

With this a connection has been made to equation 3.1. The difference between the dielectric constants, $\varepsilon_+ - \varepsilon_- \equiv \varepsilon_{+-} = i\varepsilon_{xy}$, for left- and right-circular polarized light determines how large the Verdet constant will be.

B.1.1 Microscopic Dielectric Tensor

The macroscopic dielectric tensor and the microscopic electronic structure within the independent electron approximation are related through [95]:

$$\varepsilon_{ij}(\omega) = \delta_{ij} + \frac{4e^2}{\pi\hbar m^2\omega^2}\sum_{gn}\int_{BZ} dk^3 \frac{\omega_{gn,\mathbf{k}}[f_{g,\mathbf{k}}(1-f_{n,\mathbf{k}})](|P^+_{gn}|^2 \pm_{ij} |P^-_{ng}|^2)}{\omega^2_{gn,\mathbf{k}} - \omega^2 - 2i\omega\Gamma_{gn,\mathbf{k}}}. \tag{B.8}$$

Where ij equals xx or $+-$, the operator $\pm_{ij}$ denotes $+(-)$ for $ij = xx(+-)$, and indexes g and n label Bloch states, which are indicated by their wave vector $\mathbf{k}$ and occupied by a fraction $f_{n,\mathbf{k}}$, (Equal to the Fermi-Dirac distribution). The integral is across the complete Brillouin zone, and the summations is over all bands. The energy $\hbar\omega_{gn,\mathbf{k}}$ corresponds to the difference between bands g and n at $\mathbf{k}$, and $\Gamma_{gn,\mathbf{k}}$ denoted the lifetime broadening of this transition. Only $\Delta\mathbf{k} = 0$ ('vertical') transitions have been taken into account, as consequence of the electric dipole approximation. The matrix element P is given by

$$P^{\pm}_{gn} = \langle\psi_{g,\mathbf{k}}|p_{\pm}|\psi_{n,\mathbf{k}}\rangle \tag{B.9}$$

that couples states via the momentum operator $p_{\pm} = -i\hbar(\nabla_x \pm i\nabla_y)$. It determines the probability of a transition between states to occur. If there is spin splitting in the energy bands the quantity $P^+_\uparrow$ will be different from $P^-_\uparrow$. This effect is proportional the Spin-Orbit coupling, e.g. $|P^+_\uparrow| - |P^-_\uparrow| \propto \lambda_{SO}$.

B.2 Spin-Orbit Coupling

See Coey [18] page 67, 91 and 104 for more information. The equivalent current loop of the motion of the nucleus in figure 3.4 is $I_n = Zev/2\pi r$, which creates a magnetic field $B_{so} = \mu_0 Zev/4\pi r^2$ at the center that the electron experiences. The interaction energy, $\varepsilon = -\mu_B B_{so}$, can be written approximately in terms of the Bohr magneton and the Bohr radius since $r \approx a_0/Z$ for an inner electron and $r = na_0$ for an outer electron, and $m_e vr \approx \hbar$. In the former case,

$$\varepsilon_{so} = -\frac{\mu_0\mu_B^2 Z^4}{2\pi a_0^3}. \tag{B.10}$$

Here the high dependence on the atomic number Z can be seen. This equation can be rewritten in a Hamiltionian for multiple electrons atoms in section 3.3, where the parameters above are hidden in the Spin-Orbit coupling constant Λ.

Appendix C

Jones Formalism

Jones Formalism or Jones Calculus is a mathematical method that grants a simple method of determining the influence of optical elements on the polarization of incident light [96]. It works by looking at the evolution of the amplitudes and the phase shifts of the electric field of the incident light. However, if the incident light is randomly, partially polarized or incoherent then Jones formalism fails to describe this properly and the more generalistic Mueller Calculus (Stokes parameters) must be used.

C.1 Jones Formalism

If an electromagnetic wave moves in the z-direction its electric field can be described by

$$\begin{pmatrix} E_x(t) \\ E_y(t) \end{pmatrix} = \begin{pmatrix} E_{0x}e^{i(kz-\omega t+\phi_x)} \\ E_{0y}e^{i(kz-\omega t+\phi_y)} \end{pmatrix} = \begin{pmatrix} E_{0x}e^{i\phi_x} \\ E_{0y}e^{i\phi_y} \end{pmatrix} e^{i(kz-\omega t)}, \tag{C.1}$$

where ω is the angular frequency of the light, k is the wavenumber, t is the time, $E_{0,x}$ and $E_{0,y}$ are the electric field amplitudes and ϕ_x and ϕ_y are the phase shifts. Jones formalism works by only evolving the amplitude and phase of the light, i.e. $e^{i(kz-\omega t)}$ can be neglected. The transformation occurs through the so-called Jones matrices. For istance, the Jones matrix for a arbitrary Faraday rotation, θ, without linear birefringence is given by

$$F \equiv J_{Rot} = \begin{pmatrix} \cos\theta & -\sin\theta \\ \sin\theta & \cos\theta \end{pmatrix}. \tag{C.2}$$

The intensity of the light can be calculated from the electric field as follows

$$J = EE^* \tag{C.3}$$

where the $*$ indicates the conjugate transpose.

C.1.1 Optical Elements

The Jones matrices for the different optical components that are used in this report are given here. A polarizer that has its major axis at an angle α:

$$P \equiv J_{Pol} = \begin{pmatrix} \cos^2\alpha & \cos\theta\sin\alpha \\ \cos\alpha\sin\alpha & \sin^2\alpha \end{pmatrix}. \tag{C.4}$$

The output of a polarizing beamsplitter can be modelled as a polarizer having its major axis either at 0 degrees or 90 degrees. A linear phase retarder with retardance η and fast axis at an angle of θ_f is described by

$$P_R(\eta,\theta_f) \equiv J_{PR} = e^{\frac{i\eta}{2}} \begin{pmatrix} \cos^2\theta_f + e^{i\eta}\sin^2\theta_f & (1-e^{i\eta})\cos\theta_f\sin\theta_f \\ (1-e^{i\eta})\cos\theta_f\sin\theta_f & \sin^2\theta_f + e^{i\eta}\cos^2\theta_f \end{pmatrix}. \tag{C.5}$$

A reflection from a surface with reflection coefficients $|r_p|$ and $|r_s|$ and phase shifts δ_p and δ_s for p- and s-polarizations is denoted by

$$R \equiv J_R = \begin{pmatrix} |r_p|e^{i\delta_p} & 0 \\ 0 & |r_s|e^{i\delta_s} \end{pmatrix}. \tag{C.6}$$

For a more general approach such as multilayer sytems the reader is referred to Zak et al [97].

Appendix D

Error scaling

D.1 Scaling Error

The Error scaling is calculated using equation 4.4 as follows

$$\frac{\sigma_{\theta_F}}{\theta_{F,max}} = \frac{\frac{\partial \theta_F}{\partial x}\sigma_x}{\theta_{F,max}} = \frac{\frac{1}{2}\frac{\partial \arcsin(x)}{\partial x}\sigma_x}{\theta_{F,max}} = \frac{\sigma_x}{2\sqrt{1-x^2}}\frac{1}{\theta_{F,max}}, \tag{D.1}$$

where $x = \frac{G_{mon}(\omega)}{G_{DM}(\omega)}\frac{V_{DM}}{V_+ + V_-}$ (or $x = \sin(2\theta_F)$) is the output obtained with equation 4.4, σ_{θ_F} is the measurement resolution in Faraday rotation, $\sigma_x \approx \sin(2 * 10\mu\text{rad}) \approx 2 * 10^{-5}$ is the measurement resolution in terms of output, and $\theta_{F,max}$ is the maximum Faraday rotation of the current sensor at maximum current. The error as a function of the maximum Faraday rotations, $\theta_{F,max}$, is shown in figure D.1. When focussing on the real scaling (black line) increasing the maximum Faraday rotation from 0 rad lowers the error significantly until the maximum Faraday rotation is roughly 0.4. After this the error starts increasing exponentially until blowing up to infinity at $\pi/4$ rad. Increasing the maximum Faraday rotation further lowers the error again until an optimum and it start increasing until blowing up at $3\pi/4$ rad. This pattern keeps repeating. Every $(2n+1)\pi/4$ rad, where n is an integer, the error goes to infinity. For a maximum Faraday rotation of roughly 11 rad the target of 1 ppm is reached, while ideally (blue dashed dotted line) this occurs at roughly 10 rad. For the current sensor the behaviour of the error in figure D.1 has one major consequences; for Faraday rotation close to an integer of $\pi/4$ rad the measured current would be highly inaccurate. In section 6.1 two concepts are discussed that can avoid this regime entirely.

D.1.1 Effect of multiple outputs

In figure 6.1 two concepts are shown that can aid in avoiding non-linear regimes. On the left large rotation are measured by moving from the output at 0 degrees to the output at 45 degrees when the Faraday rotation becomes larger than $\sim$ 22.5 degrees. This effect of this rotated output is shown in figure D.1 by the red dotted line between 2 and 3 rad in the grey area. In the grey area where the error of the 0 degree output goes to infinity the 45 degree rotated output instead has an almost ideal error figure. Consequently by swapping from the 0 degree output to the 45 degree output one avoids the near infinite error. In this grey area the maximum error is roughly two times higher than the ideal error. Similarly, on the right in figure 6.1 the Faraday rotation, θ_F, is reduced back to zero using a second crystal that rotated the polarization by, $-\theta_F$, using a feedback scheme. This effectively forces the output to remain in a linear regime, e.g. $\sin(2\theta_F) \approx 2\theta_F$, and the ideal case of figure D.1 is followed.

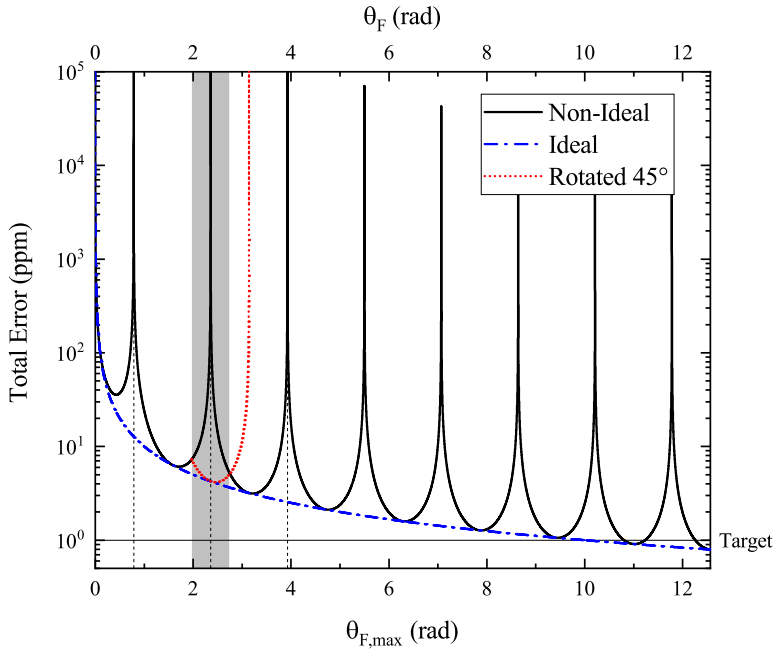

Figure D.1: The total error against the maximum Faraday rotation, $\theta_{F,max}$. The blue dashed dotted line is the ideal error scaling while the red solid line is the error scaling of equation D.1. The dashed vertical lines are the places where the maximum rotation is $(2n+1)\pi/4$, where $n = 0, 1, 2$. The target of 1 ppm is shown by the horizontal black line which crosses the error scaling at 10 rad and 11 rad for ideal and non-ideal, respectively. The red dotted line between 2 and 3 rad is if the output is rotated by 45 degrees. In the grey area the output used for readout is swapped from 0 degrees (non-ideal) to 45 degrees.

Appendix E

Error

E.1 Noise Terms

E.1.1 Shot Noise

Shot noise originates from the discrete nature of the electrons and photons. Measuring discreteness inherently involves uncertainty. It is a type of noise that can be modelled as a Poisson process. Its behaviour is equivalent to the experiment of tossing a coin, e.g. the larger the number of throws the smaller the relative noise. The electronic shot noise is given by

$$i_{shot} = \sqrt{2eI_{dc}\Delta f} \tag{E.1}$$

where e is the elementary electron charge, I_{dc} the DC current and Δf the bandwidth of the signal. For optical devices the photons also contribute with their discreteness:

$$P_{shot} = \sqrt{\frac{2hcP_{dc}\Delta f}{\lambda}} \tag{E.2}$$

where c is the speed of light in vacuum, h the plank constant, λ the wavelength of the light and P_{dc} the DC power. The effect on total error can be determined by dividing the noise, P_{shot}, by the signal, P_{dc}. It can immediately be seen that the relative noise scales as $\propto \frac{1}{\sqrt{P_{dc}}}$, e.g. decreasing for higher power. In analogy to the coin tossing experiment, the absolute number of photons that fluctuate increases but the relative noise decreases as the number of photons increases. So by increasing the wavelength the number of photons per energy unit increases lowering the noise. Shot noise can be seen as a White noise, which means it is a constant value in the frequency domain.

E.1.2 Johnson-Nyquist Noise

Johnson-Nyquist noise, also known as Thermal noise, is a type of noise that is present inside electronic conductors, e.g. resistors. The finite temperature of the resistor causes the electrons to move around with an thermal energy of $\langle H \rangle = k_B T$. This movement causes finite changes in the measured voltage over a resistor. The root mean square of this voltage fluctuation is given by

$$v_{rms} = \sqrt{4k_B T R \Delta f}. \tag{E.3}$$

This noise is a major component of the noise of an opamp. The relative noise can be described as $\propto v_{rms}/V_{signal}$. So by increasing the signal in voltage, e.g. increasing the laser power, one can lower the relative Johnson-Nyquist noise. For the photodiode electronic circuit with resistance R the higher this resistance the higher the gain: $V_{signal} \propto G(\omega) = R$. The effect of the resistance on the relative noise, therefore, scales as $\propto \frac{1}{\sqrt{R}}$. Johnson-Nyquist noise in the frequency domain is described as white noise.

E.1.3 Mechanical Vibrations

Because the Faraday rotation is defined as a relative value to a polarizer angle it is important to keep the optical elements from moving relative to each other. In reality, however, vibration from the surrounding influence the position and rotations a little as shown in figure E.1.

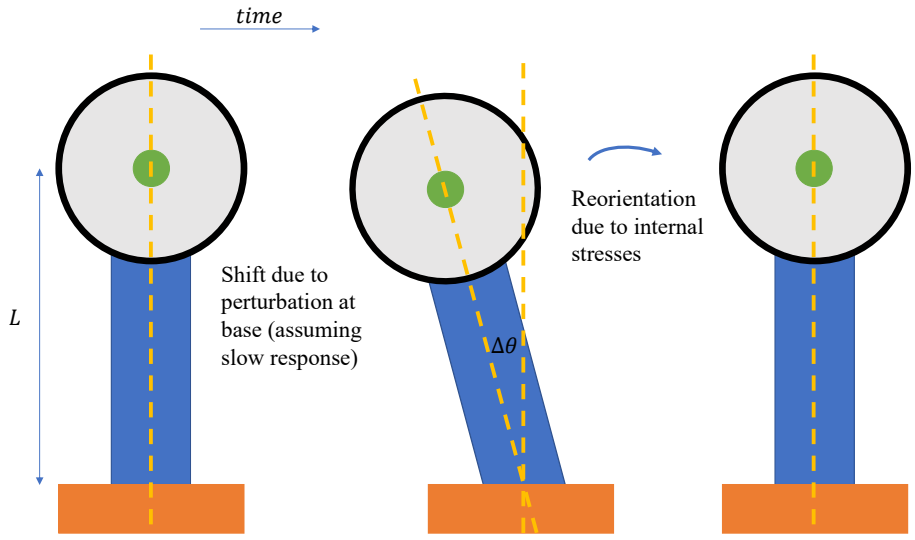

Figure E.1: A optical element, top circle, on top of a optical post, blue, of length L that experiences a perturbation at its base, orange. The perturbation causes the optical post to rotate with an angle $\Delta\theta$ (center figure) from its rest position (left figure). When the perturbation goes to zero or goes opposite the optical post relaxes back to its resting position again (right figure).

The influence of these vibrations is determined by assuming that the response can be described by a driven damped oscillator [98]. The maximum amplitude is then given by

$$A_{max} \approx \frac{f_0}{2\beta\omega_0} \tag{E.4}$$

where ω_0 is the natural frequency of the undamped oscillator that is given by

$$\omega_0 = \sqrt{\frac{k}{m}} \tag{E.5}$$

where k is the spring constant and m the mass of the optical post. $\beta = b/2m$ is the viscous damping coefficient (or damping constant) where the damping coefficient is

$$b = 2\zeta\sqrt{mk} \tag{E.6}$$

and ζ is the damping ratio. The amplitude of the driving force $f_0 = F_0/m$ can be approximated using typical vibrations of a lab as

$$f_0 = v_{lab} f_{lab} \tag{E.7}$$

where v_{lab} is the velocity amplitude in m/s and f_{lab} is the frequency of the vibrations in Hz. The spring constant of the optical post is approximated using

$$k = E\frac{A}{L} \tag{E.8}$$

where E is the Young's modulus, A the cross section and L the length of the optical post. Using equations E.4, E.5, E.6, E.7 and E.8 the maximum rotation, assuming small rotations $\Delta\theta \approx A_{max}/L$, due to vibrations is given by

$$\Delta\theta = \frac{v_{lab} f_{lab} m}{2AE\zeta} \tag{E.9}$$

Practical values are:
$v_{lab} \sim 10^{-4}$ m/s, $f_{lab} \sim 100$ Hz, taken from:
`https://www.thorlabs.com/tutorials/tables2.cfm`
Young's modulus steel: 200 GPa `https://en.wikipedia.org/wiki/Young's_modulus`.
Optical posts used $A = 0.0127^2 * \pi$ and mass $m = \rho * A * L = 8050 * 0.0127^2 * \pi * 75\text{mm} \sim 60$ g, taken from:
`https://www.thorlabs.com/newgrouppage9.cfm?objectgroup_id=1266`
`https://en.wikipedia.org/wiki/Steel`.
Damping ratio of ∼0.01, taken from:
`https://www.crystalinstruments.com/multi-resolution-spectrum-analysis`

Using above values the approximate rotation due to vibrations is of the order of 1-10 nrad.

E.2 Total Error Calculation

For the calculation of the total error it is necessary to distinguish between the different types of errors and whether they can be compensated. The 68% confidence interval is used for errors that are stochastic in nature, such as shot noise and thermal noise. They are called sum square noise (SSN), e.g. $\sigma_{shot}, \sigma_{Johnson-Nyquist}, \sigma_{vib}$. Deterministic error terms can have a sign, e.g. a lower gain can be associated with a decrease of a parameter and vice versa. The terms that can compensate each other are called linear errors (LE), e.g. $\sigma_{T,direct}, \sigma_{\lambda,direct}$. While terms that do not have a direction are put under the SSN, e.g. $|\sigma_{T,undirectional}|, |\sigma_{\lambda,undirectional}|$. Both are considered 100% uncertainty. The total error can then be called using:

$$\sigma_{tot} = \sigma_{T,direct} + \sigma_{\lambda,direct} + |\sigma_{T,undirectional}| + |\sigma_{\lambda,undirectional}| + \sqrt{\sigma_{shot}^2 + \sigma_{Johnson-Nyquist}^2 + \sigma_{vib}^2} \tag{E.10}$$

Due to the nature of most SSN they scale with the gain of the current sensor while LE impacts the gain directly and does not scale with it.

E.2.1 Parameters

The outputs of a balanced photodiode use a fixed resistance with an accompanying saturation. However, in the calculation of the total error and signal this cannot remain fixed as the maximum signal can surpass the saturation limit of the balanced photodiode. To compensate for this the resistance at the outputs are scaled to always have an equal maximum voltage. For the DM output the maximum voltage of 10V is set equal to the range of the current sensor using

$$G_{DM} = R_{DM} = \frac{10}{R(\lambda) P_{inc} \sin(2\theta_{F,max})}, \tag{E.11}$$

where $\theta_{F,max}$ is maximum Faraday rotation of the current sensor and P_{inc} is the maximum incident power on the photodiode after transmission losses. For the monitor resistance the value mainly depends on P_{inc} as $R_{mon} = R_{mon,0} * P_{inc,0}/P_{inc}$ where $R_{mon,0}$ is the resistance when the incident power is $P_{inc,0}$. This values is set to be equivalent to the specification of the balanced photodiode when the incident power on a single photodiode is 1 mW.

E.2.2 Further mathematical tricks

The total laser power is reduced by the transmission and absorption (Beer-Lambert law) through multiplication. Gain losses are taken into account by artificially lowering the Verdet constant. This is mainly relevant for the derivation of the theoretical error in section 5.3.2. The effect of a change in parameters is calculated numerically when no analytic solution were found. The error is considered tobe the maximum difference between the new output and the ideal output normalized to the range of the current sensor.

E.3 Optimum path length

The scaling of the total error with path length is linear. The scaling with the absorption is directly related to the incident power. The incident power scales the total error by decreasing the relative shot noise. Its effect is given by the

$$\frac{\sigma_{I_P}}{I_{P,max}} \propto L\sqrt{\exp(-\mu L)}, \tag{E.12}$$

which has a peak at $L = 2/\mu$.

Appendix F

Calibrations

In figure F.1 the calibrations of the setup of figure 4.2 is shown. Instead of the coil a second polarizer is used to simulate the effect of the Faraday rotation. This comparison is allowed up until the rotation surpasses 0.1 rad where the intensity starts dropping enough a non-linearity becomes visible. However, this is never reached as the RF output is saturated over a range of 23 mrad. This range can be expanded by lowering the intensity but the Faraday rotation in the experiments never reach this 23 mrad and it is therefore not necessary. The linear coefficient of the fit is -1.8618 ± 0.0004 per rad. By multiplying the equation 4.4 with this value the Faraday rotation can be obtained.

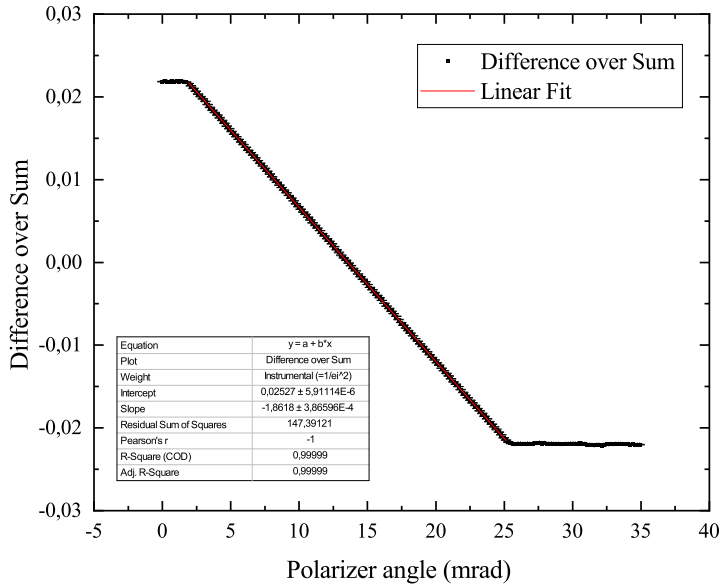

Figure F.1: The Difference over sum of equation 4.4 versus the angle of the polarizer starting from an arbitrary angle that is situated somewhere near 0 deg. The black squares are the experimental data and the red line is the linear fit in the non-saturation regime.

F.1 Aligning the Optical Setup

When placing the optical elements care is taken with reflections to not enter the laser again and are controlled for safety reasons. This is achieved by rotating the optical elements slightly. This effects, however, changes the polarization in a minor way due to the polarization dependent reflections at non zero angles. This effect is most important after the Faraday rotation has been picked up. Because the polarization is p-polarized any of such changes generally decrease the gain of the setup. For instance the TGG→Air interface at 3 degrees causes the contrast to drop by roughly 0.2% as more s-polarized light is reflected in comparison to p-polarization. When the main beam is the reflection of an interface, however, the contrast is instead increased. In section 5.3 the effect of reflections is discussed more thoroughly.

F.2 Thickness TGG

The thickness of the TGG measured was 0.506, 0.517, 0.505, 0.500 and 0.503 with an uncertainty of 1 μm. It is possible that the large difference of the second measurement was caused by some dirt or inhomogeneous surface of the TGG. The mean with standard error is 0.506 ± 0.003 mm which will be used when determining the Verdet constants through fitting.

F.3 Magnetic field determination Sweep

The approach is shown in figure F.2. The magnetic field is estimated by finding the starting point where the signal changes significantly due to the current applied going from 0 A to -1 A and the ending point where the signal changes significantly due to the current applied falling from 1 A to 0 A. By assuming linear time dependency the magnetic field is determined. The offset determined from a fit is subtracted to set the output to zero at zero magnetic field. Inaccurate positions taken at -1 A and 1 A lead to roughly 0.2% inaccuracy of the slope per measurement point away from the accurate position. This effect is generally an underestimation because the signal is lower at the highest magnetic field.

F.3.1 Averaging vs. Sweep

In figure F.3 multiple measurement results for the two different methods are shown. The averaging method is used in measurements 1,2,3 and 4 while the sweep method is used in Sweep. It can be seen that all the results are relatively close to each other. However, when performing a linear fit it can be seen that the slope of all the measurement results differ more than the standard deviation allows. The measurements using the averaging method show a smaller deviation from each other than the sweep methods which deviation is significantly higher with a maximum of 6%.

In figure F.4 the residue after the linear fit has been subtracted from the experimental data is shown for both measurement methods. For the sweep method (black) no distinct behaviour is visible and the noise can be considered Gaussian. For the averaging method (red, blue and green), however, a slight non linear effect is visible with the residue showing a recurring parabolic behaviour. These effects are the largest when the magnetic field is > 10 mT with a difference of roughly 10 μrad. This is for the 0.5 mm TGG sample an effect of roughly 1.5%. This would be equivalent to a temperature increase of ~ 5 K assuming the temperature dependence of 0.3%/K of TGG. The currents of $\sim \pm 1$ A that flow through the coil(s) start heating the coil. This heating causes the resistance of the coil to increase and might momentarily decrease the magnetic field due to the reduced current. Additionally the TGG sample heats up due to the indirect contact with the coil lowering the signal even more. This might explain why the slopes found in the averaging method in figure F.3 are slightly lower compared to the sweep. This means that the sweep method may be better to use. This could be checked more thoroughly by measuring the current during a sweep measurement and comparing with the averaging effect.

To obtain some information about the Verdet constant the mean and the standard error of the

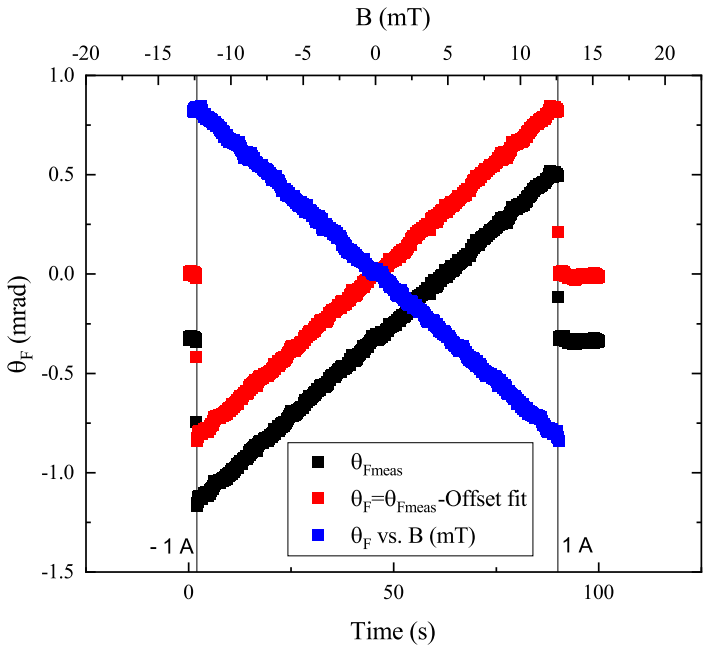

Figure F.2: The method used to obtain the Faraday rotation against the magnetic field for a sweeping current. The offset at $t = 0$ is subtracted (red) from the experimental data (black). The time is then converted to a magnetic field (Blue) by choosing a point of large change near 2 s and 80s to be equal to -1 A and 1 A, respectively.

mean is calculated. The result gives a mean gain of $(-6.35 \pm 0.08) * 10^{-2}$ rad/T. The mean Verdet constant is then $\mathcal{V} = 125.5 \pm 0.7$ rad/Tm, where the error of the Verdet constant is determined using

$$\sigma_V = \sqrt{(\frac{gain}{L^2})^2 * \sigma_L^2 + (\frac{1}{L})^2 * \sigma_{gain}^2}. \tag{F.1}$$

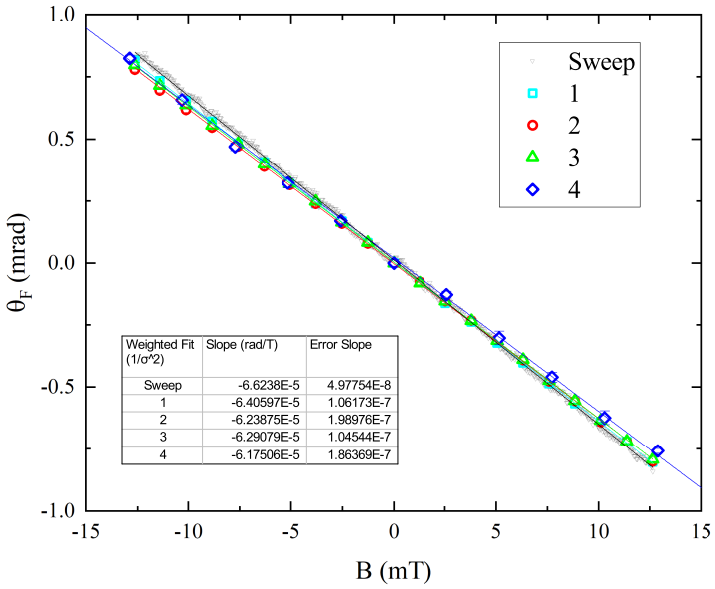

Figure F.3: The method used to obtain the Faraday rotation against the magnetic field for a sweeping current.

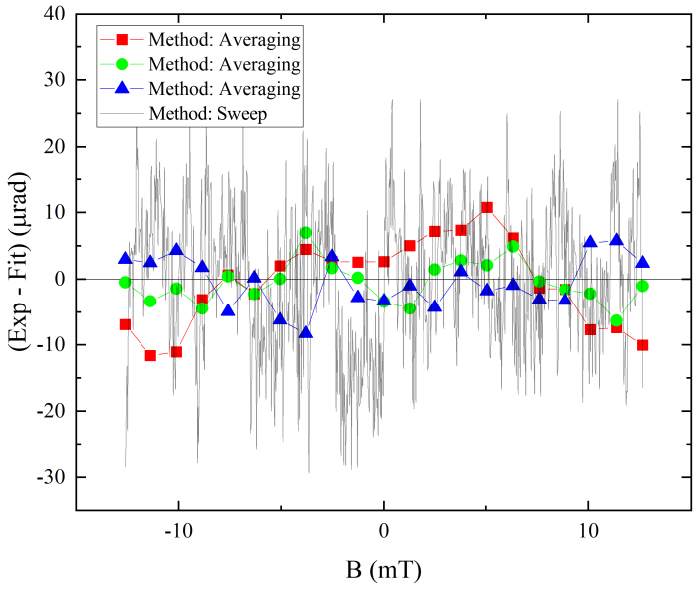

Figure F.4: The residue after the linear fit has been subtracted from the experimental data. In the red, green and blue dots the Averaging method is used. In the grey line the Sweep methods is used.

Appendix G

TGG Error Measurements

G.1 Temperature Dependence

The setup in figure G.1 is used to measure the effect of temperature on the TGG crystal. The fohn, Steinel HL1800 E, is switched on to reach a stable temperature. Then measurement starts while the föhn remains on. The temperature is measured using a Type K thermocouple placed near the TGG. It is manually checked at regular intervals using a Voltcraft 500. The temperature

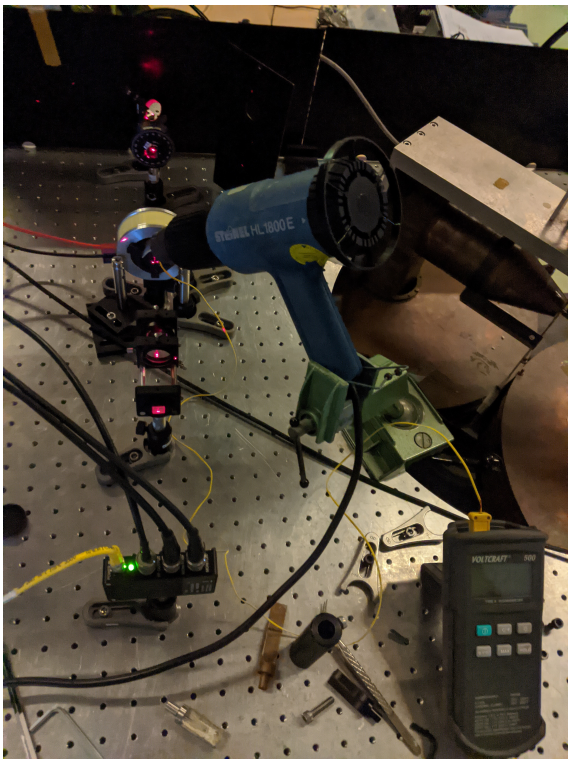

Figure G.1: The measurement setup used to measure the effect of temperature. A föhn is hold in place and aimed at the sample holder with TGG that is placed in a coil. A thermocouple (yellow wire) is placed near the TGG crystal and manually read-out.

dependence of the TGG sample can be seen in figure G.2. The solid line is the scaled $1/T$ dependence of the Verdet constant based on the findings in [35, 37]. It can be seen that the temperature dependence is roughly $0.3\%/K$ and comparable to the value found in literature of

$0.347\%/K$. The large errorbars in the temperature is caused by the drift in temperature during the measurement as the setup was not very stable and showed drift.

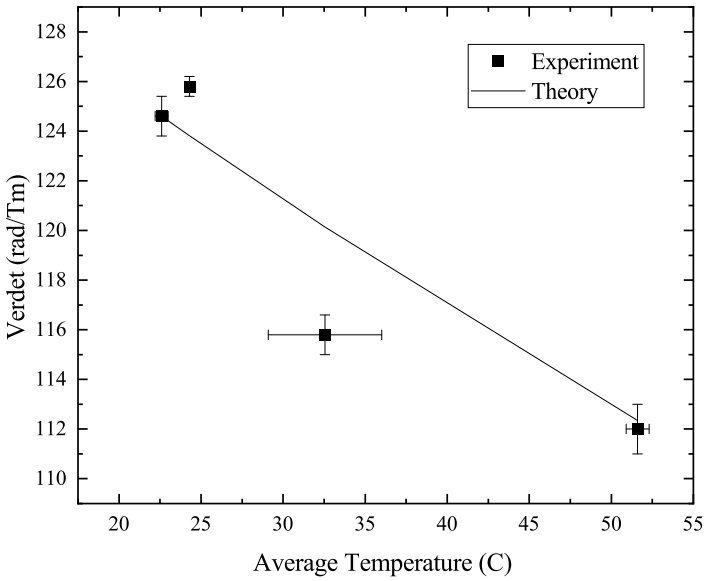

Figure G.2: The Verdet constant for different temperatures. The points are experimental values and the line is the theoretical approximation based on [35, 37].

G.2 FFT

The Fast Fourier Transform (FFT) of the error of the RF output voltage is shown in figure G.3. The logarithmic fit shows that the error goes roughly with -13 dB/decade which is almost equivalent to a 1/f noise which goes as -10 dB/decade. The slight difference can be caused by the FFT not taking into account the irregular sample acquisition causing the sampling frequency to vary. This pink noise is only present when the laser is turned on and disappears when the photodiodes are blocked. It is therefore most likely related to the laser [70]. Using modulation techniques at high frequencies $>>$ 1 MHz this 1/f noise might be removed entirely.

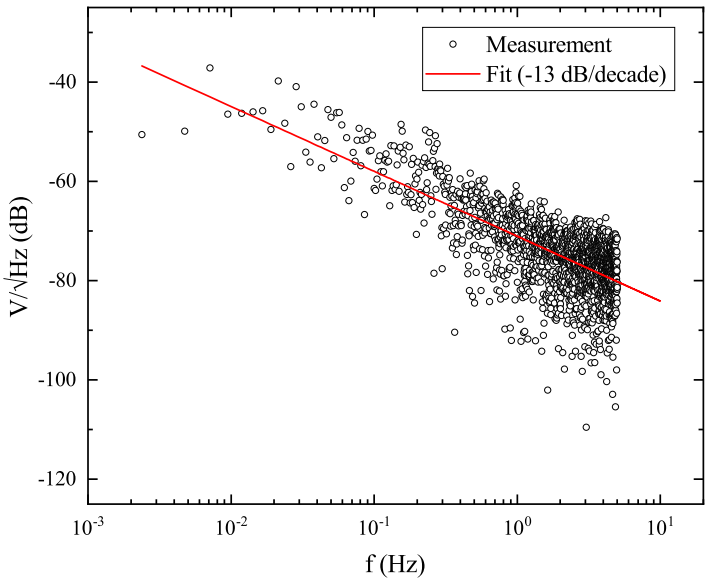

Figure G.3: The FFT of the error of the RF output voltage as measured with an Agilent 34410A. The black squares are the measurement point and the red line is a logarithmic fit.

Appendix H

Crystal Path length

The conversion of the uncertainty in the path length to the gain applicable to a linear fit of equation 3.2 is performed using:

$$\sigma_{y,new} = \sigma_{y,measurement} + V\sigma_L \tag{H.1}$$

where $\sigma_{y,measurement}$ is the uncertainty of the gain in the measurement and σ_L is the error in the path length. When using $\sigma_L = 10\%L$ for the TGG crystals the last term of the equation becomes $10\%VL$ which is simply 10% of the Gain. This error is used in the weighted fitting and therefore calculated into the error shown in the table of figure 5.3. An identical method is used for the Glass.

H.1 Non-Linear behavior

Both Glass and TGG deviate from a linear behavior since they have larger gains at larger path lengths. This effect can be seen in figure H.1 where the mean of the first measurement point is linearly extrapolated with the path length. It can be seen that the gain at higher path lengths start deviating more and more indicating a possible non-linearity. The deviation might originate from the inhomogeneous magnetic field inside the coil, where magnetic field increases as the sample gets deeper in the coil. Additionally due to the stacking multiple crystals on top of each other multiple interfaces are present that might have a non-zero reflection, e.g. ghosting. The effect of this is shown in figure H.2. The transmitted beam might contain multiple beams that have bounced multiple times inside the crystals. These additional beams will have a significantly lower intensity. However, due to the non-reciprocability of the Faraday effect these additional beams will have an enhanced Faraday rotation. For a TGG to Air interface the Reflectance, $|r|^2$, is roughly 10%. This means that about 1% of the output beam will have an enhanced Faraday rotation. The gain increase factor with would be roughly $1\% * 3 = 0.03$ for a single of such an internal reflections. Additional air gaps in between the crystals could create more internal reflections that further increase the gain in the same manner. Using an AR coating on the TGG crystals would diminish this effect. It could be tested by comparing it with a single TGG crystal with corresponding lengths. Also, the effect of alignment might be an issue as discussed in appendix F.1.

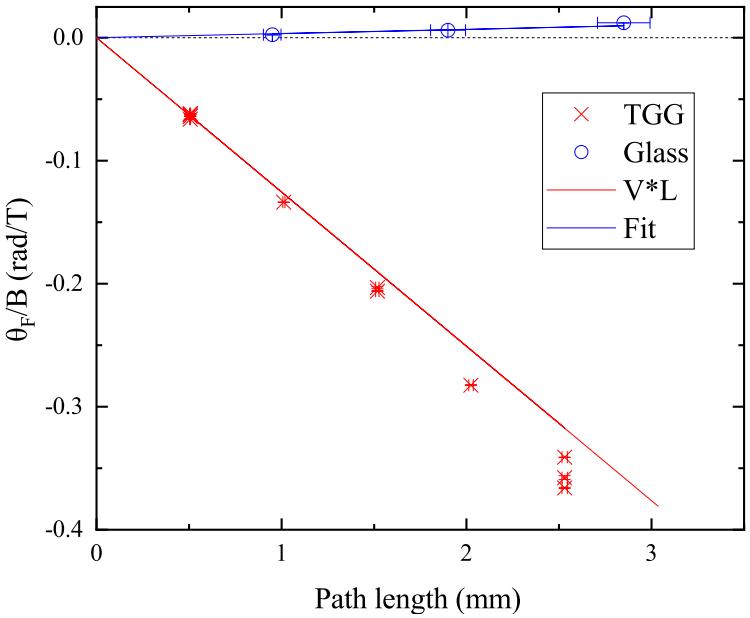

Figure H.1: The gain of the setup, given in $\frac{\theta_F}{B}$ (rad/T), for different path lengths obtained by placing an integer number of crystals against each other. The red crosses are for 0.5 mm TGG crystals and the blue circles are for 0.95 mm glass plates. The solid lines are the theoretical result of equation 3.2 when only the result of first measurement point is used.

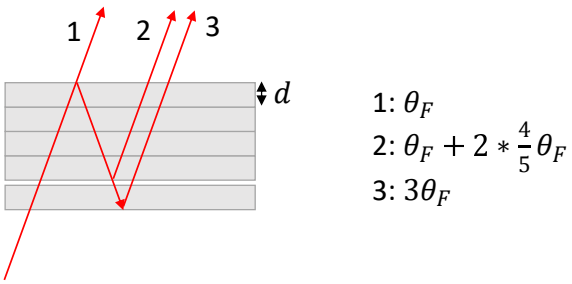

Figure H.2: A schematic view of internal reflection occurring at interfaces of different crystals of thickness d and air gaps. The first beam, 1, contains most intensity and has only a single Faraday rotation. The second beam, 2, is reflected due to an air-gap between the crystals, having attained additional Faraday rotation of $2 * 4/5 * \theta_F$. The third beam, 3, reflects at the crystal Air interface and contains the most Faraday rotation, $3\theta_F$.

Appendix I

Reflections

I.1 Influence Mirrors experiment

In the BS setup the three mirrors ($\Delta\delta = 3 * 0.3 = 0.9$ rad) only reduce the first Faraday rotation while the second one is unaffected which allows the gain to still to be large. In MS setup, however, the entire Faraday rotation, $2\theta_F$, is reduced by two mirrors ($\Delta\delta = 2 * 0.3 = 0.6$ rad) lowering the signal to almost the same as in the BS setup even though the relative phase shift of the BS is higher. This shows that it is relevant where the Faraday rotation occurs in the path of the light, i.e. destructive interference occurs only when there is conversion of s- to p-polarization (or vice versa).

In figure I.1 the effect of placing the TGG with coil at different position in the beamsplitter setup of figure 5.5 is shown. It can be seen that as the number of mirrors after the Faraday rotation is higher the gain of the output lowers. The gain is maximum when no mirrors are placed after the Faraday rotation and minimum when 3 mirrors are placed after the Faraday rotation. The experimental values show a relatively good agreement with the theoretical predictions.

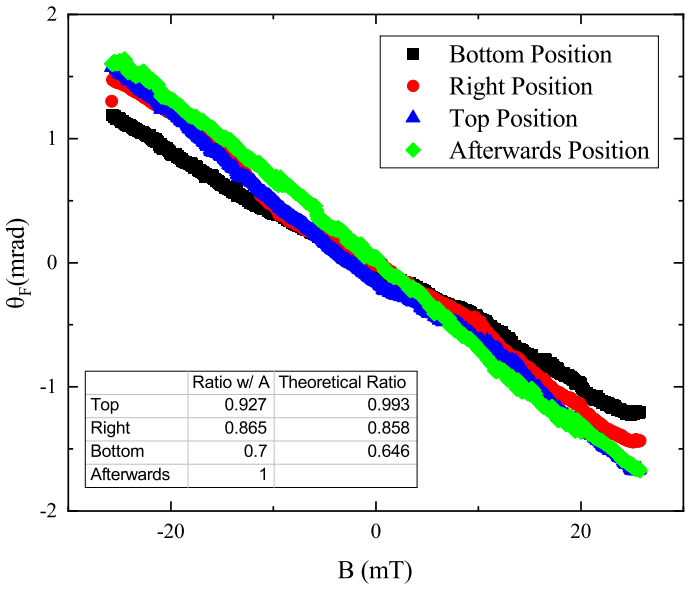

Figure I.1: The Faraday rotation against the magnetic field when the Faraday rotation occurs at different positions in the BS setup of figure 5.5. In the bottom position three mirror are used to reflect the beam back to the laser after the Faraday rotation has been picked. In the right position only two mirrors are in between the detector and the coil. In the top side there is only one mirror after the coil. The afterwards position is identical to the single pass result of 5.7 where there are no mirror after picking up the Faraday rotation. In the inset table the ratio to the afterwards position is shown. The last column is the theoretical ratio using Jones formalism.

I.2 Magnetic field drop

Assuming the magnetic field is constant along the length of the crystal but not the width the effect is roughly:

$$\frac{\int B(r)\cdot dl}{\int B(r_0)\cdot dl} = \frac{\int_{r_0}^{r_1} \frac{B(r)}{\tan(\theta_i)} dr}{\int_{r_0}^{r_1} \frac{B(r_0)}{\tan(\theta_i)} dr} = \frac{r_0 \ln(\frac{r_1}{r_0})}{r_1 - r_0}, \tag{I.1}$$

where $r_1 = d + r_0$ and $r_0 \approx 3$ mm is the distance from the center of the current wire to the beginning of the crystal. For a crystal with a width of 5 mm equation I.1 gives a factor of roughly 0.59 lower signal due to the reduced magnetic field at larger distances.

I.3 High Reflectance

In figure I.2 the high reflectance (HR) case of a TGG to Silver interface is shown. At low angles of incidence the relative phase shift lowers. The large difference between the real part and the imaginary part of the refractive index of silver, ($n_t = 0.049816 - 4.4764i$ [71, 72]), allows for a near unity reflection coefficient which is necessary for high transmission. However, this large difference does increase the non-ideal relative phase shift at $\theta_i > 0$ slightly but at a much slower rate than the drop in reflection coefficient.

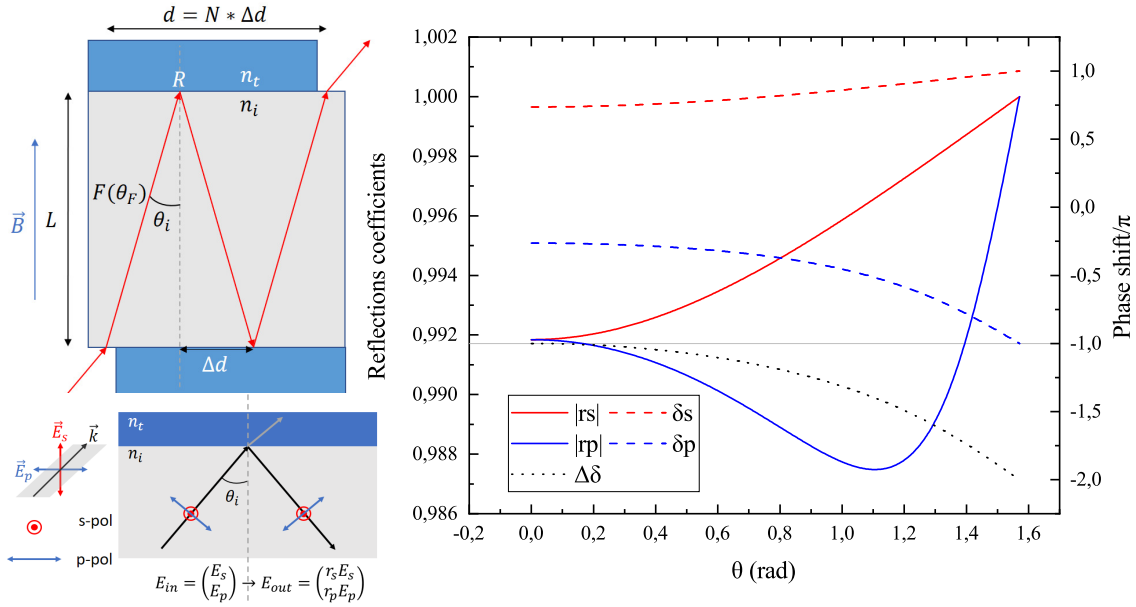

Figure I.2: The top left shows schematically the path of the light in the case of high reflectance. Bottom left shows a schematic view of a reflection at the interface. In the graph on the right the reflections coefficient, solid lines, and the phase shift, dashed lines, are shown as functions of the angle of incidence for a TGG to Silver interface. Red represents s-polarized light and blue p-polarized light. The black dotted line is the relative phase shift between s- and p-polarization.

I.4 Total Internal Reflection

In figure I.3 the reflection coeffients and phase shift of a TGG to Air interface is shown. In the inset the phase shift and relative phase shift is shown for an interface where the difference in refractive index is small: $\Delta n \approx 0.3\%$. The relative phase shift near 1.5 rad is ~ 0.12 rad and ~ 5 mrad for the TGG to Air and Δn case, respectively. Near 0.53 rad the critical angle is reached for the TGG to Air interface showing negligible relative phase shift.

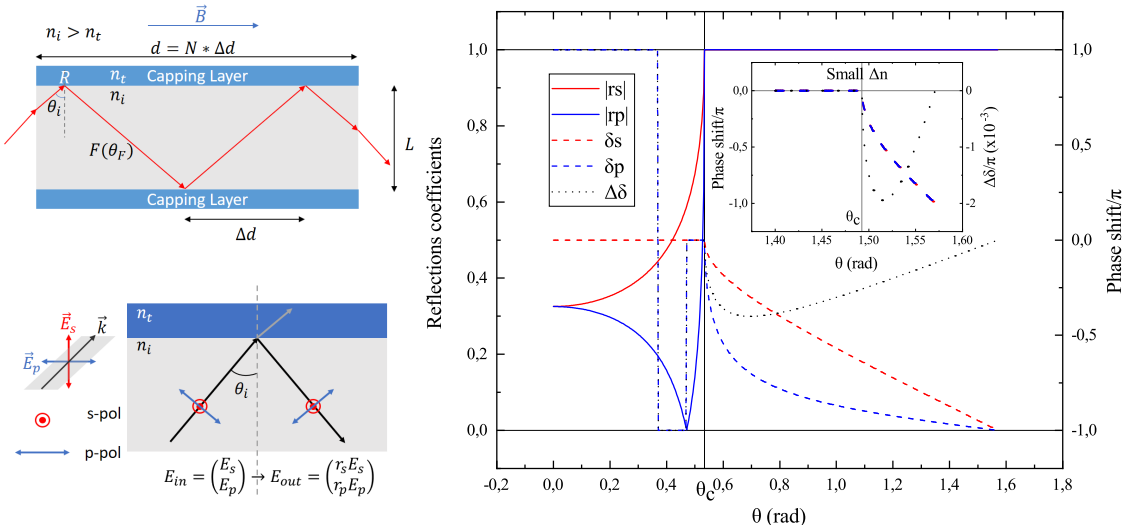

Figure I.3: The top left shows schematically the path of the light in the case of total internal reflection (TIR). The best configuration is when the magnetic field is along the width of the crystal. Bottom left shows a schematic view of a reflection at the interface. In the graph on the right the reflections coefficient, solid lines, and the phase shift, dashed lines, are shown as functions of the angle of incidence for a TGG to Air interface. Red represents s-polarized light and blue p-polarized light. The black dotted line is the relative phase shift between s- and p-polarization. In the inset of the graph the phase shift and relative phase shift are shown when a transmission material with a similar refractive index of TGG is used, with a difference of only $\Delta n \approx 0.3\%$. In the inset the value of the relative phase shift is shown on the right y-axis. The critical angle(s) θ_C are shown using a vertical line.

Appendix J

Indepth Outlook

Temperature compensation techniques

The feedback system proposed in section 6.1 may aid in reducing temperature effects significantly but the required bandwidth could be a bottleneck in realizing the design. This means that the LE of 240 ppm remains an issue. One of the methods to lower the LE is to monitor the temperature of the setup and adapt according to calibration data. Perdante et al. have shown that by using a temperature dependent birefringent plate a compensation scheme can be incorporated into the analysis [89]. This requires a modulation on the Faraday rotation. This can be achieved with an externally applied magnetic field or modulating the primary current. They showed that the temperature error lowers by roughly an order of magnitude.

The thermal dependency can also be compensated by moving the crystal from or closer to positions of higher magnetic fields by applying a material with high thermal expansion. Mironov et al. have shown such a concept for a Faraday isolator [90]. They showed an improvement of roughly an order of magnitude. This can be applied to the Faraday current sensor with a highly thermally expansing material which moves the laser beam relative to the position of the current carrying wire. Then, the temperature dependence of equation 3.2 can be expanded as

$$\frac{\partial \theta_F}{\partial T} = \frac{\partial \mathcal{V}}{\partial T} BL + \frac{\partial B}{\partial T} \mathcal{V} L + \frac{\partial L}{\partial T} B \mathcal{V}. \tag{J.1}$$

Assume the effect of temperature on the path length to be negligible, i.e. $\frac{\partial L}{\partial T} \approx 0$,. To arrive at $\frac{\partial \theta_F}{\partial T} \approx 0$, using equation 3.4, requires

$$\frac{1}{r}\frac{\partial r}{\partial T} = -(\frac{1}{\mathcal{V}}\frac{\partial \mathcal{V}}{\partial T}). \tag{J.2}$$

This means that a movement of the laser beam of 3000 ppm/K suffices to compensate the explicit temperature drift of the Verdet constant. This can be achieved by moving the current wire or have the thermal expansion of a mirror cause a slight change in an angle of incidence. This results in the beam deviating towards the current wire. This last effect can also be used to increase the number of reflections to offset the gain loss due to temperature effects of the Verdet constant. In general, it is not necessary to use a Faraday rotation as feedback. A polarization rotation can also be obtained using a photoelastic material driven by a voltage. An example is the electro-optic modulator which has a typical bandwidth of 1 GHz. As long as its temperature coefficient is equivalent to that of the Faraday crystal the temperature effect can be diminished. Another possible solution is to use interferometers made with glass fibers. Muller et al. have shown that interferometers are less sensitive to temperature drift than their polarimetric counterparts [99].

Insensitivity to the linear birefringence

Optical fibers have as major advantages that it can easily be bend around a current wire. The path length of the light in such a fiber to go up to several meters. However, the bending itself adds linear birefringence that increase the phase shift [7]. Bush et al. found that a highly circular birefringent fiber can solve this issue [75]. A similar argument can be used for the reflections discussed in section 5.3.2. In figure 5.8 the output for 10 reflections with a relative phase shift is significantly reduced at low Faraday rotations per reflection. On the other hand, looking at high Faraday rotations per reflection the difference between the ideal output and the actual output becomes smaller. Consequently, applying a magnetic field offset to increase the Faraday rotation per reflection would remove the effect of the relative phase shift on the gain and a higher number of reflections becomes possible.

The effect on the gain is shown in figure J.1. As the Faraday rotation per reflection increases the maximum gain increases also, i.e. from small values of ~ 1/rad at $\theta_F = 0$ to 20/rad at 1.5 rad. The grey area is the preferred position for maximum gain. The Biasing the magnetic field is a possibility but circular birefringent materials (optical activity) could also be used [100, 101].

The temperature dependency of the spontaneous magnetization (M) of a permanent magnet such as Cobalt ($T_C = 1400$ K) described by Bloch's law ($\frac{M}{M_0} = (1 - (\frac{T}{T_C})^{3/2})$) can be of the order of 500 ppm/K. Assuming the bias Faraday rotation to be 45 deg the temperature drift then is 0.02 deg/K as an offset drift. Therefore Faraday rotations due to the magnetic field of the current wire must be much larger than 0.02 deg otherwise compensation is necessary. It may, therefore, be easier to use a intrinsic circular birefringence such a a chiral material.

A similar tool is the Faraday mirror for reducing the linear birefringence along the entire path length [102]. Furthermore, one can use periodic paddings to block the magnetic field to compensate for linear birefringence [103]. Adapting to thin films may also be a solution in lowering the linear birefringence [104].

Cavity

When the angle of incidence is exactly zero a cavity can be created [91]. Sun et al. have numerically shown that a cavity used at room temperature results in a sensitivity of 25.6 fT/$\sqrt{\text{Hz}}$ [92]. For a bandwidth of 1 MHz this gives a sensitivity of 25.6 pT. This is almost 3 orders of magnitude below the required 10 nT. Chang et al. have shown experimentally that a single path can be enhancement up to 85 times inside a cavity [22]. They also discussed the possibility for a TGG based cavity that might achieve a magnetic sensitivity of ~ 10 pT/$\sqrt{\text{Hz}}$. This gives exactly the required 10 nT at 1 MHz. However, cavities suffer from background reflections, wavelength filtering effects, stability requirements for resonance and significant effects from temperature drifts. Equally important are the spurious signals that are caused by the resonance.

Reflection Coatings

The air to TGG interface has a significant loss of roughly 10% due to the large difference in refractive index. This is especially relevant for cavities such as the one proposed by [22]. This high loss can be resolved partially by using an AR coating with the optimal refractive index given by

$$n_{AR} = \sqrt{n_i * n_t}. \tag{J.3}$$

For the air to TGG interface a material with refractive index of $n_{AR} \approx 1.4$ would reduce the loss by roughly a factor 2.

The effect of phase shifts by a reflection may be overcome with multi layered structures, e.g. Bragg reflectors. By tuning the thickness and refractive indices of the layers one can design a

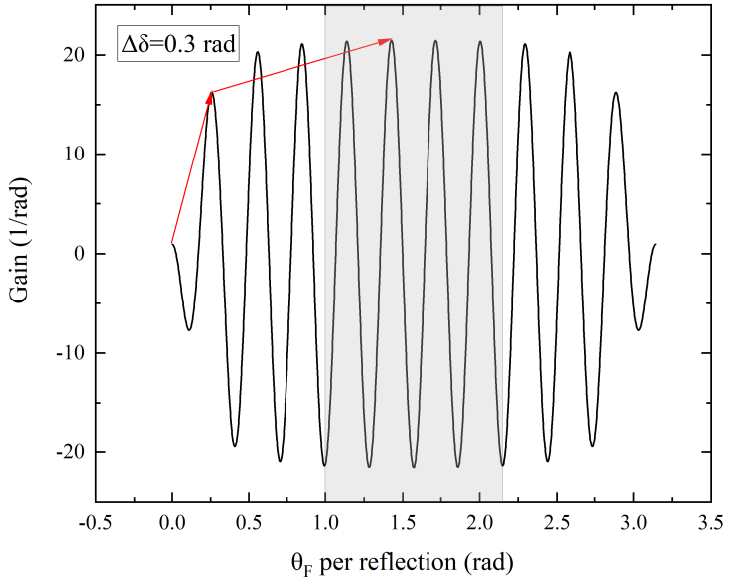

Figure J.1: The gain against the Faraday rotation per reflections for a relative phase shift of $\Delta\delta = 0.3$ rad and $N = 10$. Derived from equation 5.6.

reflection to have a specific phase shift [105].

Modulation

The main disadvantage of modulation is the limit it superimposes on the bandwidth of the device it is used in. The Faraday current sensor can, however, operate at a very high bandwidth and modulation may be interesting to use. By modulating at e.g. 10 MHz one still can retain a bandwidth of 1 MHz around the 10 MHz. Optical modulation can then help remove the 1/f noise that was found in section 5.1.1 but it cannot help remove shot noise as this is white noise. This type of modulation can be achieved by using photoelastic modulations or by modulating the laser current itself. Subkhangulov et al. have even shown possible modulation frequencies of up 1.1 THz [106].

Photonic Integrated Circuit

Most of the materials discussed in section 3.3.2 show significantly lower Verdet constants in the NIR wavelength range. Because the $4f \rightarrow 4f5d$ transition of REs has a transition wavelength in the UV it may be less feasible to use REs, instead materials with transition wavelength much higher, (VIS or NIR), should be investigated.

Due to the large path lengths required the Faraday crystal may not be easily integrated in a PIC directly. Though garnets have been proven to be growable on the substrates for PICs [107]. However, if integrated in a PIC the number of reflections and the relative phase shift picked up at each reflection could be easier to control. The best targets for the PIC are the surrounding components which can be attached to the crystal, as shown in figure J.2. The polarized light could be obtained by directly attaching a waveguide to a laser and letting it pass a polarization filter. These polarization filter have a suppression up to -17 dB. A PIC that is equivalent to the phase retarder is a polarizing controller [108]. The polarizing beam splitter could be replaced by

a polarization splitter with a splitting ratio up to 20 dB [94]. Moreover, because the entire sensor is on a chip the output can also be analyzed on-chip. This would allow multiple outputs of PICs to be analyzed at the same place. Replacing the bulk materials with fibers may allow for easier attachment to PICs.

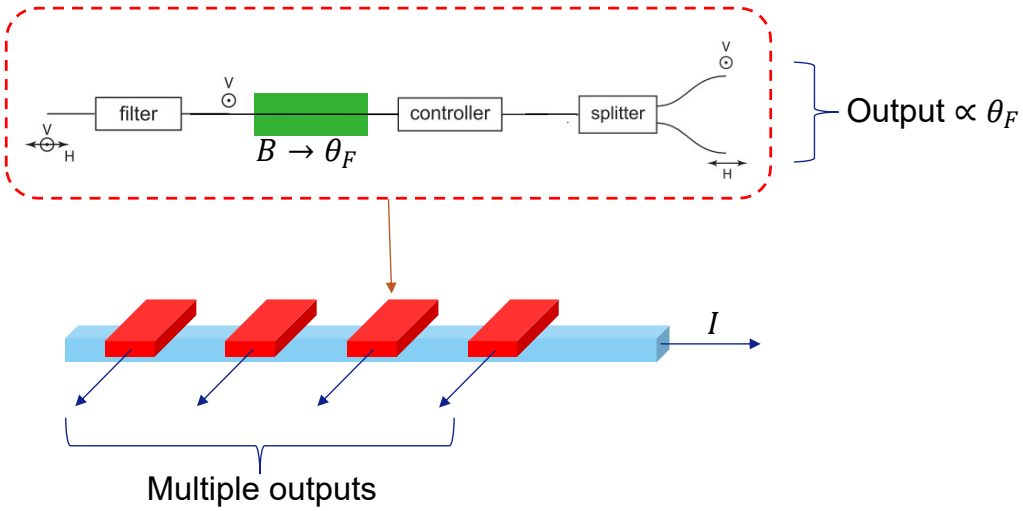

Figure J.2: A PICs equivalent design of a polarimetry measurement setup. The green square is the crystal (TGG) where the Faraday rotation occurs. Adapted from [94].

Stray field insensitivity

Insensitivity to a stray field can be achieved by enclosing the entire current wire with the light path, e.g. the entire magnetic field line is followed. Fibers can easily be bent, but bulk materials have to be cut. Geometries have been investigated, e.g. simply placing multiple elements around the wire or using internal reflection that send the light around the wire [9, 109]. By optimizing the geometry between different Faraday based current sensors crosstalk and influence of stray fields may be minimized. This may be especially relevant for the HR design in figure 6.2 and the multiple PICs discussed above [110, 111]. Furthermore, by using bulk materials, large number of reflections and PICs it is possible to keep the current sensor small. This makes enclosing with a mu-metal easily feasible.

Other possibilities

A flux concentrator can be used to enhance the magnetic field gain by a factor of up to ~ 40 [54]. The crystal can also be placed in the gap of a magnetic core and subsequently the light is aligned parallel inside the gap using reflections [79]. Magnetic core do, however, introduce new temperature drift and possible linearity issue.

One of the problems of a polarimetric measurement setup is the determination of systems parameters in addition to possible long term drift of these parameters. Rietmans et al. recently have proposed a calibration method for pulses measurements that may accurately determine the systems parameters and reduce possible systematic errors [93].

The Faraday effect may also be used to create different optical devices. Kharratian et al. discuss such a photonic device called Magnetooptical spatial light modulator [112].

Reflection Designs

Next, some possible reflection design are shown and briefly discussed. Figure J.3 shows a design that may be easily implemented when built on a chip. The main requirement is that the relative phase shift is exactly π at each segment away from the wire. A advantage is that this can be done away from the current wire.

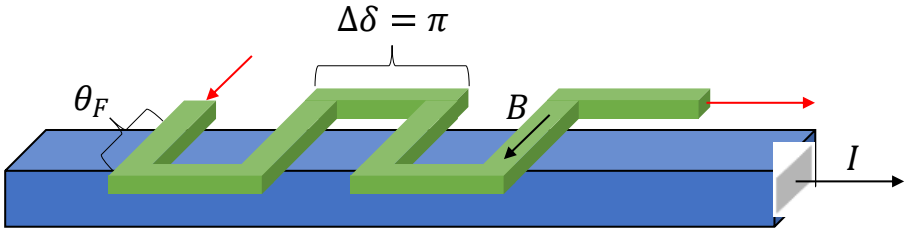

Figure J.3: A possible 2D design that may be more easily created on a chip. The relative phase shift $\Delta\delta = \pi$ at the horizontal segments.

In figure J.4 the HR case is adapted to work along the circular path of the magnetic field.

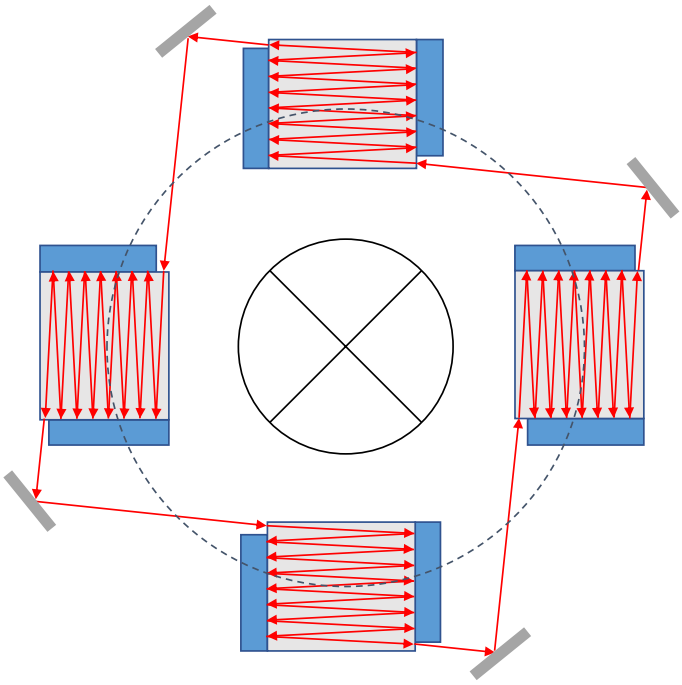

Figure J.4: A design that allows the light to pass multiple crystals using HR along the circular magnetic field.

In figure J.5 a design is show that uses a hollow cylinder to allow for for the light to make multiple trips around the current wire. A adaptation is to use a sphere instead and allow the plane of incidence to rotate in ways that may negate the linear birefringence.

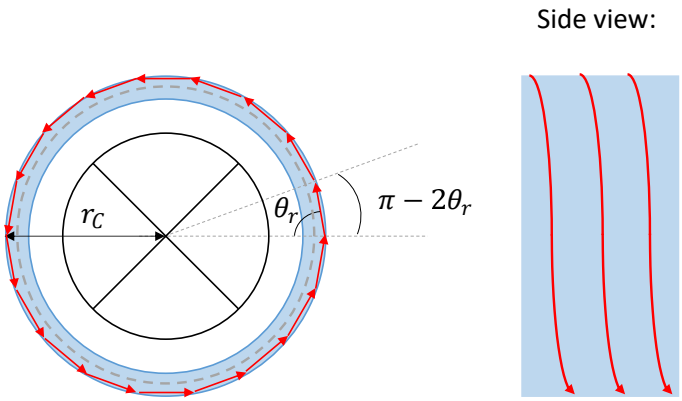

Figure J.5: A hollow cylinder similar to 6.2 but where the light can go along the cylinder axis (Side view) along the light to make multiple circular path. The number of reflections in a circle is only dependent on the angle θ_r; $N = \frac{2\pi}{\pi - 2\theta_r}$. For the small Δn case ($\theta_r = 1.5$ rad, the 100 reflections are already reached after 2 full circles.